

Craters on Charon: Impactors From a Collisional Cascade Among Trans-Neptunian Objects

Scott J. Kenyon

Smithsonian Astrophysical Observatory, 60 Garden Street, Cambridge, MA 02138

e-mail: skenyon@cfa.harvard.edu

Benjamin C. Bromley

Department of Physics & Astronomy, University of Utah, 201 JFB, Salt Lake City, UT 84112

e-mail: bromley@physics.utah.edu

ABSTRACT

We consider whether equilibrium size distributions from collisional cascades match the frequency of impactors derived from *New Horizons* crater counts on Charon (Singer et al. 2019). Using an analytic model and a suite of numerical simulations, we demonstrate that collisional cascades generate wavy size distributions; the morphology of the waves depends on the binding energy of solids Q_D^* and the collision velocity v_c . For an adopted minimum size of solids, $r_{min} = 1 \mu\text{m}$, and collision velocity $v_c = 1\text{--}3 \text{ km s}^{-1}$, the waves are rather insensitive to the gravitational component of Q_D^* . If the bulk strength component of Q_D^* is $Q_s r^{e_s}$ for particles with radius r , size distributions with small Q_s are much wavier than those with large Q_s ; systems with $e_s \approx -0.4$ have stronger waves than systems with $e_s \approx 0$. Detailed comparisons with the *New Horizons* data suggest that a collisional cascade among solids with a bulk strength intermediate between weak ice (e.g., Leinhardt & Stewart 2012) and normal ice (e.g., Schlichting et al. 2013) produces size distributions fairly similar to the size distribution of impactors on Charon. If the surface density Σ of the protosolar nebula varies with semimajor axis a as $\Sigma \approx 30 \text{ g cm}^{-2} (a/1 \text{ au})^{-3/2}$, the time scale for a cascade to generate an approximate equilibrium is 100–300 Myr at 45 au and 10–30 Myr at 25 au. Although it is necessary to perform more complete evolutionary calculations of the Kuiper belt, collisional cascades are a viable model for producing the size distribution of solids that impacted Charon throughout its history.

Subject headings: planets and satellites: dynamical evolution — planets and satellites: formation — dwarf planets: Pluto

1. INTRODUCTION

Beyond the orbit of Neptune, the Solar System contains a vast population of icy objects with radii ranging from $r \sim 1000 \text{ km}$ (e.g., Eris and Pluto; Brown & Schaller 2007; Sicardy et al. 2011; Stern et al. 2018) to $r \lesssim 1 \text{ km}$ (Schlichting et al. 2009, 2012; Liu et al. 2015). Although many of these trans-Neptunian objects (TNOs) have roughly circular orbits with semimajor axes $a \approx 35\text{--}50 \text{ au}$, others have highly elliptical orbits, $e \gtrsim 0.5$, with $a \gtrsim 100 \text{ au}$ (e.g., Gladman et al. 2008; Petit et al. 2011, 2017). Among all of the dynamical classes, the total mass in TNOs inferred from ground-based optical surveys is $\lesssim 0.1\text{--}0.2 M_\oplus$ (e.g., Fraser et al. 2014; Adams et al. 2014; Alexandersen et al. 2016; Lawler et al. 2018; Pitjeva & Pitjev 2018).

A recent analysis of data from the *New Horizons* mission creates tension between the number of TNOs *predicted* from deep surveys with ground-based optical telescopes and *derived* from direct counts of craters on Charon. Together with dynamical estimates based on the current population of Jupiter family comets (e.g., Levison & Duncan 1997; Emel’yanenko et al. 2004; Volk & Malhotra 2008; Brassier & Wang 2015, and references therein), the optical surveys require a steep size distribution, where the predicted number of 1 km TNOs is $\sim 10^5$ times larger than the observed number of 100 km TNOs. Normalizing the *New Horizons* results to the ground-based data at 10–20 km, the observed number of craters from 1–10 km TNOs is reasonably consistent with a steep size distribution. However, the number of 0.1–1 km TNOs derived from the *New Horizons* observations is roughly two orders of magnitude smaller than expected from an extrapolation of ground-based measurements (Singer et al. 2019). The deficit of small craters on Charon also disagrees with most theoretical (coagulation) models of planet formation, which predict counts more similar to those implied by ground-based surveys (e.g., Kenyon & Bromley 2012; Schlichting et al. 2013).

Here, we consider whether the size distribution derived from craters on Charon is consistent with expectations for a collisional cascade, where high velocity impacts continually erode the material from 1–100 km objects. Analytical equilibrium size distributions for collisional cascades share features with the *New Horizons* results; we derive physical parameters for cascades that broadly match the Charon cratering record. Numerical simulations with similar parameters agree rather well with the analytic predictions. Comparing the theoretical results with the *New Horizons* observations, solids with the bulk strength of weak to normal ice have size distributions that resemble the data. Because the time scale for generating these size distributions is only 20–30 Myr (100–300 Myr) at 25 au (45 au), the impactors on Charon are plausibly derived from a collisional cascade during the formation of the Solar System.

Although it is possible to construct a model that follows the time evolution of the population of TNOs, the impact rate of these TNOs on Pluto-Charon (e.g., Greenstreet et al. 2015; Bierhaus & Dones 2015), and the dynamical evolution of the gas giant planets (e.g., Malhotra 1993, 1995; Levison & Morbidelli 2003; Levison et al. 2008), we focus on a simpler issue. The goal is to understand how the features in the TNO size distribution depend on initial conditions, model parameters and time. By eliminating model size distributions that do not match the *New Horizons* data, we limit the space of plausible models to be investigated in a more detailed evolutionary calculation. We return to issues involving the impact rate and the long-term dynamical evolution of the Solar System in §6.

To set the stage for this study, we begin with an observational background (§2). After reviewing previous theoretical approaches (§3), we consider whether analytic (§4) or numerical (§5) collisional cascade models can match the *New Horizons* observations. After discussing the implications of this analysis (§6), we conclude with a brief summary (§7).

2. OBSERVATIONAL BACKGROUND

The discovery of the Kuiper Belt dramatically changed our understanding of the extent and dynamical structure of the Solar System. Data from the first few surveys (e.g., Luu & Jewitt 1988; Jewitt & Luu 1993, 1995; Williams et al. 1995; Irwin et al. 1995; Jewitt et al. 1996; Luu et al. 1997; Luu & Jewitt 1998; Trujillo et al. 2000, 2001a) detected ‘Kuiper belt objects’ (KBOs) (i) in the 3:2 resonance with Neptune, (ii) in roughly circular orbits just outside Neptune’s orbit, and (iii) in very elliptical orbits ($e \gtrsim 0.5$) with perihelia close to Neptune’s orbit. Subsequent deep imaging programs revealed an exquisite dynamical richness among Solar System objects orbiting beyond Neptune (e.g., Gladman et al. 2002; Luu & Jewitt 2002; Brown et al.

2004; Gladman et al. 2008; Petit et al. 2011; Bernardinelli et al. 2020). Today, there are ~ 3500 TNOs with semimajor axis $a \gtrsim 30$ au listed in the database of the International Astronomical Union’s Minor Planet Center.

Dynamical classifications of KBOs and TNOs are based on their current orbital elements and the gravitational influence of the four gas giant planets (e.g., Levison 1996; Duncan & Levison 1997; Gladman et al. 2002; Dones et al. 2004; Morbidelli & Levison 2004; Elliot et al. 2005; Delsanti & Jewitt 2006; Gladman et al. 2008; Petit et al. 2011; Khain et al. 2020). Many TNOs are in orbital resonance with Neptune. The 3:2 (Plutinos), 5:3, 7:4, and 2:1 (Twotinos) resonances are well-populated (e.g., Chiang et al. 2003a; Petit et al. 2011; Li et al. 2014a,b; Volk et al. 2016; Li et al. 2020); recent discoveries include TNOs in the 21:5 (Holman et al. 2018), the 9:2 (Bannister et al. 2016a), and the 9:1 (Volk et al. 2018) resonances with Neptune. Various non-resonant TNOs have orbits with perihelion distances q close to or inside Neptune’s semimajor axis, $a_N \approx 30$ au. The scattering (or scattered) disk objects (SDOs) have $a \gg a_N$. The SDOs are distinguished from Centaurs, which have $a < a_N$, $q > 7.35$ au, and a Tisserand parameter,

$$T_J = \frac{a_J}{a} + 2 \left(\frac{a}{a_J} (1 - e^2) \right)^{1/2} \cos \iota > 3, \quad (1)$$

where a_J is the semimajor axis of Jupiter, and ι is the orbital inclination of the Centaur or SDO. On more distant orbits, detached TNOs have $q \gtrsim a_N$ and $e \gtrsim 0.24$; inner Oort cloud objects have $a \gtrsim 2000$ au.

The classical KBOs are non-resonant TNOs on fairly low e orbits. Gladman et al. (2008) identified three dynamical classes: inner ($a < 39.4$ au; orbit interior to the 3:2 resonance with Neptune), main ($a \approx 42\text{--}48$ au), and outer ($a > 48.4$ au and $e < 0.24$; exterior to the 2:1 resonance with Neptune). Main classical objects are often call ‘cubewanos’ after the first known KBO, 1992 QB₁ (Jewitt & Luu 1993), and are divided into a ‘hot’ component ($\iota > 5^\circ$) and a ‘cold’ component ($\iota < 5^\circ$). Petit et al. (2011) isolated three components of the main classical belt – hot, kernel, and stirred – with specific ranges in a , e , and ι (see also Petit et al. 2017). More recent observations confirm the kernel and indicate the cold classical belt extends beyond the 2:1 resonance (Bannister et al. 2016b, 2018).

Measuring the size distribution(s) of TNOs from deep imaging observations requires several steps (e.g., Jewitt et al. 1998; Luu & Jewitt 1998; Trujillo et al. 2001b; Luu & Jewitt 2002; Bernstein et al. 2004; Petit et al. 2006; Fuentes & Holman 2008; Fraser et al. 2008; Gil-Hutton et al. 2009; Fraser & Kavelaars 2009; Fuentes et al. 2009, and references therein). In the most direct approach, analysis of large samples of TNOs with good orbits yields $\Sigma(< H)$ (in units of deg^{-2}), the cumulative sky surface density brighter than an absolute magnitude H^1 . Converting the frequency of absolute magnitudes to the frequency of object radii r requires knowledge of the geometric albedo p . If every TNO is a diffuse disk reflector, the relation between absolute magnitude, geometric albedo, and radius is straightforward (e.g., Harris & Harris 1997):

$$r \approx \frac{665}{p_\lambda^{1/2}} 10^{-0.2 H_\lambda} \text{ km}. \quad (2)$$

Although H is derived for several wavelengths λ , the albedo is often quoted in the V-band, p_V .

Early observations of TNOs suggested Σ followed a simple power law (e.g., Jewitt et al. 1998; Luu & Jewitt 1998; Chiang & Brown 1999; Sheppard et al. 2000; Trujillo et al. 2001b; Gladman et al. 2001)

$$\log \Sigma(< H) = \alpha (H - H_0), \quad (3)$$

¹Usually, H is measured in the broadband V, R, or r filters; sometimes, the bluer g filter is used.

where α is the slope and H_0 is a reference brightness. Deeper surveys for objects with $H \lesssim 12$ –13 revealed a break (or ‘knee’) in the power-law and a shallower slope to larger H (e.g., Bernstein et al. 2004; Petit et al. 2006; Fraser et al. 2008; Fuentes & Holman 2008; Fraser & Kavelaars 2009; Fuentes et al. 2009). Although the surface density is often continuous across the break, several analyses favor a ‘divot’ model, where the surface density for magnitudes just below the break is significantly smaller than the surface density above the break (e.g., Shankman et al. 2013, 2016; Alexandersen et al. 2016; Lawler et al. 2018). Combining these approaches into a single set of expressions, the cumulative sky surface density is

$$\Sigma(< H) = \Sigma_b \delta_b 10^{\alpha_b (H - H_b)} + \Sigma_f \delta_f (10^{\alpha_f (H - H_b)} - 1), \quad (4)$$

where H_b is the absolute magnitude at the break, Σ_b (Σ_f) is the surface density of bright (faint) objects at the break, α_b (α_f) is the power-law slope for bright (faint) objects above (below) the break, and

$$\delta_{b,f} = \begin{cases} 0, & H \leq H_b \\ 1, & H \geq H_b \end{cases} \quad (5)$$

To make a stronger connection to several published analyses, we follow Shankman et al. (2013, 2016) and define the contrast

$$c_{bf} = \frac{\Sigma_b}{\Sigma_f}. \quad (6)$$

When $c_{bf} = 1$, the surface density distribution is continuous across the break. Models with $c_{bf} > 1$ have a pronounced divot at the break.

Deriving $n(r)$, the differential size distribution of TNOs as a function of radius r , from fits to the surface density distribution requires an expression for the albedo $p_V(r)$. When $n(r) \propto r^{-q}$ and $p_V(r) \propto r^{-\beta}$ (e.g. Jewitt et al. 1998; Fraser et al. 2008), there is a simple relation between q , α , and β :

$$q = 5 \alpha (1 - \beta/2) + 1. \quad (7)$$

For a cumulative size distribution, $n(< r)$ or $n(> r)$, with power-law index q' , $q' = q - 1$. Measurements of α (from large magnitude-limited surveys of TNOs) and β (from mid-IR and far-IR observations that constrain the reflected and thermal emission of TNOs) yield q .

Over the past decade, analyses of $\Sigma(H)$ yield a fairly consistent picture for the location of the break and the slope of the magnitude distribution above the break (e.g., Petit et al. 2011; Gladman et al. 2012; Shankman et al. 2013; Fraser et al. 2014; Adams et al. 2014; Schwamb et al. 2014; Alexandersen et al. 2016; Shankman et al. 2016; Lawler et al. 2018). For the hot classical KBOs, the SDOs, and the Plutinos, $\alpha_b \approx 0.8$ –1.0 and $H_b \approx 7.7$ –8.3. The bright-end slope for the cold classical KBOs is much steeper, $\alpha_b \approx 1.2$ –1.5. Fraser et al. (2014) derive a brighter magnitude for the break that has not been tested by other analyses of the cold KBOs.

Curiously, the bright-end slope for KBOs in the 2:1 and 5:3 resonances with Neptune is similar to that of other dynamically hot objects, $\alpha_b \approx 0.9$ –1 (Adams et al. 2014). However, the $\alpha_b \approx 1.3$ for KBOs in the 5:2 and 7:4 resonances is closer to the slope derived for the cold classical KBOs. With many fewer objects than the other TNO populations, the errors in the slopes for the size distributions of objects in the 5:2 and 7:4 resonances are significant. Larger samples might establish whether these differences in α_b are real.

Independent analyses also agree on the overall population of the different classes of TNOs. The SDOs are the most populous group, with $\sim 37,500$ objects brighter than $H = 8$ (Shankman et al. 2013; Adams et al. 2014; Shankman et al. 2016; Lawler et al. 2018). There are $\sim 20,000$ classical KBOs, with ~ 400 in the

inner belt and the rest roughly evenly divided between the main belt and the outer belt (Petit et al. 2011; Adams et al. 2014). Within the main classical belt, $\sim 10\%$ lie within the kernel; the remainder are roughly evenly divided between the hot and stirred populations.

For many resonances, the relative populations are plagued by small number statistics (e.g., Adams et al. 2014; Bannister et al. 2016a; Volk et al. 2018; Bannister et al. 2018). However, statistics for the Plutinos suggest ~ 3000 objects with $H \leq 8$ (e.g., Gladman et al. 2012; Adams et al. 2014; Volk et al. 2016; Alexandersen et al. 2016). The 2:1 (~ 1500) and the 5:2 (~ 1000) are the next most populous. The number of TNOs in the 5:2 resonance is larger than predicted by early dynamical models (e.g., Chiang et al. 2003b; Levison et al. 2008); recent analyses address this issue (Malhotra et al. 2018; Yu et al. 2018).

Despite the general agreement on α_b and H_b , the range of possibilities for α_f and c_{bf} is much broader (e.g., Fraser et al. 2014; Shankman et al. 2013; Alexandersen et al. 2016; Shankman et al. 2016; Lawler et al. 2018). Results for the cold KBOs suggest $\alpha_f \approx 0.2$ and $c_{bf} = 1$. Analyses of data for Plutinos and SDOs yield larger slopes, $\alpha_f \approx 0.2$ – 0.6 , and various contrasts, $c_{bf} \approx 1$ – 10 . As outlined by Shankman et al. (2013, 2016) for the SDOs, the population at $H \approx 15$ – 20 is constrained by the population of Jupiter family comets which are believed to originate among the SDOs (and perhaps the Plutinos; Levison & Duncan 1997; Emel’yanenko et al. 2004, 2005; Volk & Malhotra 2008; Di Sisto et al. 2009; Brassier & Wang 2015). If the Plutino/SDO size distribution consists only of two power laws, current data favor models with $\alpha_f \approx 0.5$ – 0.6 and $c_{bf} \approx 3$ – 6 . However, a three component size distribution enables models with smaller α_f and $c_{bf} \approx 1$ for $H \approx 8$ – 12 , providing the slope at $H > 12$ becomes steep enough to match the constraints for Jupiter family comets at much fainter magnitudes.

Combined with ground-based observations, data from the *Herschel* and *Spitzer* satellites enable direct measurements of the geometric albedo p_V and the radii r of TNOs (e.g., Vilenius et al. 2012, 2014; Duffard et al. 2014; Kovalenko et al. 2017; Vilenius et al. 2018). Despite small samples limited to the largest TNOs, the distribution of measured albedo is very broad, $p_V \approx 0.03$ – 0.80 ; the albedo correlates with orbital inclination but not size. Typical values for the hot KBOs, $p_V \approx 0.09$, are smaller than the albedos for cold KBOs, $p_V \approx 0.14$. However, the Haumea family (and other TNOs like Makamake) have $p_V \gtrsim 0.5$.

Converting the brightness of TNOs at the break in the *surface density* distribution, $H_b \approx 7.7$ – 8.3 , to a radius for TNOs at the break in the *size* distribution requires a geometric albedo. For simplicity, we assume the albedo is independent of wavelength in the optical. With a typical $p_V \approx 0.10$, the faintest TNOs directly observed in ground-based or space-based surveys have a radius $r \approx 10$ km; the break occurs at a radius $r_b \approx 45$ – 60 km. Reducing (increasing) p_V to 0.05 (0.15) raises (lowers) the break radius to ~ 65 – 85 km (30 – 45 km). Because the range of albedos is much larger than the uncertainty in H_b , the uncertainty in r_b is dominated by the uncertainty in the adopted p_V .

With $\beta \approx 0$ in the relation $p_V(r) \propto r^{-\beta}$, the slope q of $n(r)$ depends only on α (eq. 7). For bright objects detected in large, ground-based surveys, $q_b \approx 5$ – 6 for hot KBOs, Plutinos, and SDOs; $q_b \approx 7$ – 9 for cold KBOs. These slopes are larger than results from the more direct measurements of smaller samples from *Herschel* and *Spitzer*: $q \approx 4.2$ for the Haumea family, $q \approx 3.3$ for hot KBOs with $r \approx 50$ – 250 km, and $q \approx 6$ for cold KBOs with $r \approx 80$ – 150 km (Vilenius et al. 2014, 2018). Still, the trends are similar: the slope for hot KBOs (including SDOs and Plutinos) is much shallower than for cold KBOs. Among fainter KBOs, the preferred $\alpha_f \approx 0.5$ – 0.6 implies $q_f \approx 3.5$ – 4 (Shankman et al. 2013; Alexandersen et al. 2016; Shankman et al. 2016). Allowing the smaller $\alpha = 0.2$ – 0.4 from some studies results in $q_f \approx 2$ – 3 .

Results from other approaches for deriving α_f provide an interesting contrast with the analyses of the ground-based optical surveys. The $q_f \approx 3.5$ – 4 needed to match the optical data at $H \approx 8$ – 11 and the

postulated source population of Jupiter family comets at $H \approx 17$ is identical to the $q_f \approx 3.8$ – 3.9 derived from several detections of stellar occultations by 0.25–0.50 km KBOs (Schlichting et al. 2009, 2012; Liu et al. 2015). Lack of detections in another occultation survey implies $q \lesssim 3.3$ – 3.8 (Bianco et al. 2010; Zhang et al. 2013). However, number counts of craters on Pluto and Charon from *New Horizons* suggest a shallower $q_f \approx 3$ ($\alpha_f \approx 0.4$) at $r \approx 1$ – 10 km and an even shallower $q_f \approx 1.75$ ($\alpha_f \approx 0.15$) at $r \approx 0.1$ – 1 km (Singer et al. 2019).

Fig. 1 illustrates the tension between the ground-based and the *New Horizons* measurements of TNO size distributions. In this Figure, the y -axis plots $R(D) = N/(D^{-3}(D_{up} - D_{low}))$ as in Singer et al. (2019); N is the number of objects in a mass bin with maximum diameter D_{up} , minimum diameter D_{low} , and central diameter D . We adopt a simple relation between impactor diameter D and crater diameter, D_c , $D = D_c/6.25$, which neglects the slightly steeper than linear relation between D and D_c and represents a compromise among relations for different materials (e.g., Holsapple 1993; Housen & Holsapple 2011; Singer et al. 2013; Singer & Stern 2015; Singer et al. 2019). In Figures derived from analytic theory or numerical calculations later in this paper, we use the radius $r = D/2$ and $r = (r_{low}r_{up})^{1/2}$; $R(r) = N/(r^{-3}(r_{up} - r_{low}))$ and $R(D) = 4R(r)$. The *shape* of the size distribution is then independent of r or D . To avoid confusion, we use *size distribution* to refer to $n(r)$, $R(r)$, and $R(D)$; the slope q is always derived from $n(r) \propto r^{-q}$. In systems with $q = 3$, $R(r)$ is independent of r .

To derive an appropriate $R(r)$ from ground-based observations, we consider several broken power-laws for TNOs with $H \leq 12$ (indicated by the thick dashed lines). To place these power-laws on the same scale as the *New Horizons* data, we adopt $R = 0.06$ at $r = 50$ km for the TNO power-laws. With this normalization, the *New Horizons* measurements at 1–10 km fall well below the $q = 3.5$ – 4.0 needed to match the occultation data (the large ‘+’ along the upper dashed line) and to produce enough Jupiter family comets with $H \approx 17$ ($r \approx 1$ km). Adopting a different normalization, $R \approx 0.4$ – 0.5 at 4–5 km, allows a crude match between the ground-based and *New Horizons* data at 1–10 km; however, the *New Horizons* data at 0.1–1 km still fall well below the level required to agree with the occultation measurements.

At $r \approx 0.1$ – 1 km, the slope from the *New Horizons* data is at the lower end of the allowed ranges derived from cold KBOs and some model fits to observations of much larger Plutinos and the SDOs with $H \leq 12$ and $r \gtrsim 10$ – 20 km for $p_V \approx 0.10$ (Fraser et al. 2014; Alexandersen et al. 2016; Shankman et al. 2016; Lawler et al. 2018). Although it is possible to consider a normalization for the TNO power-laws that places the *New Horizons* data at 0.1–1 km along the $q = 2$ branch of the figure, this choice leaves the *New Horizons* data at 1–10 km even farther from the limits derived from Jupiter family comets and occultations.

In these examples, the two broken power-laws have no divot at the break in the size distribution at 50 km ($c_{bf} = 1$). Shifting the $q = 2.00$ and $q = 3.75$ power-laws vertically downward by a factor of 10 allows a match to the *New Horizons* data at 1–2 km and roughly agrees with the *New Horizons* data at 2–10 km. However, the $c_{bf} \approx 10$ implied by this shift is larger than the $c_{bf} \approx 3$ – 6 derived in some analyses of ground-based observations for KBOs with $r \gtrsim 10$ – 20 km (e.g., Alexandersen et al. 2016; Shankman et al. 2016; Lawler et al. 2018). With this shift, there is still a stark disagreement between the *New Horizons* data at 0.1–1 km and the slope required to match ground-based observations of $r \gtrsim 10$ – 20 km TNOs and the frequency of Jupiter family comets with radii $r \sim 1$ km.

The results from *New Horizons* resemble size distributions derived from numerical calculations of colli-

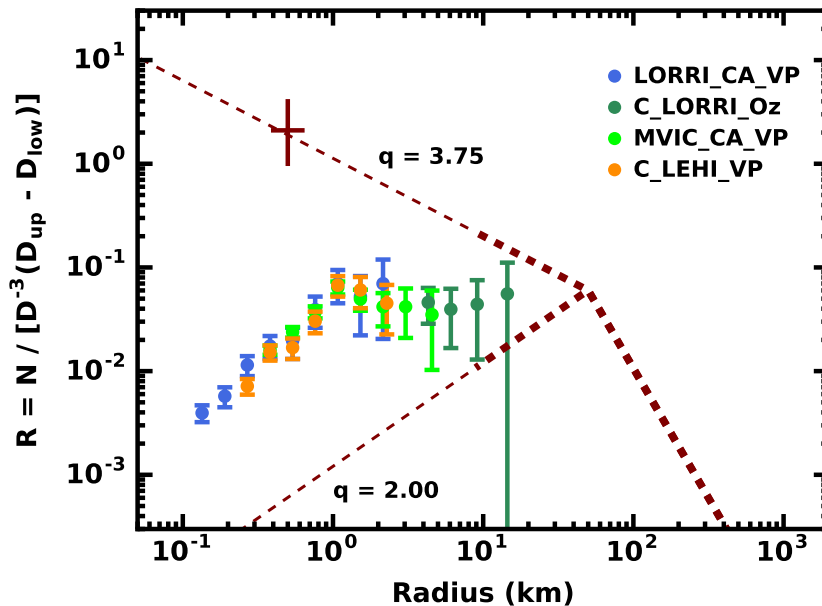


Fig. 1.— Comparison of number counts for the radii of impactors derived from craters detected on *New Horizons* images of Charon (filled points with error bars; Singer et al. 2019) with broken power-law size distributions derived from ground-based observations of TNOs (dashed lines). The impactor diameter D is $D = D_c/6.25$, where D_c is the crater diameter. Dashed lines are normalized to yield an R value at $r \sim 50$ km which roughly matches the *New Horizons* data at $r \sim 10$ – 20 km. The legend indicates the combination of instrument and geological feature for each *New Horizons* data set (Singer et al. 2019). The slopes of the two broken power-laws match observations for SDOs and other TNOs larger than the ‘break radius’ at $r \approx 50$ km and span the range of possible slopes for smaller objects below the break (e.g., Fraser et al. 2014; Lawler et al. 2018). Thicker lines cover the approximate size range detected by ground-based observations of SDOs; thinner lines are extrapolations. The + along the upper dashed line represents the constraints derived from occultation observations.

sional cascades (e.g., Kenyon & Bromley 2004b, 2012). In many cascades,

$$n(r) \propto \begin{cases} r^{-q_s} & r < r_s \\ r^{-q_i} & r_s \leq r \leq r_l \\ r^{-q_l} & r > r_l \end{cases} \quad (8)$$

where $r_l \gtrsim 10$ – 20 km, $r_s \approx 0.1$ – 1 km, $q_l \gtrsim 3.5$, $q_s \approx 3.5$ – 4.0 , and $q_i \approx 0$ – 3 . A goal of this study is to establish whether we can derive the physical characteristics of a cascade that yields a $n(r)$ which matches the *New Horizons* results.

One way to restore the balance between the ground-based and *New Horizons* analyses is to associate most of the Pluto–Charon impactors with hot KBOs from the classical belt and Plutinos and to place the source of Jupiter family comets mostly within the SDOs. Indeed, Greenstreet et al. (2015) show that four TNO populations (hot and stirred classical TNOs, classical outer TNOs, and Plutinos) contribute roughly equally to impactors on Pluto–Charon (see also Bierhaus & Dones 2015). TNOs in other dynamical classes should

impact Pluto–Charon at much lower rates. Completed prior to the *New Horizons* flyby of Pluto–Charon, both studies assumed a variety of size distributions for small TNOs. Our goal is to explore the origins of the features in the size distribution of TNOs. The next section briefly reviews analytic and numerical models that attempt to explain these features.

3. THEORETICAL BACKGROUND

Soon after the discovery of 1992 QB₁, theorists began to consider the formation and long-term collisional evolution of TNOs. Early efforts examined the growth of the largest KBOs from 1–10 km planetesimals (e.g., Stern 1995, 1996; Stern & Colwell 1997a; Kenyon & Luu 1998, 1999a; Durda & Stern 2000; Kenyon 2002) or the collisional erosion of $n(r)$ and the total mass in TNOs (e.g., Davis & Farinella 1997; Stern & Colwell 1997b). These investigations established that (i) the time scale for 100–1000 km KBOs to grow from a swarm of 1–10 km planetesimals within a smooth disk or ring is 20–100 Myr, (ii) once large KBOs form, destructive collisions can remove $\gtrsim 90\%$ of the initial mass in the Kuiper belt, (iii) the current $n(r)$ for KBOs has had a roughly constant shape for ~ 4 Gyr, and (iv) small TNOs with $r \lesssim 50$ –100 km are fragments of high velocity impacts. Initial fits of the models to observations of the size distribution at large sizes were encouraging (e.g., Kenyon & Luu 1999b).

Since these pioneering studies, several analytic treatments have focused on the physical origin of the break in the power-law size distribution at $r \approx 30$ –100 km (e.g. Kenyon & Bromley 2004b; Pan & Sari 2005; Fraser 2009). We follow previous work and compare Q_b the binding energy of two colliding TNOs with their center-of-mass collision energy per unit mass

$$Q_c = 0.5 \left(\frac{m_1 m_2 v^2}{m_{12}^2} \right) = \frac{qv^2}{2(1+q)^2}, \quad (9)$$

where v is the collision velocity, m_1 and $m_2 = \theta m_1$ ($\theta \leq 1$) are the mass of two colliding TNOs, and $m_{12} = m_1 + m_2$. When Q_c is much smaller than Q_b , the collision produces a more massive large object. However, if Q_c is much larger than Q_b , then the collision is *catastrophic* and leaves behind a ‘largest remnant’ with a mass less than half of m_{12} (e.g., Weidenschilling 1974; Greenberg et al. 1978; Wetherill 1980, and references therein).

Although there are several distinct but complementary approaches to calculating Q_b (e.g., Greenberg et al. 1984; Davis et al. 1985; Wetherill & Stewart 1989; Housen & Holsapple 1990; Wetherill & Stewart 1993; Holsapple 1994; Davis & Farinella 1997; Weidenschilling 1997; Benavidez & Campo Bagatin 2009; O’Brien & Greenberg 2003; Campo Bagatin & Benavidez 2012), it is convenient to define the collision energy required to disperse half of m_{12} beyond the gravitational reach of the colliding pair:

$$Q_D^* = Q_s r^{e_s} + Q_g \rho r^{e_g}, \quad (10)$$

where ρ is the mass density of the TNOs and (Q_s, Q_g, e_s, e_g) are model parameters (e.g., Benz & Asphaug 1999; Leinhardt & Stewart 2012). In this expression, the first (second) term is the strength (gravity) component of the binding energy. These two elements are comparable for $r \approx 0.1$ km. When Q_c is smaller (larger) than Q_D^* , collisions between equal mass objects ($\theta \approx 1$) are accretive (destructive) and large objects grow (diminish) with time. When $\theta \ll 1$ and $Q_c = \theta v^2/2$, high velocity collisions typically remove a mass from the higher mass ‘target’ that exceeds the mass in the much smaller ‘projectile’. In these ‘cratering’ collisions, massive particles gradually lose mass over time.

Setting $Q_c = Q_D^*$ for $m_1 = m_2$ ($q = 1$) yields a relation between v , r , ρ , Q_g , and e_g for large objects (Kenyon & Bromley 2004b; Pan & Sari 2005):

$$r_b = \left(\frac{v^2}{8\rho Q_g} \right)^{1/e_g}. \quad (11)$$

Collisions between pairs of equal mass objects with $r \leq r_b$ generate fragments; those with $r > r_b$ produce a larger merged object. Adopting typical values $Q_g \approx 0.1\text{--}3 \text{ erg g}^{-2} \text{ cm}^{3-e_g}$ and $e_b \approx 1.2\text{--}1.4$ (Benz & Asphaug 1999; Leinhardt & Stewart 2012), the collision velocity required to match the observed $r_b \approx 50 \text{ km}$ is $v \approx 1 \text{ km s}^{-1}$ for $\rho \approx 1.0\text{--}1.5 \text{ g cm}^{-3}$. With orbital velocities, $v_K \approx 4\text{--}5 \text{ km s}^{-1}$ and eccentricities, $e \approx 0.05\text{--}0.2$, TNOs at $a \approx 30\text{--}50 \text{ au}$ have typical relative velocities comparable to the required v . Thus, the observed r_b is reasonably consistent with theoretical expectations.

Several recent numerical calculations support this result (e.g., Krivov et al. 2005; Charnoz & Morbidelli 2007; Benavidez & Campo Bagatin 2009; Fraser 2009; Campo Bagatin & Benavidez 2012; Kenyon & Bromley 2012; Schlichting et al. 2013). When the collision velocities are appropriate for present-day TNOs, the shape of the TNO size distribution depends on (i) the initial $n(r)$, (ii) the Q_D^* parameters, and (iii) time. Calculations extending over 0.5–4.5 Gyr result in $r_b \approx 50 \text{ km}$ for nominal values of Q_g and e_g . Plausible ranges in Q_g and e_b yield factor of two variations in r_b . Large TNOs with $r \gtrsim r_b$ maintain their initial size distribution. Smaller TNOs with $r \lesssim r_b$ have wavy size distributions with peaks and valleys that depend on v , Q_g , and e_b (see also Campo Bagatin et al. 1994; O’Brien & Greenberg 2003; Krivov et al. 2005; Wyatt et al. 2011). At the smallest sizes, $r \lesssim 0.1\text{--}1 \text{ km}$, $n(r)$ follows a power law with $q \approx 3\text{--}4$.

Despite the general agreement on how the break radius and the size distribution change with input parameters, the calculations derive very different size distributions for $r \approx 0.1\text{--}100 \text{ km}$. Several display clear divots (e.g., Benavidez & Campo Bagatin 2009; Fraser 2009); others do not (e.g., Campo Bagatin & Benavidez 2012; Schlichting et al. 2013). Although waviness at $r \approx 1\text{--}100 \text{ km}$ is characteristic, none obviously match the size distribution derived from the *New Horizons* cratering record.

4. COLLISIONAL CASCADES: ANALYTICAL RESULTS

4.1. Background

To explore the possibilities for understanding the *New Horizons* observations, we begin with an analysis of equilibrium size distributions for the TNO population. In any model, $n(r)$ depends on the rates collisions remove objects with a range of sizes $r \lesssim r_b$ and add debris with a range of sizes $r \ll r_b$. When these rates are equal, $n(r)$ reaches a steady state where the shape remains fixed and the absolute level slowly declines with time. Analytic results show how the equilibrium shape of $n(r)$ depends on Q_c and Q_D^* (see the discussion in Wyatt et al. 2011). Numerical calculations designed to achieve a steady state generate wavy size distributions that resemble the analytic shapes reasonably well (e.g., Kenyon & Bromley 2016, 2017). Because all of the recent numerical simulations of the TNO populations suggest steady-state size distributions over some range of sizes, it is reasonable to investigate whether analytic steady-state size distributions can match the *New Horizons* observations.

For nearly two decades, analytic theories of collisional cascades have been developed to explain the long-term evolution of debris disks (e.g., Wyatt & Dent 2002; Dominik & Decin 2003; Wyatt et al. 2007a,b; Wyatt 2008; Kennedy & Wyatt 2011; Wyatt et al. 2011; Kenyon & Bromley 2016; Kenyon et al. 2016;

Kenyon & Bromley 2017). Defining r_{max} as the radius of the largest object in a swarm of solids, a cascade of catastrophic collisions produces a flow of material from r_{max} to r_{min} the radius of the smallest object in the swarm. Sometimes $r_{min} = 0$ (e.g., Dohnanyi 1969; Williams & Wetherill 1994). More often, r_{min} is the minimum size stable against radiation pressure from the central star (e.g., Burns et al. 1979; Artymowicz 1988; Wyatt 2008). For the Sun, $r_{min} \approx 1 \mu\text{m}$.

As the cascade proceeds, r_{max} and the mass in solids M_d decline with time t (Wyatt & Dent 2002; Dominik & Decin 2003; Wyatt 2008; Kenyon & Bromley 2017):

$$r_{max} = \frac{r_0}{(1 + t/\tau_0)^\gamma} \quad (12)$$

$$M_d = \frac{M_0}{(1 + t/\tau_0)^\gamma}, \quad (13)$$

where r_0 is the initial radius of the largest object, M_0 is the initial mass in solids with $r \leq r_0$, and $\gamma \geq 1$ is a constant (Kenyon & Bromley 2017). In these expressions, t_0 sets the collision time

$$t_0 = \frac{r_0 \rho P}{12\pi \Sigma_0} \quad (14)$$

for solids with semimajor axis a , orbital period P , and initial surface density $\Sigma_0 = M_0/2\pi a \Delta a$ within an annulus of width Δa . Defining $\alpha = -(M_0/t_0)\dot{M}_d^{-1}$, $\tau_0 = (\gamma + 1)\alpha t_0$.

In eqs. 12–13, the decline of r_{max} and M_d depends on α and γ , which encode the evolution of the cascade as a function of v^2/Q_D^* , the ratio of the center-of-mass collision energy to Q_D^* . When $v^2/Q_D^* \approx 8$, τ_0 is large; the cascade slowly reduces r_{max} and M_0 . Increasing v^2/Q_D^* decreases τ_0 . More energetic collisions produce more rapid changes in r_{max} and M_0 .

The simplest analytic theory assumes that catastrophic collisions set the equilibrium $n(r)$. Cratering collisions with $Q_c < Q_D^*$ are ignored (Wyatt et al. 2011). The model also assumes that all particles have the same collision velocity v . Within a logarithmic grid of particles with indices $k = 1$ to $k = N$ where $r_1 < r_N$, the mass loss rate of particles is assumed to be independent of the bin. The mass contained in the bin is then (Wyatt et al. 2011):

$$M_k = C_0 R_k^{-1}, \quad (15)$$

where C_0 is an arbitrary constant (see also eq. 15 of Wyatt et al. 2011). The sum R_k is the rate of collisions which disperse at least half of the combined mass of a pair of colliding particles,

$$R_k = C_1 \sum_{i=1}^{i=k} \epsilon_{ik} M_i (r_i + r_k)^2 / r_i^3, \quad (16)$$

where C_1 is another constant. When catastrophic collisions dominate

$$\epsilon_{ik} = \begin{cases} 0 & Q_c < Q_D^* \\ 1 & Q_c \geq Q_D^* \end{cases} \quad (17)$$

Although it is straightforward to develop an iterative technique to solve this set of equations (Wyatt et al. 2011), Kenyon & Bromley (2016) proposed a recursive solution. When $k = 1$, $R_1 = 4C_1 M_1 / r_1$. Thus, $M_1^2 = C_0 / 4C_1 r_1$. For $k \geq 2$, R_k is a sum over terms with known M_i and one term with M_k :

$$R_k = 4C_1 M_k / r_k + C_1 \sum_{i=1}^{i=k-1} \epsilon_{ik} M_i (r_i + r_k)^2 / r_i^3. \quad (18)$$

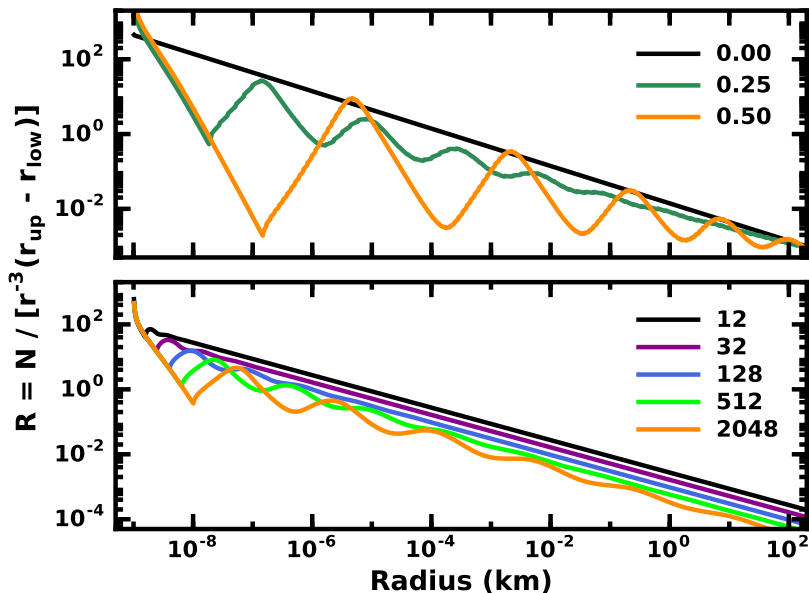


Fig. 2.— Equilibrium $R(r)$ derived from the analytic model described in the text. *Lower panel:* Results for constant Q_D^* and the values of v^2/Q_D^* listed in the legend. Models with larger v^2/Q_D^* have wavier size distributions. *Upper panel:* Results for constant $Q_D^* = 8$ (black curve) and $Q_D^* \propto r^{e_q}$ with $e_q = 0.25$ (green curve) and $e_q = 0.50$ (orange curve). Systems with larger e_q have shallower slopes and wavier size distributions than those with smaller e_q .

Setting R_{ki} equal to the second term in eq. 18, the quadratic equation

$$4C_1 M_k^2 + R_{ki} M_k - C_0 = 0, \quad (19)$$

has only one possible solution with $M_k > 0$.

4.2. Simple Examples

To calculate an equilibrium $n(r)$, we have several options. Setting $v^2/Q_D^* = \text{constant}$ for all sizes allows us to recover previous analytic results (e.g., Dohnanyi 1969; Williams & Wetherill 1994; O’Brien & Greenberg 2003; Pan & Sari 2005). With $r_{min} = 0$, $n(r)$ has the standard power-law slope $q = 3.5$. When $r_{min} = 1 \mu\text{m}$, $n(r)$ is wavy with an overall slope $q = 3.5$ (Fig. 2, lower panel; see also Campo Bagatin et al. 1994; O’Brien & Greenberg 2003; Pan & Sari 2005; Wyatt et al. 2011). The amplitude of the wave grows with increasing collision energy, from a modest wave when $v^2/Q_D^* = 12$ to a pronounced wave when $v^2/Q_D^* = 2048$.

When Q_D^* is a function of particle radius, the characteristic slope of the size distribution and the waviness change dramatically (e.g., O’Brien & Greenberg 2003). For a simple power-law function $Q_D^* \propto r^{e_q}$, the power-law slope is $q = (21 + e_q)/(6 + e_q)$ (O’Brien & Greenberg 2003; Pan & Schlichting 2012). In the strength regime of eq. 10, standard values for $e_s \approx 0$ to -0.5 yield $q = 3.50$ – 3.72 . In the gravity regime, $e_g \approx 1.2$ – 1.4 implies $q \approx 3.13$ – 3.03 ; $n(r)$ is then shallower than the standard $q = 3.5$ power-law.

The upper panel of Fig. 2 illustrates the changing properties of $R(r)$ when e_q is positive. For each example, we normalize the ratio of Q_c to Q_D^* at $v^2/Q_D^* = 8$ for collisions between equal mass objects with $r = r_{max}$. For all $r < r_{max}$, $v^2/Q_D^* > 8$; collisions between smaller equal-mass objects always produce catastrophic collisions. The black curve in the Figure has $e_q = 0$ and the standard slope $q = 3.5$. When $e = 0.25$ (green curve), $n(r)$ is shallower with an average $q = 3.4$. A system with a larger $e_q = 0.5$ has an even shallower size distribution with an average $q = 3.3$. For $e_q > 0.5$, $n(r)$ is wavier and has a smaller average slope. Once $e_q \gtrsim 1$, $n(r)$ is dominated by large amplitude waves; the average slope only crudely characterizes the shape of the size distribution.

The waviness of $n(r)$ clearly depends on e_q . When $v^2/Q_D^* = 8$ and $e_q = 0$, waviness due to the small-size cutoff is negligible. At larger e_q , v^2/Q_D^* monotonically increases from 8 at $r = r_{max}$ to $v^2/Q_D^* = 8(r_{max}/r_{min})^{e_q}$ at $r = r_{min}$. Adopting $r_{max} = 500$ km and $r_{min} = 1$ μm , $v^2/Q_D^* \approx 6700$ (5.7×10^6) at $r = r_{min}$ for $e_q = 0.25$ (0.50). Compared to the examples where v^2/Q_D^* is a constant (e.g., $v^2/Q_D^* = 12$ –2048; Fig. 2, lower panel), the waves in the upper panel of Fig. 2 are much larger. With large ranges in v^2/Q_D^* likely in real systems, these examples show how the parameters in the relation for Q_D^* impact the size distribution for constant collision velocity.

The slope and waviness of $n(r)$ also depend on how v varies with particle radius (Pan & Schlichting 2012). When the collision velocity has a power-law relation, $v \propto r^{e_v}$, imposing mass conservation yields a slope $q = (21 + e_q - 2e_v)/(6 + e_q - 2e_v)$. With v^2/Q_D^* as the basic parameter setting the slope, the twin factors of two in this expression come from the v^2 term; the negative sign results from v_c^2 in the numerator instead of the denominator of v^2/Q_D^* . In the upper panel of Fig. 2, a system with $v^2/Q_D^* = 8$ at $r = r_{max}$ and $e_v = e_q = 0$ recovers $n(r)$ with the standard slope $q = 3.5$. Setting $e_v = -e_q/2 = -0.125$ (green curve) or $= -0.250$ (orange curve) yields the same wavy $n(r)$ and a shallower general slope from r_{min} to r_{max} . Adopting a positive e_v results similarly wavy $n(r)$ with steeper slopes from r_{min} to r_{max} .

In these examples, the waves result from the lack of small particles with $r < r_{min}$. Relative to a size distribution that extends to $r = 0$, particles at or just larger than the cutoff experience fewer destructive collisions and are relatively overabundant (Campo Bagatin et al. 1994; O’Brien & Greenberg 2003). In turn, the higher frequency of these overabundant particles results in the destruction of more particles much larger than the cutoff, generating a minimum in $n(r)$. As these maxima and minima alternate among progressively larger particles, the amplitude of the waviness gradually decreases. For any Q_D^* , larger v_c results in a larger overabundance at the cutoff, which in turn creates larger waves among larger particles.

4.3. Physical Examples

In most applications, relations for Q_D^* and $v(r)$ are rarely single power-laws. Physically plausible expressions for Q_D^* consist of at least two power-laws (e.g., eq. 10) and may have an additional component that depends on the collision velocity (e.g., Benz & Asphaug 1999; Leinhardt & Stewart 2012). Throughout calculations of planet formation, the relative velocities of particles often depend on particle radius in a complicated way (e.g., Kenyon & Bromley 2015, 2017). During the late stages of planet formation, the relative velocities are often much simpler, with small particles having somewhat larger velocities than large particles (e.g., Goldreich et al. 2004; Kenyon & Bromley 2008, 2010, 2017). Here we consider how the equilibrium $n(r)$ reacts to the double power-law expression for Q_D^* with v independent of r .

To explore how the equilibrium $n(r)$ depends on the Q_D^* relation, we consider variations on the standard parameters. For these examples, we adopt $r_{max} = 100$ km and $v = 1$ –2 km s⁻¹; $Q_s \approx 10^3$ – 10^8 erg g⁻¹ cm^{-e_s},

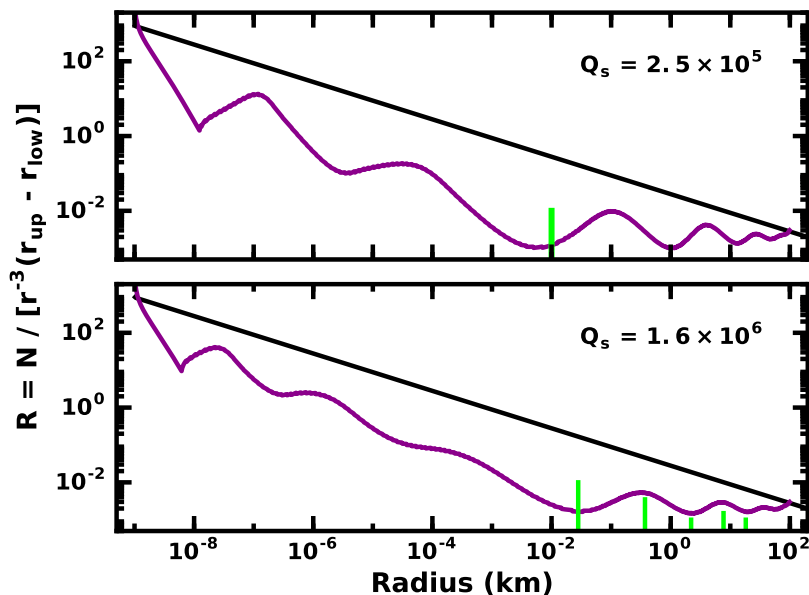


Fig. 3.— As in Fig. 2 for analytic models with $v = 1 \text{ km s}^{-1}$ and a physically plausible $Q_D^*(r)$ (eq. 10, $e_s = -0.4$, $Q_g = 0.3 \text{ erg g}^{-1}$, and $e_g = 1.35$). Compared to models with constant $Q_D = 8$ (black line in each panel), systems with a standard relation for Q_D^* have wavier size distributions (purple curves). Waviness increases as Q_s decreases. The long vertical green line in each panel shows the position of the transition radius. Shorter green lines in the lower panel indicate the predicted positions of peaks and valleys (e.g., Eqs. 21–22; O’Brien & Greenberg 2003).

$e_s \approx -0.5$ – 0.0 , $Q_g \approx 0.1$ – $3 \text{ erg g}^{-2} \text{ cm}^{3-e_g}$, and $e_g \approx 1.1$ – 1.5 (e.g., Asphaug & Benz 1996; Benz & Asphaug 1999; O’Brien & Greenberg 2003; Löhne et al. 2008; Wyatt 2008; Kenyon & Bromley 2008, 2010; Weidenschilling 2010a; Kenyon & Bromley 2012; Leinhardt & Stewart 2012, and references therein). We construct a large grid of equilibrium size distributions and examine how the shape depends on the collision velocity and the Q_D^* parameters.

Within our grid, the shape of $R(r)$ is most sensitive to Q_s (Fig. 3). In the lower panel, the wave from the small size cutoff at $1 \mu\text{m}$ is pronounced: there is a clear minimum in $R(r)$ at $6 \mu\text{m}$ followed by a maximum at $22 \mu\text{m}$. The next set of features – with a minimum at $300 \mu\text{m}$ and a maximum close to 1 mm – have a smaller amplitude and a longer wavelength. Although the third set – minimum close to 3 cm and a maximum at 30 cm – continues the progression of smaller amplitude and longer wavelength, the final set of features at 0.01 – 100 km has a larger amplitude and a shorter wavelength (in log space).

At the large sizes in Fig. 3, the minimum in Q_D^* at the transition radius r_t , $Q_t(r = r_t)$, generates the second set of waves in $n(r)$ (e.g., O’Brien & Greenberg 2003). Generally, the bulk strength is constant or decreases with radius ($e_s \leq 0$). The transition radius is then

$$r_t = \left(\frac{-e_s Q_s}{e_g \rho Q_g} \right)^{1/(e_g - e_s)}. \quad (20)$$

For particles with $r \approx r_t$, the minimum in Q_D^* produces a minimum (or ‘valley’) in $R(r)$ where particles are

easiest to break (O’Brien & Greenberg 2003). Particles with these sizes remove less material in collisions with larger particles, generating a local maximum (or ‘peak’) in $R(r)$. In their analytic derivation, O’Brien & Greenberg (2003) express the positions of the peaks r_p and valleys r_v in terms of Q_t , r_t , and v_c :

$$r_p = \left(\frac{2Q_t}{v^2} \right)^{-1/(e_g+3)} r_t^{e_g/(e_g+3)} r_v^{3/(e_g+3)}, \quad (21)$$

and

$$r_v = \left(\frac{2Q_t}{v^2} \right)^{-1/(e_g+3)} r_t^{e_g/(e_g+3)} r_p^{3/(e_g+3)}. \quad (22)$$

With a valley at $r_v = r_t$, the first relation establishes the first peak with $r > r_t$ at $r_{p,1} = (2Q_t/v^2)^{-1/(e_g+3)} r_t$. Eq. 22 then sets the first valley at $r_{v,1} = (2Q_t/v^2)^{-2/(e_g+3)} r_t^{5/(e_g+3)}$. Switching between Eqs. 21 and 22 yields a sequence of positions for peaks and valleys with $r > r_t$.

In the lower panel of Fig. 3, the long vertical green line at $r = 28$ m marks the transition radius for the adopted fragmentation parameters. The minimum at 33 m in the analytic $R(r)$ matches this prediction. Following this minimum, the analytic size distribution has a set of maxima (0.4 km, 7 km, and 35 km) that closely match the peaks at 0.4 km, 7.7 km, and 33 km predicted from Eq. 21. Valleys at 2.3 km, 19 km, and 53 km similarly lie close to the predictions of 2.2 km, 18 km, and 49 km. Comparisons of sequences for other analytic $R(r)$ with $Q_s \gtrsim 10^6$ erg g⁻¹ cm^{0.4} yield an excellent correspondence between the peaks and valleys in analytic size distributions with the predictions of Eqs. 21–22.

When $Q_s \lesssim 10^6$ erg g⁻¹ cm^{0.4}, the radius of the minimum in the analytic $R(r)$ is generally smaller than the transition radius r_t (Fig. 3, upper panel). The positions of peaks and valleys at $r > r_t$ also fall at smaller radii than predicted from Eqs. 21–22. When Q_s is small, the smaller Q_t results in a longer wavelength between peaks and valleys on either side of r_t (Eqs. 21–22). There is then an interference between the waves generated by the small-size cutoff and those caused by the minimum in Q_D^* . This interference displaces the waves from the predictions of the O’Brien & Greenberg (2003) model.

For some combinations of r_{min} and the Q_D^* parameters, the waves from r_{min} and r_t interfere destructively, yielding size distributions with slopes similar to those in Fig. 3 but with much smaller waves (Fig. 4). In this example, $Q_s = 2 \times 10^5$ erg g⁻¹ cm^{0.4}, $e_s = -0.4$, $Q_g = 0.3$ erg g⁻² cm^{1.65}, and $e_g = 1.35$. Setting $r_{min} = 0.1$ μm yields a steep slope and a large-amplitude wave from the small-size cutoff. After reaching a minimum at $r = 30$ m, $R(r)$ is fairly flat; waves from the transition in Q_D^* are obvious. Aside from a shift to larger sizes, setting $r_{min} = 0.5$ μm results in a nearly identical size distribution: the morphology of the waves is identical for small and larger sizes. Although choosing $r_{min} = 0.25$ μm makes little difference in $R(r)$ at $r \lesssim 30$ cm, the amplitude of waves at larger sizes is much smaller than for other r_{min} . In this example, the waves from the small-size cutoff nearly cancel those from the transition in Q_D^* at large r ; $R(r)$ is then nearly flat from $r = 1$ m to $r = 100$ km.

Understanding the origin of the vanishing waves with $r_{min} = 0.25$ μm is straightforward. For the adopted Q_D^* parameters in Fig. 4, the transition radius is $r_t = 8.4$ m (eq. 20) independent of r_{min} . When $r_{min} = 0.5$ μm (Fig. 4, orange curve), waves from the small-size cutoff produce a minimum (maximum) in $R(r)$ at 3–4 m (60–70 m). For $r_{min} = 0.1$ μm (Fig. 4, purple curve), these features occur at 10–100 cm. While the small-size cutoff clearly places minima on either side of r_t , maxima are well-displaced from r_t . Comparing the maxima at ~ 1 m (purple curve) and at 60–70 m (orange curve), it is clear that a model with some r_{min} between 0.1 μm and 0.5 μm will yield a maximum close to the transition radius at 8.4 m. Having a maximum from the small-size cutoff at the transition radius approximately ‘cancels’ the minimum produced from the transition radius, yielding a size distribution with little waviness for $r \gtrsim r_t$.

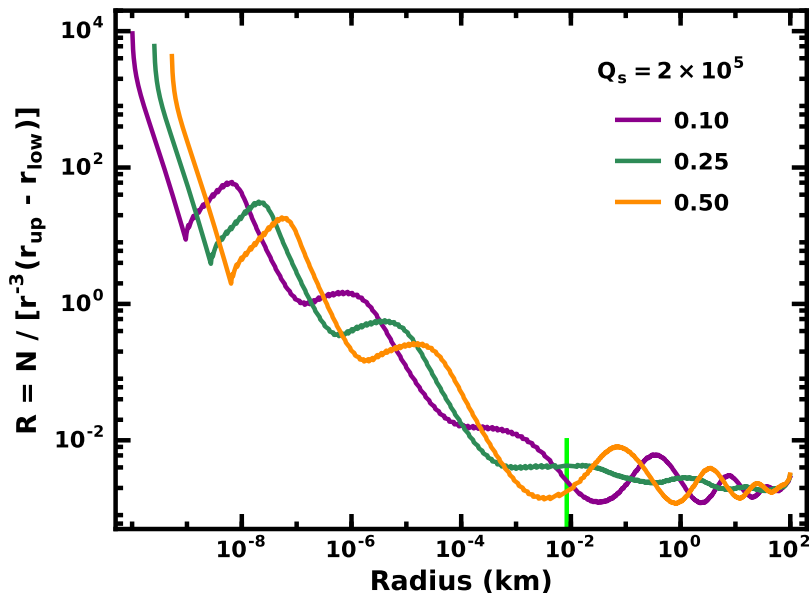


Fig. 4.— Comparison of $R(r)$ for analytic models with $Q_s = 2 \times 10^5 \text{ erg g}^{-1} \text{ cm}^{-0.4}$, $e_s = -0.4$, $Q_g = 0.3 \text{ erg g}^{-1}$, and $e_g = 1.35$ for various r_{min} (in microns) as listed in the legend. The vertical green line indicates the position of the transition radius, $r_t = 8.4 \text{ m}$. Despite the similarity in the size distributions at small sizes, interference between the small-size cutoff and the transition radius produce small waves when $r_{min} = 0.25 \text{ } \mu\text{m}$. For $r \gtrsim r_t$, different choices for r_{min} yield larger waves.

Fig. 5 illustrates how the morphology of the size distribution depends on v^2/Q_D^* . For fixed Q_D^* , raising v_c from 1 km s^{-1} to 1.4 km s^{-1} to 2 km s^{-1} increases the amplitude and wavelength of the waves. At small sizes, it is possible to scale the bulk component of the strength to compensate for the larger collision velocity and generate identical $R(r)$ from $0.1 \text{ } \mu\text{m}$ to r_t . In these examples, the transition radius moves from $r_t \approx 30 \text{ m}$ ($Q_s = 1.6 \times 10^6 \text{ erg g}^{-1} \text{ cm}^{0.4}$) to $r_t \approx 40 \text{ m}$ ($Q_s = 3.2 \times 10^6 \text{ erg g}^{-1} \text{ cm}^{0.4}$) to $r_t \approx 60 \text{ m}$ ($Q_s = 6.4 \times 10^6 \text{ erg g}^{-1} \text{ cm}^{0.4}$), shifting the peaks and valleys to larger r . With a smaller Q_t , models with the smaller v_c have the smaller wave amplitude and wavelength at $r \gtrsim r_t$. For the parameters in Fig. 5, however, the difference in amplitudes and wavelengths is less than 10%.

For the Q_D^* parameters we consider, the shape of the equilibrium size distribution is fairly insensitive to e_s and the gravity component of Q_D^* . Because the shape depends on the small size cutoff and the transition radius, it is usually possible to select a Q_s, e_s pair that yields a similar $R(r)$ to one with our ‘standard’ choice, $e_s = -0.4$, and a slightly different Q_s . When $r \gtrsim 1 \text{ km}$, the Benz & Asphaug (1999) choices for the gravity component, $Q_g = 2.1 \text{ erg g}^{-2} \text{ cm}^{1.81}$ and $e_g = 1.19$, yield similar binding energies as the Leinhardt & Stewart (2012) choices, $Q_g = 0.3 \text{ erg g}^{-2} \text{ cm}^{1.65}$ and $e_g = 1.35$. Near typical transition radii, $r_t \approx 0.01\text{--}0.1 \text{ km}$, the Leinhardt & Stewart (2012) parameters yield somewhat smaller Q_D^* than the Benz & Asphaug (1999) parameters and thus somewhat smaller r_t and Q_t . Although the shapes of size distributions using these two sets of parameters are then different for fixed bulk strength, the differences are small compared to the variations illustrated in Figs. 3–5.

Equilibrium $R(r)$ appropriate for TNOs are also insensitive to r_{max} . For $r_{min} = 1 \text{ } \mu\text{m}$ and $r_{max} =$

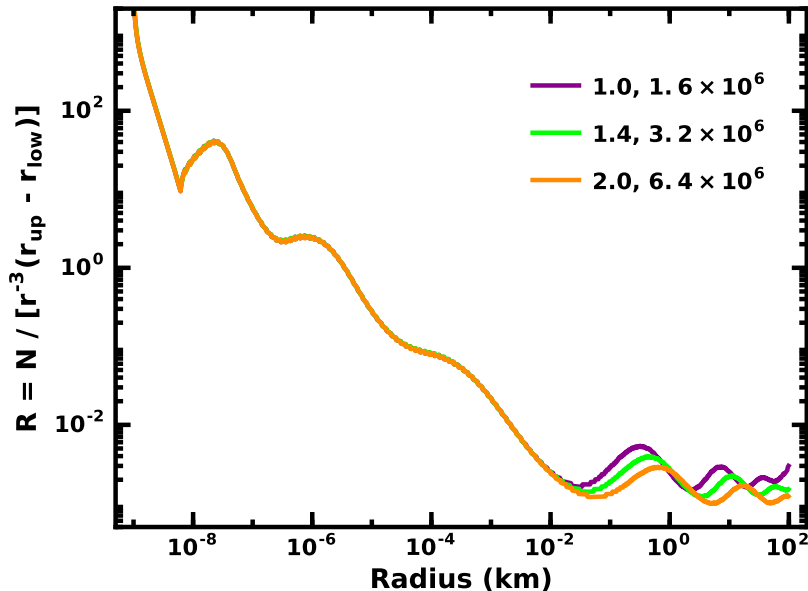


Fig. 5.— As in Fig. 4 for analytic models with $e_s = -0.4$, $Q_g = 0.3 \text{ erg g}^{-1}$, and $e_g = 1.35$ for various v_c and Q_s as listed in the legend. For small particles, it is possible to produce identical $R(r)$ with different v and Q_s . The displacements of the peaks and valleys in $R(r)$ grow at larger sizes.

50–200 km, the shape of the size distribution from 1 μm to 40–50 km is independent of r_{max} . For larger sizes, the shape and degree of waviness depend on the Q_D^* parameters and the collision velocity. However, the changes are relatively small compared to the magnitude of the waviness at $r \lesssim 30\text{--}50$ km and the variations as a function of v_c and the parameters for Q_D^* .

4.4. Application to TNOs

To apply the analytic model to observations of TNOs, we make a slight adjustment. Planetesimals with radii $r \leq r_b$ have the equilibrium size distribution; those with $r > r_b$ follow a power-law with index $q = 5\text{--}6$. With this modification, we include large TNOs whose size distribution is fixed over the lifetime of the Solar System.

Finding the best match to the *New Horizons* observations requires a search algorithm. We consider each model within the grid described in the previous section, where $v_c = 1\text{--}2 \text{ km s}^{-1}$, $r_{min} = 0.1\text{--}10 \mu\text{m}$, $Q_s = 10^3\text{--}10^8 \text{ erg g}^{-1} \text{ cm}^{-e_s}$, $e_s = -0.5\text{--}0.0$, $Q_g = 0.3 \text{ erg g}^{-2} \text{ cm}^{1.65}$, and $e_g = 1.35$. With little change in the shape of $R(r)$ as a function of r_{max} , we fix $r_b = 100$ km and derive equilibrium size distributions for $r < r_b$. For each set of parameters, we adjust a scale factor to derive the best match to the *New Horizons* data. Among the complete set of models, we search for those that minimize χ^2 using the quoted errors from Singer et al. (2019). The best models have a typical χ^2 per degree of freedom of 3–4. While these fits do not attain a χ^2 per degree of freedom of ~ 1 , the best fits are significantly better than the worst fits with χ^2 per degree of freedom $\gtrsim 100\text{--}1000$.

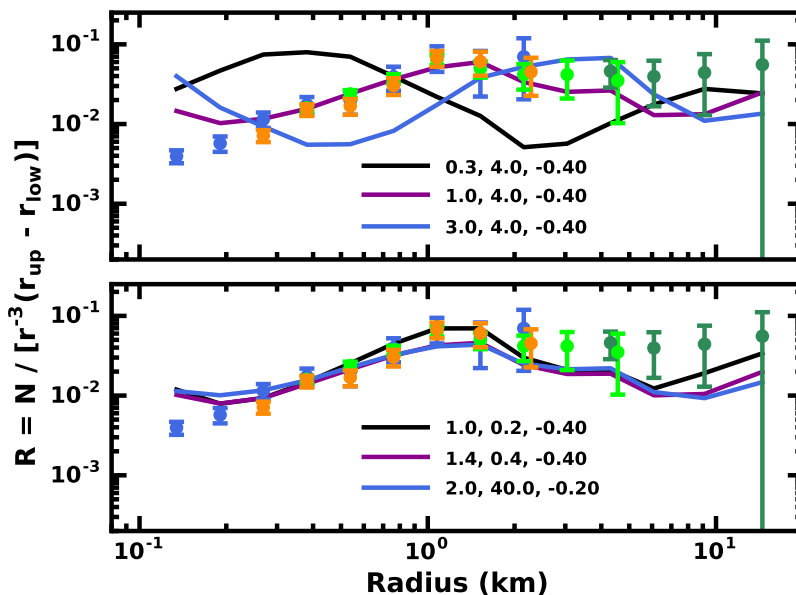


Fig. 6.— Comparison of the observed size distribution inferred from *New Horizons* cratering data (data color-coded as in Fig. 1, Singer et al. 2019) with equilibrium size distributions derived from an analytic model where Q_D^* is a function of radius. Some models have been adjusted vertically for clarity. For all models, $Q_g = 0.3 \text{ erg cm}^{1.65} \text{ g}^{-2}$ and $e_g = 1.35$. *Lower panel*: legend indicates numerical values for v_c in km s^{-1} , Q_s in units of $10^5 \text{ erg g}^{-1} \text{ cm}^{e_s}$, and e_s . *Upper panel*: for calculations with $v_c = 1.4 \text{ km s}^{-1}$, legend indicates numerical values for r_{min} in μm , Q_s in units of $10^4 \text{ erg g}^{-1} \text{ cm}^{0.4}$, and e_s .

Fig. 6 compares six equilibrium size distributions with the *New Horizons* data. In the lower panel, calculations with collision velocities, $v_c = 1$ (black curve) and 1.4 km s^{-1} (purple curve), and small values of Q_s yield size distributions that provide satisfactory matches to the data at 0.2–10 km. When the collision velocity is 2 km s^{-1} (blue curve), models with larger Q_s and smaller e_s match the data as well as those with smaller Q_s . Although higher velocity models match better at small sizes, they generate a somewhat larger valley at $r = 10\text{--}20 \text{ km}$ which may not be present in the data.

For all collision velocities considered in the lower panel of Fig. 6, we searched for reasonable matches with significantly different values of Q_s and e_s than those listed in the panel. When $v_c = 1\text{--}1.4 \text{ km s}^{-1}$, model size distributions with smaller Q_s have a minimum at 0.3–0.5 km and a steep rise to smaller sizes; at larger sizes, the waviness is larger than observed. Systems with factor of 100 larger Q_s have a fairly flat $R(r)$ with negligible waves compared to the *New Horizons* data. When $v_c = 2 \text{ km s}^{-1}$, size distributions with small Q_s rarely have a minimum at 0.1 km and are too wavy to match the *New Horizons* data. Strong ice particles have equilibrium size distributions that are not wavy enough to match the *New Horizons* data.

Varying r_{min} from the standard $1 \mu\text{m}$ does not allow better matches to the data (Fig. 6, upper panel). For a broad range of Q_s and e_s , reducing r_{min} to 0.1–0.3 μm eliminates the drop in $R(r)$ from 0.5–0.6 km to 0.1 km. Similarly, increasing r_{min} to 3–10 μm also makes it harder to match the data at the smallest sizes.

The amplitude and position of the wave at $r = 0.1\text{--}1 \text{ km}$ are sensitive to Q_s and e_s . In any model, 10%

changes to Q_s and 5% changes to e_s have a small impact on the wave. Larger modifications either make the amplitude of the wave smaller or shift it to smaller or larger r . For collision velocities $v_c = 1\text{--}2 \text{ km s}^{-1}$ and the range of Q_D^* parameters we studied, making the wave amplitude or wavelength larger is impossible. Models with smaller and larger values for v_c also tend to provide poorer matches to the data.

Adopting velocity laws with shallow power-laws, $v \propto r^{e_v}$ with $e_v < 0.01\text{--}0.02$, changes these results insignificantly. In our experiments, larger variations in collision velocity from the smallest to the largest objects in the grid generate much poorer matches to the *New Horizons* data. While it may be possible to identify $v(r)$ relations that allow better matches to the *New Horizons* data (e.g., the possibilities discussed in Pan & Schlichting 2012), our analysis suggests a constant velocity among TNOs provides a better match to the *New Horizons* observations.

Given the uncertainties in and the simplicity of the analytic model, it provides a reasonable match to the *New Horizons* data. Compared to standard collisional disruption models where the slope for $r \lesssim 100 \text{ km}$ is 3.5, the match to the *New Horizons* data at 0.1–10 km with the analytic equilibrium model is impressive (compare with Fig. 1). Despite this success, the analytic model does not include cratering collisions which remove less than half the mass from the target. In most numerical simulations, cratering enables significant mass loss from the system and sometimes competes with catastrophic collisions in generating the collisional cascade. With no analytic model for cratering, we rely on numerical simulations to consider whether including cratering in a collision algorithm can maintain the reasonable match between the analytic model and the *New Horizons* data.

5. COLLISIONAL CASCADES: NUMERICAL RESULTS

5.1. Methods

To calculate the evolution of KBOs with different sizes, we run a series of numerical simulations with *Orchestra*, an ensemble of computer codes designed to track the accretion, fragmentation, and orbital evolution of solid particles ranging in size from a few microns to thousands of km (Kenyon 2002; Bromley & Kenyon 2006; Kenyon & Bromley 2008; Bromley & Kenyon 2011, 2013; Kenyon & Bromley 2016; Kenyon et al. 2016). Using the coagulation component of *Orchestra*, we start with an ensemble of solids with minimum radius r_{min} and maximum radius r_{max} orbiting the Sun within a single annulus having an inner radius a_{in} and outer radius a_{out} . The solids have mass density ρ , initial total mass M_0 , and initial surface density Σ_0 .

To evolve the size and velocity distributions of solids in time, *Orchestra* derives collision rates and outcomes with standard particle-in-a-box algorithms. Systems start with an initial size distribution $n(r) \propto r^{-q}$ in discrete bins with a mass spacing factor $\delta = m_{i+1}/m_i$ between adjacent bins. When a pair of solids collide, the mass of the merged object is

$$m = m_1 + m_2 - m_{esc} . \quad (23)$$

The mass of debris ejected in a collision is

$$m_{esc} = 0.5 (m_1 + m_2) \left(\frac{Q_c}{Q_D^*} \right)^{b_d} . \quad (24)$$

The exponent b_d is a constant of order unity (e.g., Davis et al. 1985; Wetherill & Stewart 1993; Kenyon

& Luu 1999a; Benz & Asphaug 1999; O’Brien & Greenberg 2003; Kobayashi & Tanaka 2010; Leinhardt & Stewart 2012).

To place the debris in the grid of mass bins, we set the mass of the largest collision fragment as

$$m_{max,d} = m_{l,0} \left(\frac{Q_c}{Q_D^*} \right)^{-b_l} m_{esc}, \quad (25)$$

where $m_{l,0} \approx 0.01$ – 0.5 and $b_l \approx 0$ – 1.25 (Wetherill & Stewart 1993; Kenyon & Bromley 2008; Kobayashi & Tanaka 2010; Weidenschilling 2010b). When b_l is large, catastrophic (cratering) collisions with $Q_c \gtrsim Q_D^*$ ($Q_c \lesssim Q_D^*$) crush solids into smaller fragments. Lower mass objects have a differential size distribution $N(r) \propto r^{-q_d}$. After placing a single object with mass $m_{max,d}$ in an appropriate bin, we place material in successively smaller mass bins until (i) the mass is exhausted or (ii) mass is placed in the smallest mass bin. Any material left over is removed from the grid.

In most calculations, we assume that the orbital e and i are constant with time. Otherwise, we derive orbital evolution due to collisional damping from inelastic collisions and gravitational interactions. For inelastic and elastic collisions, we follow the statistical, Fokker-Planck approaches of Ohtsuki (1992) and Ohtsuki et al. (2002), which treat pairwise interactions (e.g., dynamical friction and viscous stirring) between all objects. We also compute long-range stirring from distant oligarchs (Weidenschilling 1989).

Our solutions to the evolution equations conserve mass and energy to machine accuracy. Typical calculations require several 12 hr runs on a system with 56 cpus; over the 10^6 – 10^8 timesteps in a typical 2–4 Gyr run, calculations conserve mass and energy to better than one part in 10^{10} .

Although nearly all other numerical treatments of KBO evolution adopt a variant of the particle-in-a-box algorithm for collision rates (e.g., Benavidez & Campo Bagatin 2009; Fraser 2009; Schlichting & Sari 2011; Campo Bagatin & Benavidez 2012; Schlichting et al. 2013, and references therein), the details of deriving collision outcomes often differ from one investigation to the next. To make clear connections with previous calculations, we first consider a set of calculations with standard starting conditions. This analysis also allows us to understand the relationships between the features in the size distributions and the initial conditions and various input parameters. We then examine how to build a numerical cascade model that generates the size distribution derived from Charon impactors with *New Horizons*.

5.2. Evolution of the Size Distribution for Standard Parameters

In models 1–4 (Table 1), we explore parameter spaces considered in previous publications (O’Brien & Greenberg 2003; Kenyon & Bromley 2008; Fraser 2009; Benavidez & Campo Bagatin 2009; Kenyon & Bromley 2010, 2012; Campo Bagatin & Benavidez 2012; Schlichting et al. 2013). In a single annulus at 30–60 au that spans the Kuiper belt, the large initial mass ($45 M_\oplus$) guarantees evolution towards an equilibrium size distribution in 0.5–1 Gyr. The choice for the mass resolution, $\delta = 1.12$, should yield smooth size distributions with relatively little noise (e.g., Kenyon & Bromley 2016). For a system with an initial $r_{max} = 500$ km and collision velocity $v_c = 1$ km s $^{-1}$, we choose four sets of fragmentation parameters that result in destructive collisions for objects with mass density $\rho = 1.5$ g cm $^{-3}$ and $1 \mu\text{m} \lesssim r \lesssim 100$ – 200 km. The initial size distribution has a steep slope, $q = 5.5$, for $r \geq r_l$ with $r_l =$ (a) 1 km, (b) 3 km, (c) 10 km, (d) 30 km, or (e) 100 km. In all calculations, $r_l = r_s$; there is no intermediate size population between the steep power-law at large sizes ($r \gtrsim r_l$) and the shallower power-laws at small sizes ($r \lesssim r_s$). At smaller sizes, we consider initial slopes with integer values between -3 and 3 inclusive. Most of the initial mass is concentrated in size

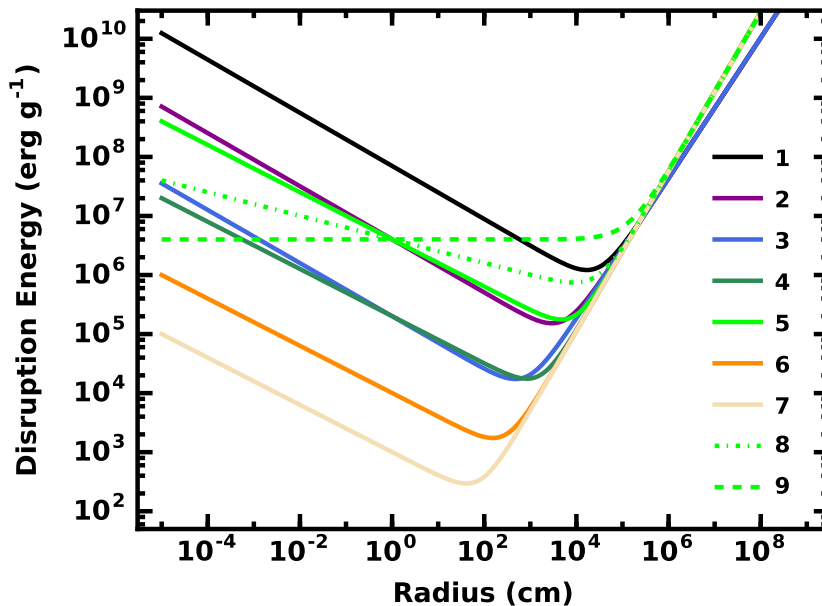


Fig. 7.— Variation of Q_D^* as a function of radius for the fragmentation models summarized in Table 1. For $r \gtrsim 1$ km, the Benz & Asphaug (1999) and Leinhardt & Stewart (2012) parameters yield similar results for Q_D^* . At smaller radii, the minimum in Q_D^* at r_t depends on Q_s and e_s . In the examples shown, $r_t \approx 1$ –100 m.

bins with $r \approx r_l$; destructive collisions initiate a robust cascade for $r \leq 100$ km. Although growth is possible for $r \gtrsim 200$ km, the large collision velocity and small mass guarantees modest evolution in the population of the largest objects over 1–5 Gyr.

The sets of fragmentation parameters in the first four rows of Table 1 span the range of possibilities derived from numerical simulations of high velocity collisions between solids with an icy composition. In the ‘strong ice’ formulation of Benz & Asphaug (1999) for model (1), the binding energy in the strength and gravity regimes is comparable with basalt (Fig. 7, black line). The ‘weak ice’ parameters derived by Leinhardt & Stewart (2012) for model (4) yield similar results in the gravity regime ($r \gtrsim 1$ km), but the binding energy of 1 cm objects is 350 times smaller (Fig. 7, dark green line). The ‘normal ice’ regime of model (2) adopted in Schlichting et al. (2013) follows the gravity regime of Benz & Asphaug (1999) and places the binding energy of 1 cm objects in between the strong and weak ice models (Fig. 7, purple line). Model (3) is a composite of the Benz & Asphaug (1999) and Leinhardt & Stewart (2012) approaches (Fig. 7, blue line), setting the gravity component as in model (1) and the strength component as in model (4).

Before considering the results of the numerical calculations, we place the starting conditions in the context of analytic models for collisional cascades (e.g. Wyatt & Dent 2002; Dominik & Decin 2003; Wyatt 2008; Wyatt et al. 2011; Kenyon & Bromley 2017, and references therein). For the initial mass $M_0 = 45 M_\oplus$ at 45 au, the time scale for collisions between equal-mass objects is

$$t_0 \approx 8 \text{ Myr} \left(\frac{r_l}{1 \text{ km}} \right) \left(\frac{45 M_\oplus}{M_0} \right). \quad (26)$$

Systems with $r_l = 1$ km evolve on short time scales, allowing the system to reach an approximate equilibrium

over the 4.5 Gyr age of the Solar System. Other initial conditions, such as q_s , probably have little impact on the equilibrium. With 100 times longer collision times, systems with most of the mass in 100 km objects cannot evolve into an equilibrium. After 4.5 Gyr, their size distributions probably depend on q_s .

Aside from t_0 , the evolution of the mass in a collisional cascade depends on the ratio of the collision velocity to Q_D^* . When v^2/Q_D^* is large, collisions between unequal mass objects produce much more debris than when v^2/Q_D^* is small. The mass in the system then declines much more rapidly. In our approach, the time scale for the mass to decline is $\tau_0 \approx 1.13\alpha t_0$ (Kenyon & Bromley 2017) where α is a function of v^2/Q_D^* . When $v^2/Q_D^* \approx 5$ –10, $\alpha \approx 5$. Equal-mass collisions barely shatter the objects; the time scale to reduce the system mass by a factor of two is roughly five times larger than t_0 . When $v^2/Q_D^* \approx 1000$ –3000, $\alpha \approx 0.1$ –0.04. Equal-mass collisions completely shatter the objects and leave behind low mass remnants; the time scale for mass reduction is 10–20 times faster than t_0 .

Table 2 lists v^2/Q_D^* and τ_0 for the parameters in models 1–4. Ensembles of 1 km objects colliding at 1 km s^{-1} have large $v^2/Q_D^* \approx 3000$ and short evolution time scales, $\tau_0 \approx 0.3$ –0.4 Myr. With the system mass, $M \propto M_0/(1 + t/\tau_0)^{1.13}$, these systems lose most of their initial mass on time scales of 100 Myr. Significant mass loss allows the system to approach an equilibrium state. In contrast, the small v^2/Q_D^* and large τ_0 for a ring of 100 km objects implies little evolution on interesting time scales. Over 4.5 Gyr, these systems retain 40% to 75% of their initial mass and have little time to reach equilibrium. For the largest objects in the swarm ($r \gtrsim 100 \text{ km}$), their size distributions will change little.

In the next sub-sections, we review the evolution of calculations with the parameters of models 1–4. Because the evolution is repetitive, we discuss model (1) in detail, summarizing how the size distribution changes in time as a function of the starting conditions and comparing how $R(r)$ at 4.5 Gyr depend on r_l and q_s . For models (2)–(4), we illustrate differences between the results of these calculations and those of model (1), concentrating on (i) whether $R(r)$ reaches an equilibrium and (ii) how these equilibria depend on initial conditions.

5.2.1. Calculations with Strong Ice

Fig. 8 illustrates the evolution of $R(r)$ for a system with $r_l = 1 \text{ km}$, $q_s = -3$, and strong ice Benz & Asphaug (1999). Starting from a very peaked size distribution at $t = 0$, the cascade gradually removes km-sized objects and generates a pronounced debris tail at $r \lesssim 0.1 \text{ km}$. After 1–3 Myr (Fig. 8, lower panel), the debris tail contains as much mass as all objects with $r \gtrsim 3 \text{ km}$. With a few low amplitude waves at $r \lesssim 1 \text{ cm}$ (not shown) and an overall slope $q \approx 3.70$, the shape of $R(r)$ for $1 \mu\text{m} \lesssim r \lesssim 0.1 \text{ km}$ follows the general expectation for a collisional cascade.

As the calculation proceeds (Fig. 8, top panel), catastrophic collisions gradually eliminate most of the material at 1 km and shift the peak to larger and larger sizes. At the same time, cratering collisions continually erode the population of 10–100 km objects. Over 4.5 Gyr, the system loses 98.7% of its initial mass. The remaining material has a steep size distribution at $r \gtrsim 30 \text{ km}$ with a slope similar to the initial $q_l = 5.5$, which flattens out at $r \approx 0.1$ –10 km and then rises at much smaller radii with a slope $q \approx 3.7$.

In this calculation, the amount of mass in the two ‘peaks’ at 1–5 km and at 5–30 km depends on the evolution time. With more mass initially in km-sized objects, the time scale for the cascade to destroy half of these objects is $t_0 \approx 8 \text{ Myr}$ (Eq. 26). After many destructive collisions over the first 1–10 Myr, cratering by small particles in the debris tail accelerates the loss of km-sized objects. Over the next 40 Myr, this

Table 1. Input Parameters for Coagulation Calculations^a

Model	v (km s ⁻¹)	b_d	$m_{l,0}$	b_l	Q_s	e_s	Q_g	e_g	r_t (km)	Q_t (erg g ⁻¹)
1	1.0	1.0	0.2	0.0	7×10^7	-0.45	2.10	1.19	0.1668	1.23×10^6
2	1.0	1.0	0.2	0.0	4×10^6	-0.45	2.10	1.19	0.0291	1.54×10^5
3	1.0	1.0	0.2	0.0	2×10^5	-0.45	2.10	1.19	0.0047	1.76×10^4
4	1.0	1.0	0.2	0.0	2×10^5	-0.40	0.30	1.35	0.0084	1.78×10^4
5	1.0	1.0	0.2	0.0	4×10^6	-0.40	0.30	1.35	0.0467	1.79×10^5
6	1.0	1.0	0.2	0.0	1×10^4	-0.40	0.30	1.35	0.0015	1.76×10^3
7	1.0	1.0	0.2	0.0	1×10^3	-0.40	0.30	1.35	0.0004	2.99×10^2
8	1.0	1.0	0.2	0.0	4×10^6	-0.20	0.30	1.35	0.0887	7.51×10^5
9	1.0	1.0	0.2	0.0	4×10^6	-0.00	0.30	1.35	...	4.00×10^6
10	1.4	1.0	0.2	0.0	4×10^6	-0.40	0.30	1.35	0.0467	1.79×10^5
11	2.0	1.0	0.2	0.0	4×10^6	-0.40	0.30	1.35	0.0467	1.79×10^5

^aThe columns list v the collision velocity; b_d the exponent in the relation between ejected mass and impact energy (Eq. 24); $m_{l,0}$ and b_l , parameters in the relation between the size of the large remnant and the impact energy (Eq. 25); Q_s , e_s , Q_g , and e_g , the parameters in the relation for Q_D^* (Eq. 10); r_t , the transition radius where Q_D^* is a minimum (Eq. 20; and Q_t , the minimum Q_D^* at r_t . All calculations are performed in an annulus with inner radius $a_{in} = 30$ au, outer radius $a_{out} = 60$ au, and total mass $M_0 = 45 M_\oplus$. Particles have minimum sizes $r_{min} = 1 \mu\text{m}$, initial maximum sizes $r_{max} = 500$ km, and mass density $\rho = 1.5 \text{ g cm}^{-3}$. collide at velocity $v = 1 \text{ km s}^{-1}$. The initial size distribution is a power-law with slope $q_l = 5.5$ for radii $r \gtrsim r_l$ and slope q_s for $r \lesssim r_s$. The mass grid has $\delta = 1.12$. In these calculations, $r_s = r_l$, with $r_l = 1, 3, 10, 30, \text{ or } 100$ km; $q_s = -3$ to 3 inclusive.

Table 2. Collision Time Scales^a

Model	$r_l = 1 \text{ km}$		$r_l = 3 \text{ km}$		$r_l = 10 \text{ km}$		$r_l = 30 \text{ km}$		$r_l = 100 \text{ km}$	
	v^2/Q_D^*	τ_0 (Myr)	v^2/Q_D^*	τ_0 (Myr)	v^2/Q_D^*	τ_0 (Myr)	v^2/Q_D^*	τ_0 (Myr)	v^2/Q_D^*	τ_0 (Myr)
1	2468.7	0.4	720.6	3.2	174.3	33.5	47.2	296.4	11.3	3352.9
2	2690.9	0.4	731.3	3.1	174.7	33.5	47.3	296.3	11.3	3352.8
3	2705.0	0.4	732.0	3.1	174.7	33.5	47.3	296.3	11.3	3352.8
4	2891.3	0.3	656.4	3.4	129.2	42.9	29.3	443.0	5.8	6049.1
5	2862.6	0.3	655.5	3.4	129.2	42.9	29.3	443.0	5.8	6049.2
6	2892.8	0.3	656.5	3.4	129.2	42.9	29.3	443.0	5.8	6049.1
7	2892.8	0.3	656.5	3.4	129.2	42.9	29.3	443.0	5.8	6049.1
8	2605.0	0.4	643.5	3.5	128.8	43.0	29.3	443.2	5.8	6049.6
9	1341.1	0.6	519.9	4.1	122.9	44.7	29.0	447.4	5.8	6061.6
10	5610.8	0.2	1284.7	2.0	253.2	24.7	57.5	251.6	11.3	3344.0
11	11450.5	0.1	2621.8	1.1	516.8	13.8	117.3	139.3	23.1	1809.2

^aThe columns list $v^2/Q_D^* = v^2/Q_D^*$ for collisions between equal mass objects with the listed radius, $v = 1 \text{ km s}^{-1}$, and parameters for Q_D^* in Table 1; and the evolution time for a collisional cascade with an equilibrium size distribution, $\tau_0 = 1.13\alpha t_0$, where t_0 is defined in Eq. 14 and $\alpha = 13.0(v^2/qdstar)^{-1.237} + 20.9(v_c^2/Q_D^*)^{-0.793}$ (Kenyon & Bromley 2017).

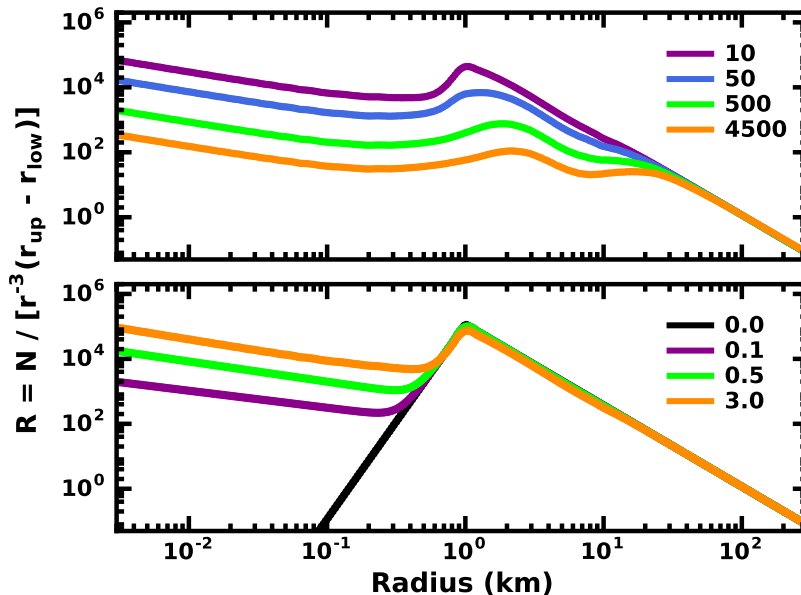


Fig. 8.— Evolution of $R(r)$ for a collisional cascade with initial mass $M_0 = 45 M_\oplus$, initial size distribution parameters $r_s = r_l = 1$ km, $q_l = 5.5$, and $q_s = -3.0$, and fragmentation parameters $Q_b = 7 \times 10^7$ erg g $^{-1}$ cm $^{0.45}$, $e_b = -0.45$, $Q_g = 2.1$ erg g $^{-2}$ cm $^{1.81}$, and $e_g = 1.19$. Evolution times in Myr are listed in each panel. *Lower panel:* Collisions generate a fragmentation tail for $r < 1$ km. Although the amount of material in the tail grows with time, the size distribution for $r \gtrsim 1$ km is unchanged for the first 3 Myr of evolution. *Upper panel:* As the evolution proceeds, collisions deplete material from the peak of the size distribution at 1 km; the peak gradually moves to larger radii.

population drops by a factor of seven, turning a very peaked $R(r)$ with a maximum at 1 km into a rounded size distribution with a peak close to 1 km. As the cascade proceeds, the typical collision time grows due to the falling surface density and the concentration of mass into larger and larger objects. By the end of the calculation at 4.5 Gyr, the surface density is 100 times smaller; 10–20 km objects contain most of the remaining mass. With t_0 now ~ 1 Gyr, the peak in $R(r)$ will continue to drop by a factor of two in number every 1–2 Gyr.

Among objects with $r \gtrsim 5$ km, collision outcomes depend on the relative masses of the projectiles and the targets. For projectiles at the peak of the size distribution ($r \approx 1$ –2 km), collisions with 5 km objects are catastrophic. However, cratering events with much less numerous 10 km objects produce debris and leave behind a slightly smaller remnant. Thus, 5 km objects are removed from the swarm more rapidly than 10–20 km objects, creating a pronounced dip in $R(r)$ after 4.5 Gyr of evolution. Continuing the calculation beyond 4.5 Gyr would continue the evolution visible in the top panel of Fig. 8: the peak at 2–3 km would gradually shift to larger radii, possibly eliminating the dip at 5 km and generating a fairly flat $R(r)$ at 1–30 km. At the same time, the shoulder in $R(r)$ at 20–30 km would gradually shift to larger radii. Throughout this evolution, the fragmentation tail at $r \lesssim 0.1$ –0.3 km would have some modest waves superimposed on a constant slope $q \approx 3.7$.

Starting with a different size distribution for the smaller objects leads to similar results (Fig. 9). When

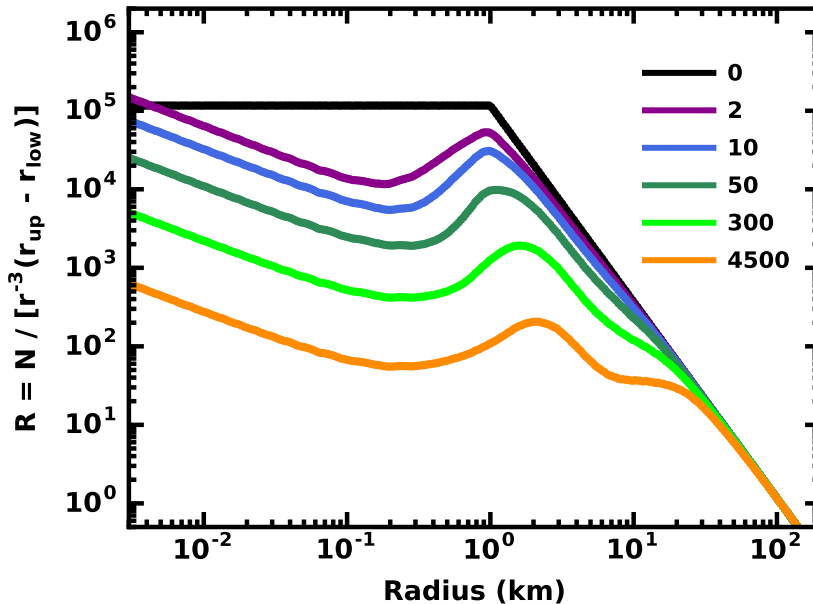


Fig. 9.— As in Fig. 8 for $q_s = 3.0$. Collisional depletion of 1 km objects generates a pronounced wave in the size distribution, with a valley near the transition radius, $r_t = 0.17$ km, a peak at 1–2 km, and a second valley at 5–10 km. Although the valley at the r_t remains fixed, peaks and valleys at larger radii gradually move to larger radii with time.

$q_s = 3$, objects with $r \lesssim 1$ km contain a modest amount of the total mass. Unlike a calculation with $q_s = -3$, this extra material rapidly destroys 1 km objects through numerous cratering collisions. With $r_t \approx 0.15$ km, catastrophic and cratering collisions also remove objects rapidly from bins with $r \approx 0.1$ – 0.2 km. In ~ 10 Myr, the number of 1 km (0.1–0.2 km) objects drops by a factor of seven (thirty), dramatically changing $R(r)$ at 0.01–1 km.

In the first 10–50 Myr of this calculation, cratering also removes substantial mass from particles as large as 10 km. Although collisions among 10–20 km objects are rare, these objects are continually peppered by much smaller objects. As a result of this cratering, the slope of the size distribution slowly declines from the original steep slope $q = 5.5$ to $q \approx 4.6$. Material from these collisions flows into the debris tail, which robustly maintains the standard slope, $q \approx 3.7$, from 1–10 μm to 0.01 km.

After 300 Myr, the size distribution in this calculation starts to resemble the calculation in Fig. 8 (Fig. 9, light green curve). While the evolution produces a minimum in $R(r)$ at 0.1–0.3 km, the peak slowly shifts from 1 km to 2–3 km. As this peak shifts to larger sizes, catastrophic collisions generate a dip in the size distribution at 5 km. For larger particles, $R(r)$ consists of a fairly flat (10–30 km) section that merges with the steep $q = 5.5$ section at the largest sizes. After 4.5 Gyr, this system loses 99.1% of its initial mass, slightly more than systems with smaller q_s .

Despite starting with differing amounts of material with $r \lesssim 1$ km, all calculations with $r_l = 1$ km and $q_s = -3$ to 3 approach nearly identical size distributions after 4.5 Gyr of collisional evolution (Fig. 10). Starting at the smallest sizes we consider (1 μm), all $n(r)$ follow a power law with $q \approx 3.7$ for $r \lesssim 0.05$ – 0.1 km. Among

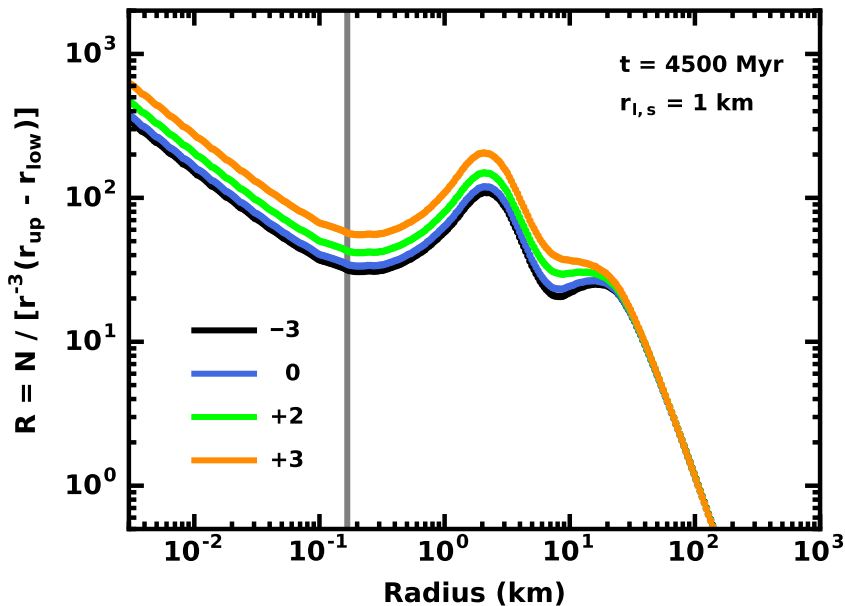


Fig. 10.— Size distribution at 4.5 Gyr for collisional cascades with initial mass $M_0 = 45 M_\oplus$, initial size distribution parameters $r_s = r_l = 1$ km and $q_l = 5.5$, and fragmentation parameters $Q_b = 7 \times 10^7$ erg g $^{-1}$ cm $^{0.45}$, $e_b = -0.45$, $Q_g = 2.1$ erg g $^{-2}$ cm $^{1.81}$, and $e_g = 1.19$ for various slopes q_s of the initial size distribution as listed in the legend. The vertical grey line indicates the transition radius for this set of Q_D^* parameters. The shapes of $R(r)$ are nearly independent of q_s .

the smallest particles with $r = 1\text{--}10$ μm , the ratio $v^2/Q_D^* \approx 10$. Thus the degree of waviness is negligible at the smallest sizes (see Fig. 2). The first major wave occurs near the transition radius, $r_t \approx 0.17$ km, where particles are weakest. After this minimum, the shape of the first peak at 2–3 km is insensitive to q_s : normalizing the four curves in Fig. 10 at the same R value at 2–3 km yields nearly indistinguishable $R(r)$ for smaller sizes.

For larger particles, the shape of $R(r)$ at 4.5 Gyr depends on q_s . Systems with $q_s \approx -3$ have a deeper valley at 5 km than those with $q_s \approx 3$. Because the valley is deeper, the local peak at 10–20 km is more pronounced in systems with $q_s \approx -3$ than those with $q_s \approx 3$. Over 4.5 Gyr, cratering produces this difference. Systems with $q_s \approx 3$ initially have more mass in objects with $r \lesssim 1$ km than those with $q_s \approx -3$. With this extra mass, substantial cratering begins at the start of the calculation. Over time, this cratering removes slightly more mass at 5–20 km compared to calculations with $q_s \approx -3$. At 5–20 km, $R(r)$ has a smaller valley at 5 km and a less obvious peak at 10–20 km.

The final states of these calculations agree with several expectations for equilibrium size distributions. For all q_s , $R(r)$ has a valley near the transition radius, $r_t = 0.17$ km. From Eqs. 21–22, equilibrium models have an expected peak at 1.2 km and a valley at 5.1 km. Results from the numerical calculations yield $r_p \approx 2$ km and $r_v \approx 8$ km. In these numerical results, the shifts are not from waves emanating from the small-size cutoff. The waves at small sizes are too small to impact $R(r)$ at larger sizes. Instead, several aspects of the calculation shift the waves to somewhat larger sizes: (i) after 4.5 Gyr, the system has not quite reached equilibrium, (ii) our use of the full expression for Q_D^* instead of two separate power laws displaces peaks and

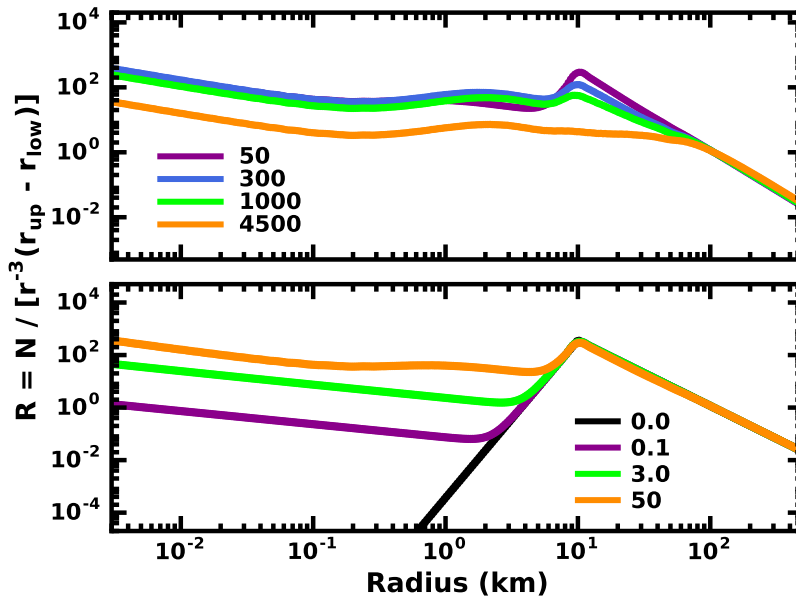


Fig. 11.— As in Fig. 8 for $r_l = r_s = 10$ km; evolution times in Myr appear in the legend for each panel. Although the collision time is ten times longer than for systems with $r_l = 1$ km, the shape of the size distribution evolves in a similar fashion. After 4.5 Gyr, $R(r)$ develops a clear minimum near the transition radius, $r_t = 0.17$ km, a modest peak (valley) at 2 km (5–6 km), a small peak at 10 km, a gradual decline to 100 km, and a steep drop to 500 km.

valleys (O’Brien & Greenberg 2003), and (iii) our starting condition with a steep slope $q = 5.5$ at the largest sizes creates an inflection point in $n(r)$ which impacts the amount of debris lost in cratering collisions. Fig. 10 demonstrates that the depth of the valley at 8 km also depends on the initial slope of the size distribution at $r \lesssim 1$ km. More material initially at smaller sizes leads to a shallower valley. Together, these features of the calculation shift peaks and valleys from analytic expectations.

Among previously published calculations, only Fraser (2009) considers a starting point with most of the mass in small objects with $r \approx 1$ km and the Benz & Asphaug (1999) fragmentation parameters. The evolution in Figs. 8–10 generally agrees with these results. Using identical fragmentation parameters, Fraser (2009) derives size distributions with a valley near r_t , a peak at 2–3 km, and a valley (‘divot’) at 10 km. This shape is fairly insensitive to small changes in the fragmentation parameters.

Aside from the longer evolution time, placing most of the initial mass in larger objects has a modest impact on $R(r)$ at 4.5 Gyr. When $r_l = 10$ km, the collision time at the start of each calculation is roughly ten times longer than when $r_l = 1$ km (Eq. 26). During the first 50 Myr in the evolution of a calculation with $q_s = -3$ (Fig. 11, lower panel), catastrophic collisions of 10 km objects build a prominent debris tail. The deep valley in $R(r)$ advances from 2 km at 0.1 Myr to 6 km at 50 Myr. Early on in this sequence, the debris tail has a small wave at 1–10 μm superimposed on a smooth distribution with slope $q \approx 3.7$. By 50 Myr, $R(r)$ flattens at 0.1–3 km and develops a second small wave. At larger sizes ($r \gtrsim 10$ km), $R(r)$ is essentially constant in time.

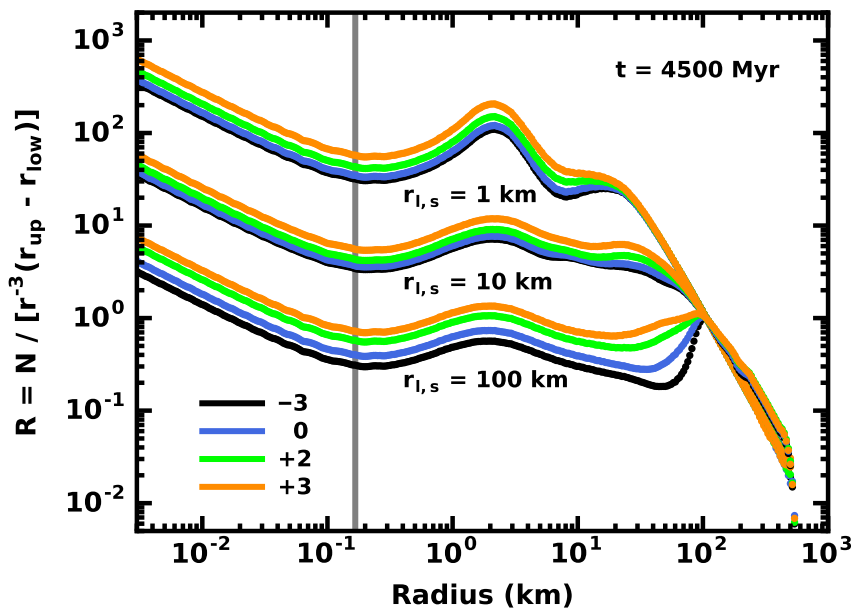


Fig. 12.— Size distributions at 4.5 Gyr for strong ice calculations with various $r_{l,s} = 1, 10,$ and 100 km as indicated under each set of curves and various q_s as indicated in the legend in the lower left corner. The vertical grey line indicates the transition radius for this set of Q_D^* parameters. Common features of $R(r)$ include (i) an extended debris tail with slope $q = 3.7$ at $r \lesssim 0.1$ km, (ii) a valley near the transition radius $r_t = 0.17$ km, and (iii) a peak at $r \approx 2$ km. The height of the 2 km peaks depends on r_l but not q_s . Features in $R(r)$ for $r \gtrsim 5$ km – including a valley at 5–10 km and peaks at 20–100 km – also depend on r_l . The slope q_s is only important for calculations with $r_l = 100$ km, where systems with small q_s have a much deeper valley at 40–50 km than those with larger q_s .

From 50 Myr to 4.5 Gyr, catastrophic collisions and cratering remove 91% of the initial mass and modify $R(r)$ considerably at 0.1–100 km (Fig. 11, top panel). For $r \lesssim 0.1$ km, the system maintains a fairly smooth debris tail with $q \approx 3.7$ and a small wave at 1–10 μm . As catastrophic collisions remove the sharp peak at 10 km, they establish a distinct valley in the debris tail near the transition radius, $r_t = 0.17$ km. A wave in $R(r)$ at larger sizes has a modest peak at 2 km and a valley at 6 km. Beyond a tiny residual peak at 10 km, $n(r)$ has a slope $q \approx 3.7$ – 3.8 at 10–100 km; at 100–500 km, $q \approx 5.4$.

The features in $R(r)$ have several physical sources. At 10 km, catastrophic collisions are numerous enough to destroy most of the objects after 1–2 Gyr. As with the calculations of Figs. 8–10, catastrophic collisions and cratering combine to create the wavy size distribution with valleys at 0.17 km and 6 km and a peak at 2 km. The second valley lies closer to the analytic prediction of 5.1 km, but the peak is still off the prediction of 1.2 km. Among the largest objects with $r \approx 100$ –500 km and initial $q = 5.5$, collisions between equal mass objects are extremely rare. Cratering dominates. Because cratering can remove material more easily from 100 km objects than 500 km objects, the population of 100 km objects decreases slightly, enough to decrease the slope from $q = 5.5$ to $q \approx 5.4$. Debris from these collisions maintains a debris tail with the standard slope, $q \approx 3.7$, from 10–100 km. Remarkably, the largest objects accrete enough from the debris tail to maintain their population over 4.5 Gyr. Some manage to grow marginally larger.

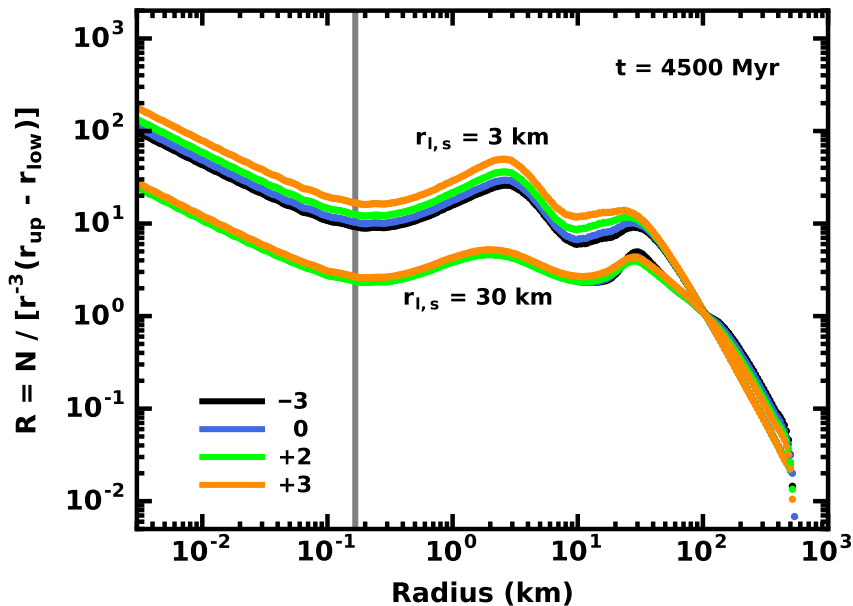


Fig. 13.— As in Fig. 12 for $r_l = 3$ and 30 km. Common features of $R(r)$ include (i) an extended debris tail with slope $q = 3.7$ at $r \lesssim 0.1$ km, (ii) a valley near the transition radius $r_t = 0.17$ km, and (iii) a peak at $r \approx 2$ km. The height of the 2 km peaks depends on r_l but not q_s . Features in the size distribution for $r \gtrsim 5$ km – including a valley at 5–10 km and peaks at 20–100 km – also depend on r_l . The slope q_s is only important for calculations with $r_l = 100$ km, where systems with small q_s have a much deeper valley at 40–50 km than those with larger q_s .

To conclude this sub-section, we compare the final size distributions (at 4.5 Gyr) for systems with $r_l = 1, 3, 10, 30,$ and 100 km and various q_s (Fig. 12 and Fig. 13). When $r_l = 100$ km and $q_s \approx -3$ (Fig. 12, lowest set of curves), populating the debris tail requires relatively rare collisions of massive objects. In calculations with progressively larger q_s , additional mass in the debris tail allows more cratering, which fills in the deep valley (or divot) at 50 km. Although $R(r)$ at 10–100 km reflects the starting q_s , the size distribution at smaller r has many of the same features as the size distributions discussed above: (i) a debris tail with a small wave at 1–10 μm and a slope $q = 3.7$ from 1 μm to 0.1 km, (ii) a clear valley near the transition radius, $r_t = 0.17$ km, and (iii) a clear peak at 2–3 km. For $r \approx 2$ –20 km, the shape of $R(r)$ clearly depends on r_l : systems with smaller r_l have more of a valley at 5–10 km. In systems with smaller r_l , the transition from the steep slope, $q \approx 5.5$, at large radius to a much shallower slope occurs at a smaller radius.

Size distributions generated in calculations with $r_l = 3$ km have the same features as those with $r_l = 1$ km (Fig. 13, upper group of plots). In both sets of calculations, the debris tail has a small wave at 1–10 μm and a slope $q = 3.7$ from 1–10 μm to the transition radius at 0.15 km. After the valley near the transition radius, size distributions for $r_l = 3$ km have a shallower rise to a peak at 2–3 km than those with $r_l = 1$ km. The evolution of this peak is also different. In systems with $r_l = 1$ km, the peak shifts from 1 km to 2–3 km over 4.5 Gyr. When $r_l = 3$ km, this peak remains at 3 km throughout the evolution. At larger radii, systems with $r_l = 3$ km have a valley at 10 km instead of 8 km and a shallow rise to a second and somewhat more prominent peak at 25–30 km instead of a more rounded shoulder at 20 km. At the largest sizes, $r \gtrsim 30$ km,

both sets of calculations maintain a very steep $R(r)$, $q \approx 5.5$ when $r_l = 1$ km and $q \approx 5.3$ when $r_l = 3$ km. Systems with $r_l = 3$ km lose $\sim 97\%$ of their initial mass in 4.5 Gyr, compared to 99% when $r_l = 1$ km.

In a slight contrast to the other calculations, the evolution of systems with $r_l = 30$ km is almost completely independent of q_s (Fig. 13, lower set of curves). Aside from a slight offset, size distributions for any q_s are identical from 1 μm to 3–4 km. As for calculations with other r_l , there is a small wave at 1–10 μm and a smooth power-law slope $q = 3.7$ from 1 μm to the transition radius, a deep valley near r_t , and a broad, shallow peak at 2 km. For larger sizes, the shallow valley at 10 km has a small variation with q_s : systems with smaller q_s have a somewhat deeper valley than those with larger q_s . Unlike systems with smaller r_l , the collision rates in these calculations are insufficient to modify the sharp peak in $R(r)$ at 30 km, whose height is fairly independent of q_s . This behavior is similar to the evolution of systems with $r_l = 100$ km, but all of the $r_l = 30$ km systems have nearly identical $R(r)$ on either side of the peak.

Systems with $r_l = 30$ km show clear signs of evolution in $R(r)$ at the largest sizes. For $r \approx 30$ –100 km, the power-law slope evolves from the initial $q = 5.5$ to $q \approx 4$ at 4.5 Gyr. Although the slope for $r \approx 300$ –500 km remains constant at $q = 5.5$, the slope for $r \approx 100$ –300 km becomes shallower, $q \approx 4.9$. Despite the unchanging slope at 300–500 km, several 500 km objects accrete debris and grow to sizes of 550–600 km. Overall, these systems lose only $\sim 75\%$ of their initial mass; nearly all of the remaining mass is in objects with $r \gtrsim 1$ km.

In all of these examples, systems with the same initial mass and $q_s \approx 3$ lose more mass than those with $q_s \approx -3$. When $q_s \approx -3$, the swarm has more mass at the peak of $R(r)$ and somewhat more mass among the largest objects. Although catastrophic encounters among equal mass objects at the peak are then more common, the lack of small particles results in many fewer cratering collisions. Compared to catastrophic collisions, cratering generates a faster flow of material from the largest objects to the smallest. Thus systems with more material initially in small objects ($q_s \approx 3$) lose more total mass than systems with more mass initially in large objects ($q_s \approx -3$).

Comparisons with published results indicate common features among the calculations. Using similar fragmentation parameters, O’Brien & Greenberg (2003) start with a shallower power-law size distribution, $q \approx 3.5$, for all sizes. Nevertheless, their calculation generates a valley near the transition radius; subsequent peaks and valleys lie close to the analytic predictions as in the calculations described above. Benavidez & Campo Bagatin (2009) consider the evolution of solids with similar initial masses and fragmentation parameters, but larger collision velocities. For their fragmentation parameters, $r_t \approx 0.08$ –0.15 km. Curiously, their calculations do not show a distinct valley at r_t ; in between deep valleys at 1–2 km and 40–60 km, their Fig. 4 has an obvious peak at 10 km (see also Campo Bagatin & Benavidez 2012). In these calculations, the larger v shifts other features in $n(r)$ to larger sizes compared to our results; the lack of a valley at the transition radius may be due to (i) differences in the fragmentation algorithm, which distributes debris among lower mass bins, (ii) the treatment of the evolution of small particles and a small-size cutoff at 1–10 cm instead of 1 μm , (iii) an inflection point in the initial $n(r)$ at 100 km, which might initiate a set of waves not considered in the analytic model and not established in our calculations, (iv) the inclusion of populations with different collision velocities, which might wash out peaks and valleys in the size distribution, or (v) the design of their figures which may understate peaks and valleys at small sizes.

Campo Bagatin & Benavidez (2012) follow the evolution of systems with a power law $n(r)$ at $r \geq 100$ km and no smaller solids. As in our calculations with $r_l = 100$ km and $q_s = -3$, collisions among 100 km and larger objects are too infrequent to fill in the valley (divot) at 50–100 km. Unlike our results, their size distributions are featureless power-laws over 0.1–30 km with little evidence for significant peaks and valleys

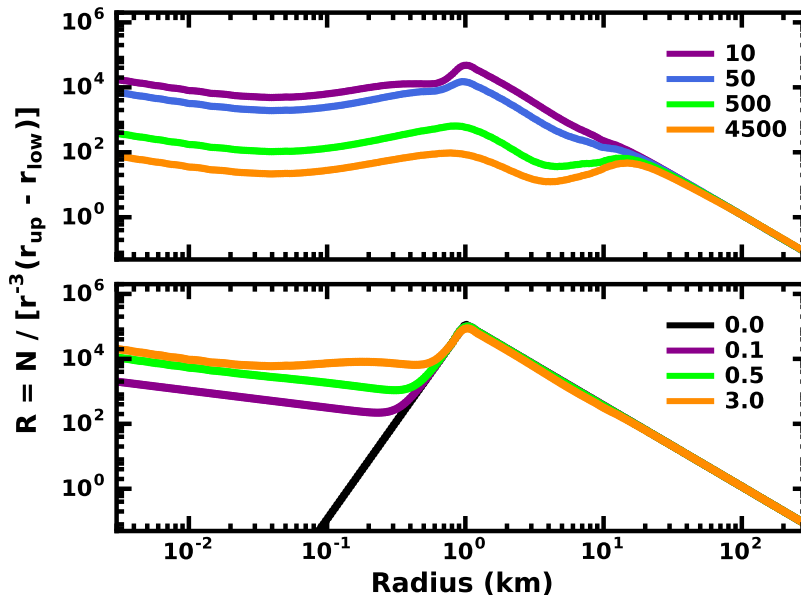


Fig. 14.— Evolution of $R(r)$ for a ring with initial mass $M_0 = 45 M_\oplus$, $r_s = r_t = 1$ km, $q_t = 5.5$, and $q_s = -3.0$, and the normal ice parameters. Evolution times in Myr are listed in each panel. *Lower panel:* During the first 3 Myr, collisions generate a substantial fragmentation tail which fills in much of the deep valley at $r \lesssim 1$ km in the initial state. *Upper panel:* After 10 Myr, collisions deplete material from the peak of the size distribution at 1 km, generating a wavy $R(r)$ with two distinct valleys, 0.01–0.1 km and 3–5 km, and two peaks, 1 km and 10–20 km.

as in Fig. 12.

5.2.2. Calculations with Normal Strength Ice

In calculations with normal ice, small objects have less tensile strength than strong ice particles. The transition radius, $r_t = 0.029$ km, and the minimum strength, $Q_t \approx 1.5 \times 10^5$ erg g $^{-1}$, are 6–8 times smaller than values with the strong ice parameters (Table 1). The difference in Q_D^* grows to a maximum of 17.5 for $r \lesssim 1$ m. Among particles with $r \gtrsim r_t$, the difference in the binding energy gradually diminishes; for $r \gtrsim 1$ km, the binding energies in the two models are nearly identical.

From the analytic model, we expect the evolution of normal ice calculations to follow closely those of model (1). Collisions among 1–100 km planetesimals generate substantial debris which drives a robust cascade. As the cascade proceeds, $R(r)$ should be somewhat wavier, with a clear valley close to the transition radius. Despite the smaller bulk strengths, the rates collisions remove large objects from the grid should be roughly similar as in the strong ice calculations. Thus, these systems should lose roughly the same amount of material over 4.5 Gyr.

Fig. 14 confirms these expectations. Starting from a swarm with most of the mass in 1 km objects, catastrophic collisions produce substantial debris in a few Myr. For $r \lesssim 0.01$ km, the size distribution follows

a smooth power-law with $q \approx 3.7$; at 1–10 μm , a modest wave steepens the slope to $q \approx 4.7$. By 3–10 Myr, the system has a clear valley at 0.03–0.04 km, a slight peak at 0.2–0.4 km, and a second valley at 0.7 km. The second valley resembles the divots identified in previous simulations (e.g., Fraser 2009; Campo Bagatin & Benavidez 2012).

As the cascade proceeds, material lost in the catastrophic collisions of large objects and numerous cratering collisions of pebbles with 1 km objects wash out the features at 0.1–1 km. At 500 Myr, $R(r)$ exhibits a characteristic shape, with a distinct valley at 0.03–0.04 km, a rounded peak at 1 km, and a second valley at 5 km. Despite the clear evolution for $r \lesssim 10$ km, $R(r)$ at $r \gtrsim 20$ km is unchanged: collisions remove a few objects with $r \approx 10$ –40 km, but do not have enough time to destroy much larger objects.

Compared to the results of model (1) in Fig. 8, the final size distribution at 4.5 Gyr for the normal ice calculation in Fig. 14 shows many common features. Starting at the largest sizes, the evolution of both calculations has negligible impact on objects with $r \gtrsim 20$ –30 km. For the starting mass ($45 M_{\oplus}$) and slope ($q = 5.5$), the time scale to remove a substantial amount of mass from the largest objects is much longer than 4.5 Gyr. At smaller sizes, dramatically shorter collision times allow significant evolution. The combination of catastrophic and cratering collisions builds a valley in $R(r)$ close to r_t , a peak at larger radius, and a second valley between the peak and the unchanged portion of $R(r)$ at $r \gtrsim 20$ –30 km. In model (1), the larger r_t results in a main peak at 3 km; the six times smaller transition radius with the normal ice parameters maintains a peak close to the original peak of 1 km. In turn, the locations of these peaks set the radius of the second valley, roughly 8 km for model (1) and only 4 km for model (2).

After 4.5 Gyr, the collision cascade with the normal ice parameters removes slightly less mass (98.6%) from the grid than with the strong ice parameters (98.7%). With a smaller r_t , the calculation shown in Fig 14 always has somewhat less mass in solids with $r \lesssim r_t$ than the calculation with the strong ice parameters. A smaller mass generates fewer cratering collisions and a smaller flow of mass from the largest objects to the smallest objects. With somewhat more mass in the largest objects, this calculation also generates more debris in catastrophic collisions. Overall, these differences almost precisely balance, yielding a total mass loss nearly identical to mass loss with the strong ice parameters.

Calculations with different initial r_l and q_s yield similar outcomes. When $r_l = 1$ km and $q_s > -3$ (Fig. 15, upper set of curves), systems begin the calculation with more solids in bins with $r \lesssim 1$ km. From the start of the calculation, this material creates a flurry of cratering collisions, which remove substantial amounts of mass from the largest size bins. Over time, the increased flow of mass from the largest objects to the smallest objects (and then out of the grid entirely) results in a somewhat smaller mass at the end of the calculation. The total mass removed ranges from 98.6% of the initial mass for $q_s = -3$ to 98.7% ($q_s = 0$) to 99.1% ($q_s = 3$).

Despite the different final masses, all calculations with $r_l = 1$ km have nearly identical final $R(r)$. For mass bins with $r \gtrsim 175$ km, the size distribution at 4.5 Gyr is identical to the starting point. Smaller size bins suffer losses, ranging from 1–2 objects at $r \approx 150$ –170 km to a reduction by more than three orders of magnitude for $r \approx 1$ km. At 20–200 km, the slope of $R(r)$ falls from the initial $q_l = 5.5$ to $q = 5$. Among smaller particles, $R(r)$ then drops to a valley at 4 km, rises back to a peak at 0.8–1 km, falls to another valley just short of the transition radius at 0.04 km, and then rises with a slope $q = 3.7$ to 10–20 μm . The small-size cutoff generates a much steeper slope, $q = 4.7$, at 1–10 μm .

Results for systems with $r_l = 10$ km follow a similar pattern (Fig. 15, middle set of curves). With more mass tied up in the largest objects, more mass bins become involved in the evolution. Here, all bins with $r \lesssim 300$ km lose at least one particle. Thus, the slope of the size distribution remains constant at $q = 5.5$ for $r \approx$

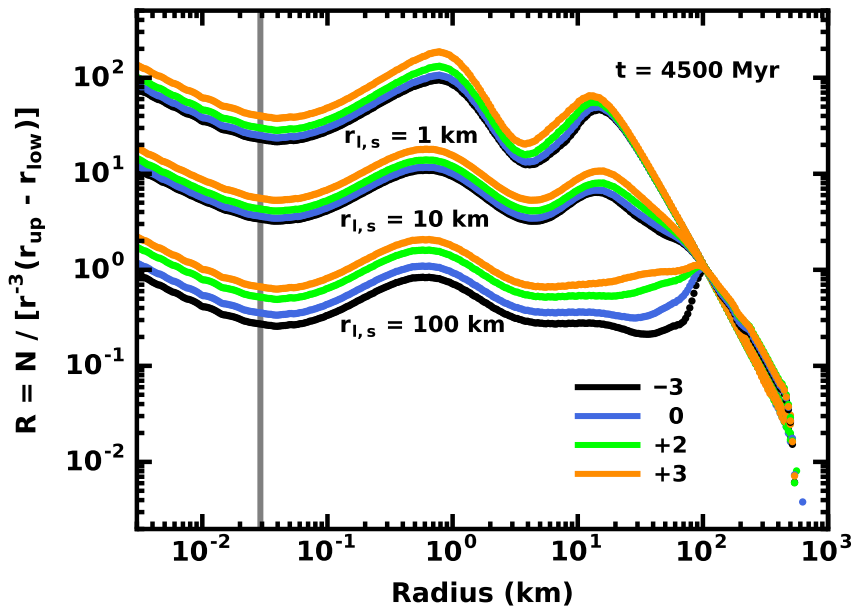


Fig. 15.— Final size distributions at 4.5 Gyr for systems with $r_s = r_l = 1$ km (upper set of curves), 10 km (middle set of curves), and 100 km (lower set of curves), values of q_s listed in the legend, and the normal ice fragmentation parameters. The vertical line indicates the transition radius, $r_t = 0.029$ km. Compared to results with the strong ice parameters, these systems have wavier $R(r)$ with more pronounced peaks and valleys.

300–500 km, declines to $q = 5.2$ for $r \approx 100$ –300 km, and then falls to $q = 4.4$ for $r \approx 20$ –100 km. For $r \lesssim 20$ km, $R(r)$ is identical to calculations with $r_l = 1$ km, with deep valleys at 0.4 km and 4 km surrounding a peak at 0.7–0.8 km. These size distributions are less wavy than those with $r_l = 1$ km.

With more mass initially in the largest objects, these systems retain much more mass. A ring with $M_0 = 45 M_\oplus$ and $q_s = -3$ loses 90% of its mass in 4.5 Gyr. Larger q_s yields a ring with less mass after 4.5 Gyr: 9.6% of the initial mass for $q_s = 0$ and 7.3% for $q_s = 3$. As in other calculations described earlier, systems with larger q_s have more mass initially in small objects. Aside from being closer to the small-size cutoff at $1 \mu\text{m}$, small objects start to remove mass from the largest objects sooner, resulting in more mass loss overall.

In systems with $r_l = 100$ km, the evolution has a different character (Fig. 15, lower set of curves). When $q_s = -3$ (black curve), nearly all of the mass starts in 100 km objects with long collision times ($t_0 \approx 800$ Myr; Eq. 26) and even longer evolution times ($\tau_0 \approx 3$ Gyr, Table 2). Over ~ 1 Gyr of evolution, most of the 100 km objects experience at least one catastrophic collision which generates significant debris. Cratering collisions from the debris then begin to remove mass from the swarm of 100 km objects. By the end of the calculation, $R(r)$ of the debris at $r \lesssim 2$ –3 km looks almost identical to $R(r)$ with $r_l = 1$ km or 10 km: a valley at 3–4 km, a rounded peak at 1 km, another valley near the transition radius, a smooth power law at $r \approx 10 \mu\text{m}$ to 0.01 km with $q = 3.7$, and a steeper power law with $q = 4.7$ at 1 – $10 \mu\text{m}$.

Among larger objects, the size distribution is very different. Initially, these systems have no objects with $r \gtrsim 500$ km; after 4.5 Gyr, they have more than 300. When $r_l = 1$ km or 10 km, the population of objects

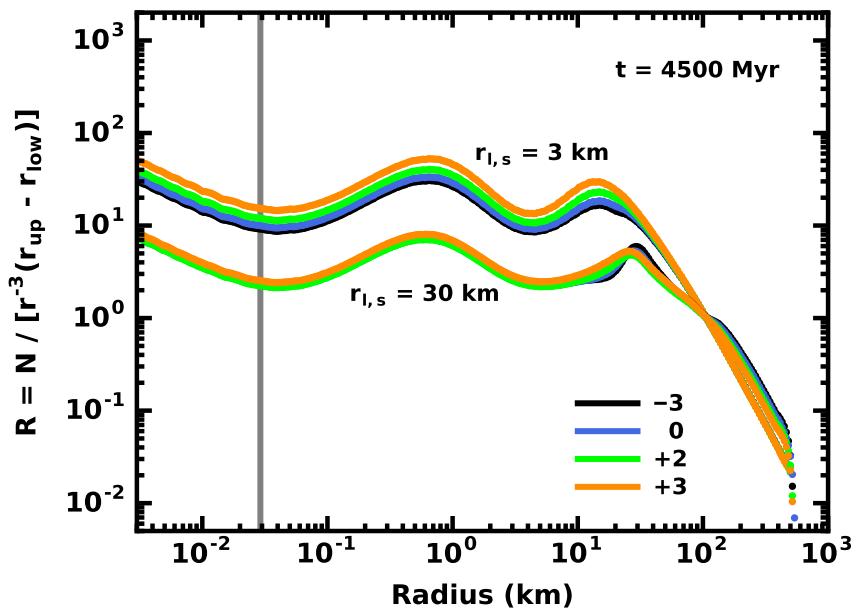


Fig. 16.— As in Fig. 15 for $r_s = r_l = 3$ km (upper set of curves) and 30 km (lower set of curves).

with $r \approx 200$ – 500 km is nearly unchanged after 4.5 Gyr. In systems with $r_l = 100$ km, nearly all particles with $r \approx 300$ – 500 km accrete some material from the rest of the swarm in 4.5 Gyr. Smaller particles lose mass: after 4.5 Gyr, the number of 100 km (200 km) objects is 50% (40%) smaller than in the initial state.

The disparate evolution among large and small objects creates a wavy $R(r)$ among the largest objects. For $r \approx 100$ – 500 km, $n(r)$ is a wavy power law with typical $q \approx 5$. The number of objects is roughly constant at $r \approx 30$ – 100 km, generating a deep divot in the R -plot shown in Fig. 15. The number of objects then grows with decreasing radius, producing a small peak at 10–20 km and an equally tiny valley at 4–5 km.

Systems with larger q_s have fewer features in the sizes distribution. When $q_s \geq -2$, growth of the largest objects is restrained; collisions generate only 200 (50) objects with $r \gtrsim 500$ km when $q_s = 0$ (3). Size distributions from 100 km to 500 km are then smoother, with smaller waves for larger q_s . Larger q_s also yields smaller divots at 30–100 km; instead of a flat $R(r)$ at 4.5 Gyr with $q \approx 0$ (for $q_s = -3$), systems with $q_s = 0$ – 3 have smoother power-laws with $q \approx 2$.

Independent of q_s , size distributions for $r \lesssim 3$ km have the same features. As in calculations with $r_l = 1$ km or 10 km, $R(r)$ rises from a valley at 3 km to a rounded peak at 1 km. All systems display a deep valley at 0.03–0.04 km, just larger than the transition radius, $r_t = 0.029$ km. The distribution then rises steeply from 0.01 km to 10 μm , with power-law slope $q = 3.7$, and concludes with a steeper rise from 10 μm to 1 μm with slope $q = 4.7$.

As with the strong ice models, results for $r_l = 3$ km and 30 km and the normal ice are nearly independent of q_s (Fig. 16). When $r_l = 3$ km, the locations of peaks and valleys at 0.1–30 km match those for $r_l = 1$ km and 10 km; the amplitude of the waviness lies between the levels derived for 1 km and 10 km. At $r \approx 20$ – 500 km, the $q = 5$ slope of the power-law is smaller than the initial $q_s = 5.5$. For $r \approx 1$ μm to 0.01 km, there is a smooth power-law with $q = 4.7$ at 1–10 μm that transitions into another smooth power-law with

$q = 3.67$ at $10 \mu\text{m}$ to 0.01 km .

Results for $r_l = 30 \text{ km}$ follow a similar trend. Aside from a normalization factor, $R(r)$ at 4.5 Gyr for systems with $r_l = 30 \text{ km}$ and any q_s closely follow those with $r_l = 1\text{--}10 \text{ km}$ from $r = 1 \mu\text{m}$ to $r \approx 10 \text{ km}$. At larger sizes, the shape depends on q_s . Systems with $q_s \approx -3$ have a narrow and somewhat taller peak at 30 km than those with $q_s \approx 3$. For $r \approx 100\text{--}500 \text{ km}$, all systems have a featureless power-law with $q \approx 5$ and a few larger objects that have accreted material from the rest of the swarm. At these large sizes, the main difference between calculations with $r_l = 30 \text{ km}$ and those with $r_l = 1\text{--}10 \text{ km}$ is the collision time. Over 4.5 Gyr , systems with $r_l = 30 \text{ km}$ do not suffer enough destructive collisions to round-off or shift the initial peak at 30 km . Longer time scale calculations would probably yield a more rounded peak at $20\text{--}30 \text{ km}$ with a similar shape for all q_s .

5.2.3. Calculations with Weak Ice

In weak ice models, we expect wavier $R(r)$ than with strong or normal ice. Among particles with $r \lesssim 0.1 \text{ km}$, bulk strengths are small. The minimum Q_D^* is $Q_t \approx 2 \times 10^4 \text{ erg g}^{-1}$ at a transition radius $r_t \approx 5 \text{ m}$ (model 3) or 8 m (model 4). At $r \approx 1\text{--}10 \mu\text{m}$, the binding energy is $20\text{--}350$ times smaller than for strong or weak ice. For a fixed v , collisions among particles with smaller binding energies should produce size distributions with larger waves at the smallest sizes. These waves may extend close to the transition radius, changing the morphology of waves generated at the minimum Q_t . Thus, we expect more complicated size distributions than those in the strong ice or normal ice calculations.

At larger sizes ($r \gtrsim 1 \text{ km}$), the similar binding energies in the two models should yield similar outcomes as in other models. In the gravity regime, the weak ice models have identical Q_D^* at $r \approx 2 \text{ km}$. Although Q_D^* is larger (smaller) for the model (3) fragmentation parameters at smaller (larger) sizes, the differences are minor. Thus, these two sets of parameters yield similar collision and evolution times for large objects with $r \gtrsim 0.1 \text{ km}$ (Table 2). Aside from a wavier size distribution, we expect a set of peaks and valleys at $1\text{--}100 \text{ km}$ and the same steep slope at $100\text{--}500 \text{ km}$.

The evolution of collisional cascades derived from calculations with the weak ice fragmentation parameters closely follows the evolution described for stronger ice models. Catastrophic collisions among objects at the peak of the initial size distribution generate copious amount of debris with sizes ranging from $1 \mu\text{m}$ to r_l . Once these collisions produce some debris, cratering collisions add material to the cascade. On time scales of $10\text{--}20 \text{ Myr}$ ($r_l = 1 \text{ km}$) to $1\text{--}2 \text{ Gyr}$ ($r_l = 100 \text{ km}$), the cascade develops an approximately equilibrium $R(r)$ at $1 \mu\text{m}$ to several km, with peaks and valleys that stay fixed for the remainder of the calculation. In systems with $r_l = 1\text{--}10 \text{ km}$, the largest objects do not accrete significant mass from the swarm; the largest object always has $r = 500 \text{ km}$. When $r_l = 30\text{--}100 \text{ km}$, large objects grow, reaching sizes of $520\text{--}525 \text{ km}$ ($r_l = 30 \text{ km}$) to 600 km ($r_l = 100 \text{ km}$).

Despite the weaker bulk strength, swarms of weak ice particles lose less mass than those with ice or strong ice. Differences in mass loss range from a few tenths of a per cent for $r_l = 1 \text{ km}$ to $\sim 10\%$ for $r_l = 100 \text{ km}$. In weak ice systems, collisions among particles in the debris tail are more destructive. The mass in particles with $r \approx 1 \mu\text{m}$ to $1\text{--}10 \text{ m}$ is smaller in weak ice models than in stronger ice models. With less mass in the debris tail, cratering collisions remove less mass from more massive particles with $r \gtrsim 1 \text{ km}$. Given the rather small differences among the models, it is clear that mass loss is driven by catastrophic collisions among 1 km and larger particles.

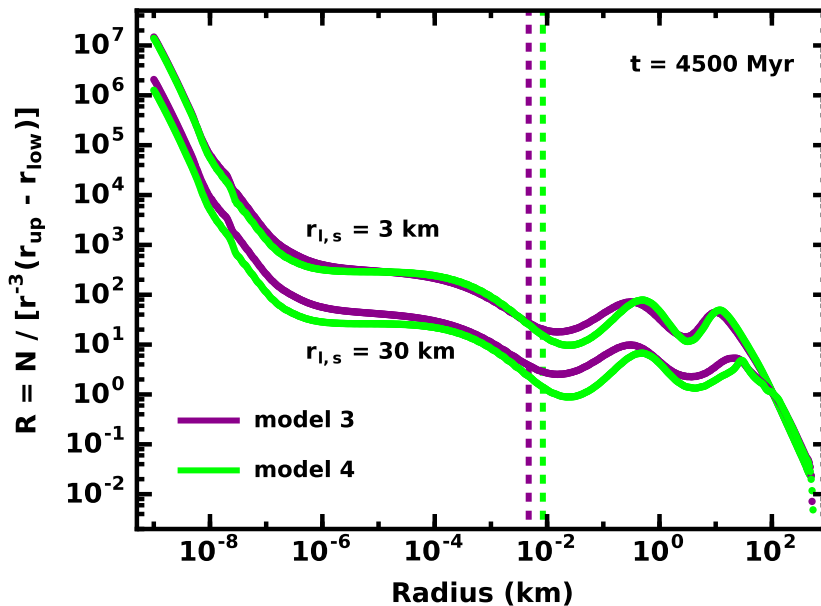


Fig. 17.— Final $R(r)$ at 4.5 Gyr for systems with $r_s = r_l = 3$ km (upper set of curves) or 30 km (lower set of curves), $q_s = 3$, and the fragmentation parameters indicated in the legend. Vertical dashed lines indicate the transition radius for each set of fragmentation parameters.

At 4.5 Gyr, the size distributions for models with $r_l = 3$ km and 30 km confirm expectations (Fig. 17). The overall shape of $R(r)$ is nearly independent of r_l and the fragmentation parameters. Particles with $r \approx 1\text{--}10 \mu\text{m}$ ($10\text{--}100 \mu\text{m}$) have a steep power-law slope $q \approx 5.3$ (4.5). These systems have a pronounced wave with valleys at $300 \mu\text{m}$, $20\text{--}30$ m, and $2\text{--}5$ km; a weak peak at 10 cm; and stronger peaks at $300\text{--}500$ m and $1\text{--}3$ km. The wave from the small-size cutoff clearly impacts the waves due to the minimum in Q_D^* ; in all systems, the radius of the deepest valley is $3\text{--}10$ times larger than r_t .

For systems with other q_s , the size distributions are similar. The small particles have a small range of power-law slopes, $q \approx 5.3\text{--}5.4$ at $1\text{--}10 \mu\text{m}$ and $4.4\text{--}4.6$ at $10\text{--}100 \mu\text{m}$. Calculations with the model (3) parameters produce shallower valleys, with the main valley marginally closer to the transition radius. The positions and heights of peaks at $5\text{--}10$ km depend little on q_s or the fragmentation parameters; however, peaks at $300\text{--}500$ m lie at smaller sizes in model (3) calculations. The size distributions of the largest particles are virtually unchanged. The typical power-law slope at $100\text{--}500$ km, $q \approx 5.2\text{--}5.4$ is close to the initial $q = 5.5$.

Calculations with $r_l = 1$ km and 10 km yield results similar to those shown in Fig. 17. At small sizes ($r \lesssim 10$ m, size distributions are nearly independent of r_l and q_s , with similar placement of peaks and valleys and little difference in power-law slopes at $1\text{--}100 \mu\text{m}$. Both sets of calculations have peaks at 400 m and 10 km. Aside from having waves with larger amplitudes, the model (4) calculations with $r_l = 1$ km and 10 km have narrower peaks somewhat closer to 1 km than the model (3) calculations. Aside from a gradual evolution to a smaller slope, all calculations show little change in the power-law $R(r)$ for $r = 100\text{--}500$.

When $r_l = 100$ km, $R(r)$ for large objects at 4.5 Gyr depends on q_s . As in the calculations with r_l

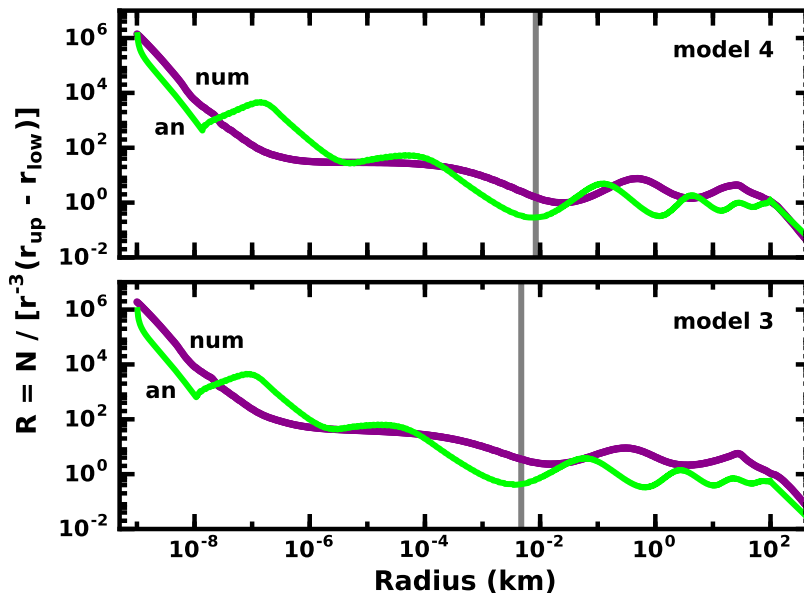


Fig. 18.— Comparison of theoretical $R(r)$ for the model (3) (lower panel) and the model (4) (upper panel) fragmentation parameters derived from the analytic model in §4.3 (‘an’; green curves) and numerical models with $r_l = r_s = 30$ km and $q_s = 3$ (‘num’; purple curves). The vertical grey line indicates the position of r_t . From $1 \mu\text{m}$ to 100 km, the level of waviness and the overall shape of $R(r)$ from the numerical models agrees well with the predictions of the analytic model. In the numerical model, the placement of peaks and valleys is displaced from the predictions of the analytic model.

$= 100$ km and the stronger ice models (see Figs. 12 and 15), a few of the largest objects reach sizes of ~ 600 km. The derived $n(r)$ follows a smooth power-law $q \approx 5$ at 100 – 500 km and then drops abruptly at 50 – 100 km. Smaller q_s leads to larger drops (divots). From 3 – 50 km, $R(r)$ has a few small amplitude waves superimposed on a power-law with $q \approx 2$ – 3 . Systems with smaller q_s have shallower slopes. Below 2 – 3 km, $n(r)$ for $r_l = 100$ km follows the results for $r_l = 1$ – 30 km: rising to a clear peak at 400 – 600 m, falling to a valley at 20 – 30 m, curving up and over to a valley at $300 \mu\text{m}$, and finally rising steeply to 1 – $10 \mu\text{m}$.

Overall, $R(r)$ derived from calculations with the weak ice parameters match the $R(r)$ inferred from the analytic model in §4.3 (Fig. 18). Over roughly 11 orders of magnitude in size – from $1 \mu\text{m}$ to 100 km – the general shapes of the two distributions are similar. In both panels, the numerical model does not possess the deep valley at $10 \mu\text{m}$ and the peak at $100 \mu\text{m}$ in the analytic model. In the lower panel of Fig. 18, the analytic model has a deep valley near the transition radius of 4.7 m and smaller valleys at 0.5 km and 10 km. In the numerical model, the waviness has a smaller amplitude; peaks and valleys are displaced to larger radius. In the upper panel of Fig. 18, the deepest valley in the analytic $R(r)$ lies just short of the transition radius; shallower valleys are at larger radii than those in model (3). The $R(r)$ in the numerical model has a similar degree of waviness with peaks and valleys at larger radii than the analytic model.

Several aspects of the calculations prevent a detailed match of the numerical model to the analytical model. In the analytical model, the rate material is removed from each mass bin sets the size distribution. Requiring a constant flow of material from the largest to the smallest mass bin allows an analytical solution

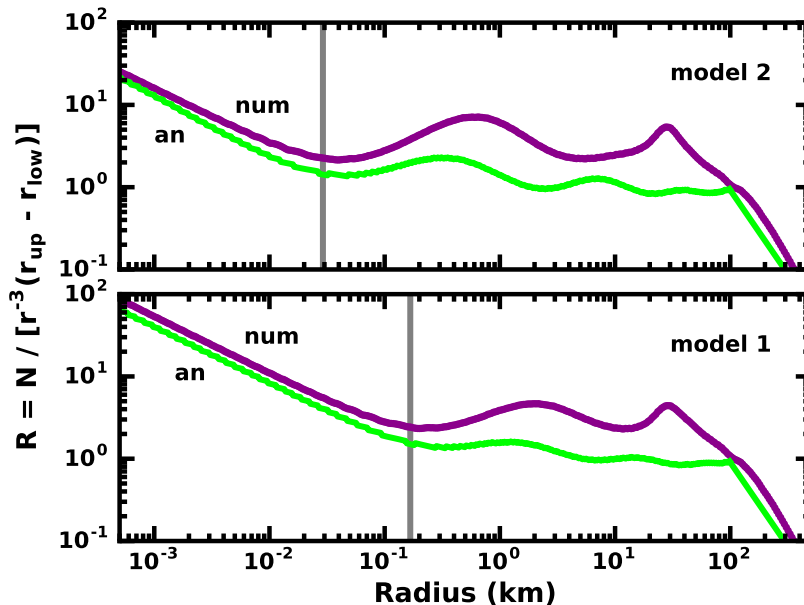


Fig. 19.— As in Fig. 18 for the strong ice (lower panel) and the normal ice (upper panel) fragmentation parameters.

(Wyatt et al. 2011). In the numerical calculations, every collision removes mass from a pair of bins and redistributes this mass among bins of lower mass. Redistribution tends to smooth out peaks and valleys in the size distribution. Among the largest objects, the requirement that the number of collisions per time step be an integer creates shot noise from one time step to the next. Redistributed mass from these occasional collisions generates pulses in the size distribution that propagate from large to small objects, further diminishing the strengths of peaks and valleys. Although most objects suffer catastrophic collisions, cratering events dominate the evolution of particles with $r \gtrsim 300\text{--}700$ km. Debris from these collisions also fills in peaks and valleys at the smallest sizes.

The lack of equilibrium at the largest sizes also prevents a good match between the analytical model and the numerical simulations. At any size, the time scale to reach an equilibrium is at least 10–20 times larger than the collision time. For $t_0 \approx 1$ Gyr and $\tau_0 \approx 3\text{--}4$ Gyr, objects with $r \gtrsim 100$ km do not have time to reach equilibrium in a 4.5 Gyr calculation. Although this lack of a complete equilibrium impacts all of $R(r)$ to some degree, material with $r \gtrsim 10$ km is much more out of equilibrium than solids with $r \lesssim 10$ km. Calculations with $r_l = 30\text{--}100$ km do not have time for collisions to smooth out the initial peak at 30–100 km and thus produce different waves than predicted by the analytic model.

The analytic and numerical results for the strong ice and normal ice parameters also agree reasonably well (Fig. 19). At the smallest sizes, $r \lesssim 0.01\text{--}0.1$ km, the two approaches are nearly indistinguishable; with little waviness, the slopes match precisely. Both approaches yield $R(r)$ with valleys at the transition radius. In the lower panel of Fig. 19, the waviness in the analytic $R(r)$ is minimal; the power-law slope is $q \approx 3$. The numerical model maintains the initial peak at 30 km, has more waves, and a power-law slope $q \approx 3$. In the upper panel, the larger waviness in the analytic model is a result of the smaller Q_s . However, the overall slope from 30 m to 100 km is still $q \approx 3$. The numerical model has a larger waviness, but a similar overall

slope $q \approx 3$ from 30 m to 100 km.

In these examples, it is simple to see how the numerical model might evolve towards the analytic model over a longer evolution time. As collisions remove more mass from the swarm at 0.1–100 km, the sharp peak at 30 km will become more rounded and eventually disappear. The debris tail at smaller sizes will maintain the equilibrium $n(r)$ with slope $q \approx 3.7$. This evolution will have little impact on solids at 200–500 km, which will retain a size distribution with a steep slope $q \approx 4$ –5. At 0.1–10 km, collisions will likely preserve the shallow slope $q \approx 3$ and perhaps develop the same waviness as the analytic model. For the parameters in these calculations, we estimate the time scale to reach this equilibrium is ~ 30 –40 Gyr, much longer than the age of the Solar System.

Despite the large difference in fragmentation parameters, size distributions for $r = 1$ m to 500 km at 4.5 Gyr for models (1)–(4) have many similar features (Fig. 20). For models (2)–(4), the first valley is at a radius $r \approx 10$ –50 m (Fig. 20, blue, green, and orange curves); this valley is close to the transition radius for model (2) and much larger than r_t for models (3) and (4). In systems with the strong particles of model (1), the first valley lies at 300–400 m (Fig. 20, black curve), somewhat larger than the transition radius. In all four examples, the first peak is at a radius roughly ten times larger than the first valley. Systems with weaker particles have a larger wave amplitude than those with stronger particles. Following the first peak, the second valley is at 5–10 times larger radius. In the example shown, there is enough room for a second peak and then the sharp power-law decline from 30–40 km to 500 km.

Neglecting the details of the waviness in Fig. 20, these size distributions share three main features. At large sizes, $r \approx 30$ –100 km to 500–600 km, $n(r)$ is a power law with a slope q ranging from 4–5 at 30–200 km and 5.0–5.5 at 200–500 km. At intermediate sizes, $r \approx 0.01$ –0.1 km to 10–30 km, $n(r)$ has a wavy pattern superimposed on a shallow power-law with $q \approx 3$. Finally, at the smallest sizes ($r \lesssim 0.01$ km), $n(r)$ is a steeper power-law with a typical $q \approx 3.7$. For ice and strong ice, this steeper power-law has very little waviness. Although waviness dominates the power-law in weak ice calculations, the change in $n(r)$ from 1 μm to 1–10 m is the same as a power-law with $q \approx 3.7$ –3.9.

These calculations show that the degree of waviness at 0.1–100 km depends on particle strengths. Strong ice models have waves with an amplitude in $R(r)$ of 2–4 (Figs. 10, 12, and 20). While consistent with the *New Horizons* data at 1–10 km, these models never develop a factor of ten wave at 0.1–1 km in any calculation. The normal ice models feature larger waves with amplitudes as large as a factor of five (Figs. 14, 15, and 20), which falls a factor of two short of the required amplitude. While the two weak ice models do not generate a valley (peak) at the observed 0.1 km (0.5–1.0 km), the amplitude and wavelength of features in $R(r)$ are similar to those in the data.

5.3. Variations on the Standard Parameters

With eight parameters to characterize each collisional cascade model (see Table 1), it is not feasible to make an exhaustive exploration of the available parameter space outside the ‘standard’ parameters considered above. Here, we consider several variants on models (1)–(4), with the goal of understanding how the shape of the size distribution at 0.1–100 km depends on the input parameters.

For fixed collision velocity and fragmentation parameters, calculations with different values of b_d , $m_{l,0}$, and b_l yield results that are indistinguishable from those with the standard parameters. Although $n(r)$ is somewhat sensitive to b_d for collisional cascades at 1 au (Kenyon & Bromley 2016), tests with $b_d = 9/8$ for

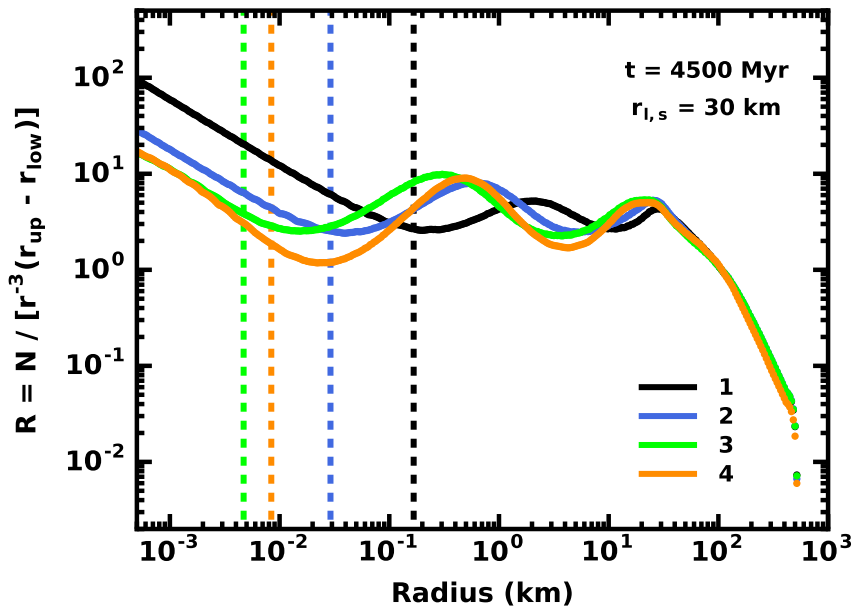


Fig. 20.— Comparison of $R(r)$ for $r_l = r_s = 30$ km at 4.5 Gyr for the model fragmentation parameters listed in the legend. Vertical dashed lines indicate the position of the transition radius for the appropriate fragmentation model. Aside from the details of the wavy patterns, all models share three features: (i) a power-law with $q \approx 3.7$ at $1 \mu\text{m}$ to 10–100 m, (ii) a wavy distribution superimposed on a power-law with $q \approx 3$ at 10–100 m to 30–100 km, and (iii) a steep power-law with $q \approx 4.5$ –5.5 at 100–500 km.

solids at 45 au generate nearly identical $R(r)$ as those with $b_d = 1$. Additional tests with $(m_{l,0}, b_l) = (0.2, 1.0)$ and $(0.5, 0.75)$ instead of $(0.2, 0.0)$ suggest $n(r)$ for icy objects at 45 au and at 4.5 Gyr is independent of these parameters.

To explore the sensitivity of waves to Q_s , we consider calculations with $Q_s = 10^4 \text{ erg g}^{-1} \text{ cm}^{0.4}$ (model (6), Fig. 7, orange curve) and $Q_s = 10^3 \text{ erg g}^{-1} \text{ cm}^{0.4}$ (model (7), Fig. 7, wheat curve). In calculations with larger Q_s , Q_g and e_g have little impact on the shape of the size distribution. Thus, we adopt the Leinhardt & Stewart (2012) parameters for the gravity component of Q_D^* , which generate somewhat larger waves in the size distribution at 1–100 km. To make a tighter connection to results with the analytic model, we set $e_s = -0.4$. In the next suite of calculations, we examine results for different values of e_s .

Fig. 21 compares results for calculations with $r_l = r_s = 100$ km. All calculations show a pronounced peak in $R(r)$ at $r = 100$ km. Within a $45 M_\oplus$ swarm of solids at 30–60 au, the time scale for catastrophic collisions to remove a substantial fraction of 100 km objects is long, $\gtrsim 5$ –10 Gyr (Table 2). Thus, the slope of the size distribution at 100–500 km is remarkably stable over 4.5 Gyr, with $q \approx 5.1$ for all models. Several of the largest objects with $r \approx 400$ –500 km gradually accrete debris from the rest of the swarm and reach sizes of ~ 600 –650 km. Although these objects gain significant mass, they are few in number: ~ 5 –10 with radii as large as 600–650 km.

For radii $r \approx 0.1$ –100 km, the overall slope of $R(r)$ is flat, with $q \approx 3$ for all models. Systems with strong ice have a modest wave, with valleys at 0.2 km and 40–50 km and a peak at 2 km. For systems with

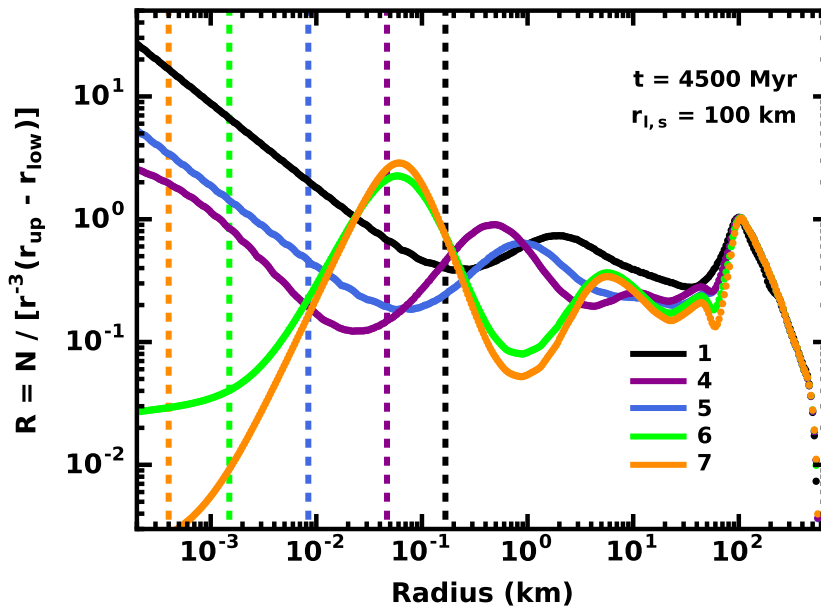


Fig. 21.— Comparison of $R(r)$ for $r_l = r_s = 30$ km at 4.5 Gyr for the model fragmentation parameters listed in the legend. Vertical dashed lines indicate the position of the transition radius for the appropriate fragmentation model. Aside from the details of the wavy patterns, all models share three features: (i) a power-law with $q \approx 3.7$ at $1 \mu\text{m}$ to $10\text{--}100$ m, (ii) a wavy distribution superimposed on a power-law with $q \approx 3$ at $10\text{--}100$ m to $30\text{--}100$ km, and (iii) a steep power-law with $q \approx 4.5\text{--}5.5$ at $100\text{--}500$ km.

weaker ice, peaks and valleys lie at smaller radii; the amplitude of the wave grows. In models (4) and (5), the amplitude of the wave is small at $5\text{--}100$ km and then grows dramatically at smaller radii. In models (6) and (7), there is a significant wave for $r \lesssim 20\text{--}30$ km. Model (6) has a deep valley at $r = 1$ km and a peak at 6 km, with a peak to valley amplitude of 4.5. For $r \gtrsim 0.01$ km, model (7) has the same wavy size distribution as model (6), with valleys and peaks at the same locations but a larger peak-to-valley amplitude. Although the waves at $0.1\text{--}100$ km in model (6) and model (7) have as large an amplitude as the wave in the *New Horizons* data, the positions of the peaks and valleys do not match.’

At the smallest sizes, $r \lesssim 0.1$ km, waviness is a strong function of Q_s . In model (1), the size distribution follows a power-law with $q \approx 3.7\text{--}3.8$ from r_t to $1 \mu\text{m}$. Reducing Q_s by a factor of $\sim 20\text{--}300$ for models (5) and (6) results in a similar slope $q \approx 3.6\text{--}3.8$ from r_t to $10 \mu\text{m}$ and a much steeper slope $q \approx 4.9\text{--}5.4$ at $1\text{--}10 \mu\text{m}$. In model (6), the overall size distribution is rather flat, $q \approx 2.5\text{--}3$, with a large peak at $0.05\text{--}0.07$ km and a very deep valley at $0.01\text{--}10$ m. For $r \lesssim 1$ cm, there is a sharp rise in $R(r)$. At $1\text{--}10 \mu\text{m}$, the slope of $q \approx 5.4$ is similar to the rise in model (4). However, the slope at $10 \mu\text{m}$ to 1 cm, $q \approx 4.5$, provides a clear measure of the steep slope of the size distribution below the deep valley at $0.01\text{--}10$ m. In model (7), the $q \approx 5.41$ at $1\text{--}10 \mu\text{m}$ follows the slope in model (6); however, the rise from 1 cm to $10 \mu\text{m}$ is more dramatic, with $q \approx 4.85$.

To understand how the shape of the size distribution depends on the bulk strength component of Q_D^* in more detail, we perform calculations with different values for e_s (Fig. 7, compare solid, dashed, and dot-dashed lime curves). In models (8) and (9), particles have the bulk strength of normal ice and the Leinhardt

& Stewart (2012) parameters for the gravity component. In model (9), the strength component of Q_D^* is independent of radius, $e_s = 0$. For model (8), the exponent $e_s = -0.2$ lies midway between the standard values, $e_s = -0.45$ to -0.4 , and $e_s = 0$.

Fig. 22 compares a set of $R(r)$ at 4.5 Gyr for calculations with $r_{l,s} = 30$ km. In the standard normal ice models (2) and (5), the size distributions have a sharp peak at 30 km, where catastrophic collisions have been unable to destroy most of the initial set of objects in 4.5 Gyr. In model (2), calculations with the Benz & Asphaug (1999) parameters for the gravity component of Q_D^* generate a shallow trough at 3–20 km, a broad peak at 700 m, and a valley near the transition radius at 29 m (Fig. 22, black curve). When we switch to the Leinhardt & Stewart (2012) parameters for the gravity component (Fig. 22, blue curve), the larger transition radius, $r_t = 47$ m, pushes the features in $R(r)$ to larger sizes. However, the amplitude of the waves is independent of the parameters.

In model (8), the shallower slope of the strength component of Q_D^* generates smaller waves in $R(r)$ (Fig. 22, green curve). When $e_s = -0.2$, $r_t = 89$ m. Although the first valley in $R(r)$ is at a larger radius, 200–300 m, the shape of $R(r)$ from 1 μm to the valley is similar to models with smaller e_s . With the first peak at 2–3 km and a second valley at 10–15 km, the waviness in this model has a somewhat smaller wavelength than in the standard models (2) and (5). The shape between the first peak and the second valley is also different: roughly sinusoidal in model (8) compared to a flatter trough in models (2) and (5). Despite these differences, the size distribution in model (8) has the same sharp peak at 30 km, a power-law slope $q \approx 4.1$ at 30–100 km, and a power-law slope $q \approx 5.3$ at 100–500 km. As in models (2) and (5), some of the largest objects accrete material from the rest of the swarm. Compared to models with $r_l = r_s = 100$ km, growth is limited, reaching sizes of 600 km (instead of 700 km) in 4.5 Gyr.

In model (9) calculations, setting $e_s = 0$ does not allow a transition radius. Size distributions with these parameters are more featureless (Fig. 22, orange curve). Aside from a power-law slope $q \approx 3.8$ (3.7) from 1 μm to 1 cm (10 m), $R(r)$ has an inflection point at $r \approx 1$ km where the size distribution becomes fairly flat, a shallow dip at 10 km, and a sharp rise to a peak at 20–30 km. Despite these differences, the size distribution at larger r is similar to that in models (2), (5), and (8): a power-law slope $q \approx 4.1$ at 30–100 km and a slope $q \approx 5.3$ at 100–500 km. Modest accretion from the rest of the swarm allows the largest objects to reach sizes $r \approx 600$ km after 4.5 Gyr.

These examples illustrate the difficulties in generating $R(r)$ with a waviness larger than that derived with the standard fragmentation parameters. At the largest sizes, the total mass sets the collision time; when $r_l = r_s = 30$ –100 km, collisions among the largest objects are rare. The shape of the size distribution remains close to the initial one over 4.5 Gyr of evolution. At smaller sizes, $R(r)$ has a clear waviness superimposed on a fairly flat power-law with $q \approx 3$ from 0.1 km to 10 km. Decreasing the slope of the bulk strength component in Q_D^* leads to smaller waves.

Fragmentation parameters outside the range considered here are probably not physically plausible. Several studies of the energy required for catastrophic fragmentation of 1–1000 km asteroids (e.g., Davis et al. 1985; Housen & Holsapple 1990; Love & Ahrens 1996) yield values for Q_D^* intermediate between those of Benz & Asphaug (1999) and Leinhardt & Stewart (2012). Although TNOs are icier than typical asteroids, it seems unlikely that the gravity component of Q_D^* can be much smaller than the relation derived by Leinhardt & Stewart (2012). Among investigations for small sizes, the coefficients derived for the bulk strength component of Q_D^* for asteroids are similar to the value adopted for model (1), with a slope $e_s \approx -0.2$ to -0.6 (e.g., Farinella et al. 1982; Housen & Holsapple 1990; Holsapple 1994; Housen & Holsapple 1999). Our choices allow for a much smaller strength for ice, while retaining ‘standard’ values for the variation with

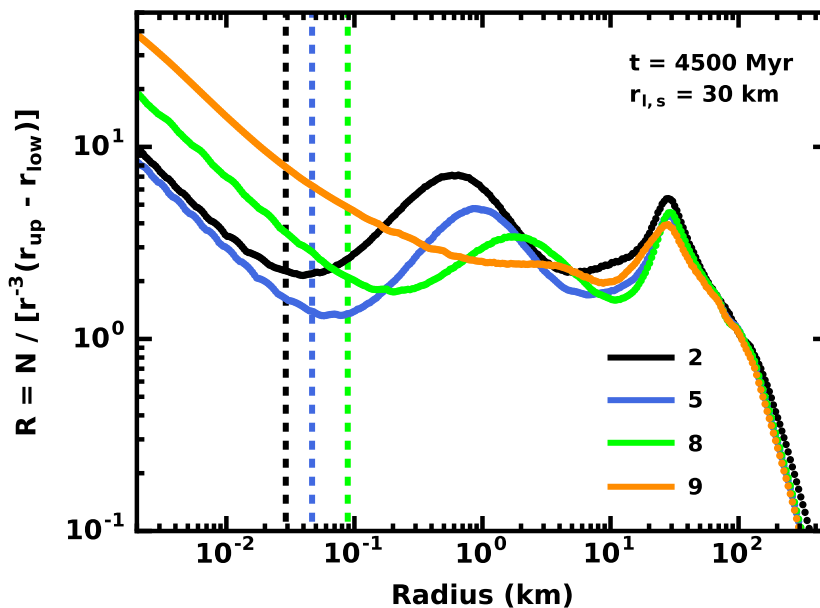


Fig. 22.— As in Fig. 21 for $r_l = r_s = 30$ km at 4.5 Gyr. All calculations have the same Q_s . Aside from the pronounced at 30 km common to all calculations, the degree of waviness is more sensitive to e_s (compare blue, green, and orange curves) than to gravity component of Q_D^* (compare black and blue curves). Systems with $e_s = 0$ have much less wavy $R(r)$ than systems with $e_s = -0.2$ or -0.4 .

radius.

Aside from these studies, Durda et al. (1998) derived much steeper relations for asteroids in both the strength and gravity regimes. Their minimum $Q_D^* \approx 1-2 \times 10^4$ erg g^{-1} is similar to the $Q_t \approx 1.8 \times 10^4$ erg g^{-1} in models (3) and (4), but at a transition radius, $r_t \approx 70$ m, intermediate between the r_t for models (1) and (2). Although inferred to match properties of the size distribution of asteroid, we considered several test calculations with the Durda et al. (1998) relation for Q_D^* . In our approach, the large values for e_s and e_b make calculations of collisional cascades somewhat delicate. Nevertheless, several tests suggest this relation will not yield size distributions for TNOs substantially different from results in models (1)–(11).

In a final suite of calculations, we consider how the collision velocity shapes the size distribution. For the normal ice bulk strength and the Leinhardt & Stewart (2012) gravity parameters for Q_D^* , model (10) has $v = 1.4$ km s^{-1} ; model (11) has $v = 2$ km s^{-1} . With these parameters, v^2/Q_D^* is twice as large in model (10) as in model (5); v^2/Q_D^* is four times larger in model (11). Based on results for the analytic size distribution (Figs. 2–5), systems with larger v^2/Q_D^* should have wavier size distributions.

Fig. 23 illustrates the impact of the collision velocity on systems with $r_l = r_s = 10$ km. All three calculations generate a deep valley near the transition radius, $r_t = 47$ m. At the smallest sizes, the power-law slopes for $R(r)$ in model (10) are $q \approx 5.1$ at $1-10 \mu\text{m}$, 3.5 at $10 \mu\text{m}$ to 1 cm, and 3.6 at $10 \mu\text{m}$ to 10 m. Power-law slopes in model (11) are nearly identical: $q \approx 5.2$ at $1-10 \mu\text{m}$, 3.5 at $10 \mu\text{m}$ to 1 cm, and 3.6 at $10 \mu\text{m}$ to 1 m. Compared to model (5), which has identical fragmentation parameters and $v = 1$ km s^{-1} , the size distributions of these models have somewhat steeper slopes at $1-10 \mu\text{m}$ ($q \approx 5.1-5.2$ instead of $q \approx$

4.9) and somewhat shallower slopes at large sizes ($q \approx 3.5$ – 3.6 instead of $q \approx 3.6$ – 3.7). Although the size distributions are wavy at small sizes, the waves are not large.

For sizes $r \gtrsim 0.1$ km, systems with larger collision velocities have wavier size distributions with longer wavelengths between peaks and valleys. In Fig. 23, all three models have peaks at similar levels in $R(r)$ at 1 km. In model (11), valleys at the transition radius and at 8–10 km (Fig. 23, orange curve) are much deeper than those in model (5) or model (10). The size distribution in model (11) has a peak at a larger radius, ~ 30 km, than those in model (5), ~ 15 km, or in model (10), ~ 20 km. Despite these differences, the overall shapes of the size distributions are fairly similar.

At the largest sizes, $R(r)$ is nearly independent of v . Calculations with $v = 1$ km s $^{-1}$ have a small shoulder in the size distribution at 50 km, which is absent in calculations with larger v . Despite the missing shoulder, the power-law slope at 100–500 km changes little with v . At low velocities, $q \approx 5.1$ – 5.6 for $r_t = 100$ – 1 km. When $v = 2$ km s $^{-1}$, $q \approx 5.0$ – 5.6 . However, the growth of the largest objects is more sensitive. At $v = 1$ km s $^{-1}$, the largest objects reach sizes of 650 km. The largest objects grow only to 575–600 km when $v = 2$ – 1.4 km s $^{-1}$.

To facilitate comparisons between these results and other calculations, Table 3 summarizes results from the full suite of numerical calculations described above. For each combination of fragmentation parameters and r_t , the Table lists the ratio of the final mass (at 4.5 Gyr) to the total mass, the radius of the largest object in the grid, the power-law slope for five specific size intervals, the radius r_v of the first valley at or larger than the transition radius, the first peak r_p with $r > r_v$, and the amplitude of the wave between r_p and r_v , $A_{pv} = R(r_p)/R(r_v)$. The five power-law slopes span the full range of radii in the size distribution; q_1 : 1–10 μm , q_2 : 10 μm to 1 cm, q_3 : 0.01–10 m, q_4 : 0.01–100 km, and q_5 : 100–500 km. Each slope is calculated as $q = (\log n(r_2) - \log n(r_1))/(\log r_2 - \log r_1)$, where r_1 (r_2) is the lower (upper) limit of the size range. For most calculations, the waviness in $R(r)$ is dominant at sizes, $r \approx 0.1$ – 100 km. Thus, the slopes q_1 , q_2 , and q_3 provide some measure of the shape of the fragmentation tail at small sizes. Similarly, the slope q_5 measures the impact of the cascade on the initial slope of $q = 5.5$ for $r \gtrsim 100$ km. At intermediate sizes, q_4 allows a comparison between the $q_s = -3$ to 3 and the final slope for $r \lesssim 100$ km.

The parameters r_v , r_p , and A_{pv} allow an evaluation of the waviness for each model. Systems with $A_{pv} \gtrsim 4$ – 5 have a significant waviness correlated with Q_s ; larger A_{pv} requires smaller Q_s . Comparison of r_v with r_t in Table 1 provides a separate evaluation of the size distribution: systems with $r_v \approx r_t$ have large q_s and less waviness. When Q_s is small, r_v is well off r_t ; the size distribution is then very wavy.

5.4. Applications to TNOs

To apply the results of collisional cascade calculations to the analysis of Singer et al. (2019), we focus on several basic features. In the *New Horizons* data, $R(r)$ is fairly flat at 1–20 km. From a well-defined peak at 1–2 km, the errors bars allow a shallow valley at 5–10 km. The last data point at ~ 15 km places few constraints on any model. For this exercise, we assume that the size distribution remains fairly flat from 10 km to 50–100 km and then matches the steep power-law with $q \approx 5.0$ – 5.5 for $r \gtrsim 100$ km derived from ground-based observations. Other options are possible, but this approach seems simplest. At the smallest sizes probed by *New Horizons*, 0.1–1 km, the factor of 10–20 drop in $R(r)$ is well-defined. We make no assumption about the behavior of $R(r)$ at $r \lesssim 0.1$ km.

Among the numerical calculations, several generate size distributions with the required features. Models

Table 3. Mass and Size Distribution Parameters at 4.5 Gyr^a

Model	r_l (km)	M/M_0	r_m (km)	q_1	q_2	q_3	q_4	q_5	r_v (km)	r_p (km)	A_{pv}
1	1.0	0.013	500	3.81	3.74	3.69	3.56	5.50	0.225	2.17	3.49
1	3.0	0.031	500	3.81	3.74	3.69	3.42	5.44	0.225	2.62	2.94
1	10.0	0.089	501	3.81	3.74	3.69	3.32	5.36	0.217	2.01	2.14
1	30.0	0.265	530	3.81	3.74	3.69	3.27	5.00	0.208	1.94	1.97
1	100.0	0.787	600	3.81	3.74	3.69	3.07	5.09	0.217	1.94	1.89
2	1.0	0.013	500	4.68	3.66	3.68	3.41	5.49	0.040	0.78	4.42
2	3.0	0.036	500	4.68	3.66	3.68	3.34	5.46	0.038	0.65	3.75
2	10.0	0.094	501	4.68	3.66	3.68	3.18	5.35	0.038	0.65	3.36
2	30.0	0.271	550	4.68	3.66	3.68	3.14	5.01	0.037	0.58	3.27
2	100.0	0.794	625	4.68	3.66	3.68	2.92	5.09	0.037	0.58	3.20
3	1.0	0.016	500	5.36	3.78	3.40	3.36	5.63	0.014	0.30	4.05
3	3.0	0.039	500	5.36	3.78	3.40	3.26	5.40	0.014	0.30	3.94
3	10.0	0.094	501	5.36	3.78	3.40	3.14	5.34	0.014	0.30	3.90
3	30.0	0.275	535	5.36	3.78	3.40	3.09	4.95	0.014	0.30	3.84
3	100.0	0.804	605	5.36	3.78	3.40	2.88	5.08	0.014	0.30	3.79
4	1.0	0.016	500	5.40	3.76	3.44	3.32	5.64	0.024	0.56	9.66
4	3.0	0.045	501	5.40	3.76	3.44	3.23	5.44	0.024	0.48	7.85
4	10.0	0.117	502	5.40	3.76	3.44	3.10	5.44	0.024	0.48	7.71
4	30.0	0.352	565	5.40	3.76	3.44	3.01	5.23	0.024	0.48	7.49
4	100.0	0.910	650	5.40	3.76	3.44	2.80	5.13	0.024	0.46	7.28
5	1.0	0.014	500	4.93	3.58	3.66	3.42	5.64	0.067	1.10	5.61
5	3.0	0.040	501	4.93	3.58	3.66	3.30	5.44	0.067	0.98	4.01
5	10.0	0.114	515	4.93	3.58	3.66	3.19	5.45	0.067	0.91	3.69
5	30.0	0.347	575	4.93	3.58	3.66	3.11	5.31	0.065	0.91	3.55
5	100.0	0.906	650	4.93	3.58	3.65	2.89	5.13	0.065	0.91	3.43
6	1.0	0.021	500	5.41	4.48	2.61	3.45	5.67	0.946	5.18	16.24
6	3.0	0.042	501	5.41	4.48	2.61	3.31	5.47	0.910	5.58	14.96
6	10.0	0.114	502	5.41	4.48	2.61	3.17	5.44	0.877	6.75	8.83
6	30.0	0.279	592	5.41	4.48	2.61	3.09	5.24	0.877	6.75	5.46
6	100.0	0.877	630	5.41	4.48	2.61	2.86	5.12	0.877	5.79	4.46
7	1.0	0.021	500	5.41	4.85	2.27	3.40	5.73	0.946	5.20	18.74
7	3.0	0.042	501	5.41	4.85	2.27	3.27	5.53	0.910	5.63	16.20
7	10.0	0.114	502	5.41	4.85	2.27	3.14	5.49	0.877	6.65	9.55
7	30.0	0.279	592	5.41	4.85	2.27	3.05	5.28	0.877	6.85	7.55
7	100.0	0.877	630	5.41	4.85	2.27	2.83	5.17	0.877	5.82	6.37
8	1.0	0.014	500	5.42	3.38	3.57	3.53	5.64	0.225	1.94	3.15
8	3.0	0.037	501	5.42	3.38	3.57	3.40	5.44	0.225	2.52	2.54
8	10.0	0.111	502	5.42	3.38	3.57	3.28	5.44	0.225	1.94	2.03
8	30.0	0.348	570	5.42	3.38	3.57	3.20	5.31	0.217	1.94	1.91
8	100.0	0.908	650	5.42	3.38	3.57	2.99	5.16	0.217	1.60	1.82
9	1.0	0.016	500	5.67	3.23	3.53	3.62	5.59	0.877	2.82	1.20
9	3.0	0.038	501	5.36	3.78	3.40	3.36	5.63	1.059	4.28	1.24
9	10.0	0.107	510	5.36	3.78	3.40	3.26	5.40	4.624	9.84	1.36
9	30.0	0.328	575	5.36	3.78	3.40	3.14	5.34	9.462	26.24	1.93
9	100.0	0.885	650	5.36	3.78	3.40	3.09	4.95	18.707	102.53	3.48
10	1.0	0.011	500	5.09	3.55	3.67	3.38	5.63	0.072	1.28	6.40
10	3.0	0.031	500	5.09	3.55	3.67	3.26	5.41	0.072	1.23	4.52
10	10.0	0.093	525	5.09	3.55	3.67	3.16	5.35	0.072	1.10	3.93
10	30.0	0.286	545	5.09	3.55	3.67	3.13	5.01	0.072	1.06	3.75
10	100.0	0.813	600	5.09	3.55	3.67	2.91	5.10	0.072	1.02	3.63
11	1.0	0.008	500	5.21	3.50	3.76	3.32	5.62	0.056	1.33	10.44
11	3.0	0.024	500	5.21	3.50	3.76	3.19	5.38	0.054	1.33	7.17
11	10.0	0.079	500	5.21	3.50	3.75	3.11	5.25	0.054	1.14	5.71
11	30.0	0.227	550	5.21	3.50	3.75	3.10	4.81	0.054	1.10	5.44
11	100.0	0.705	590	5.21	3.50	3.75	2.90	4.98	0.054	1.10	5.27

^aFor each model at 4.5 Gyr, the columns list r_l in km, the ratio of the final mass to the initial mass, r_m the radius of the largest object, the slopes q_1 , q_2 , q_3 , q_4 , q_5 as defined in the main text, r_v the position of the first valley near the transition radius, r_p the position of the first peak after the first valley, and $A_{pv} = R(r_p)/R(r_v)$.

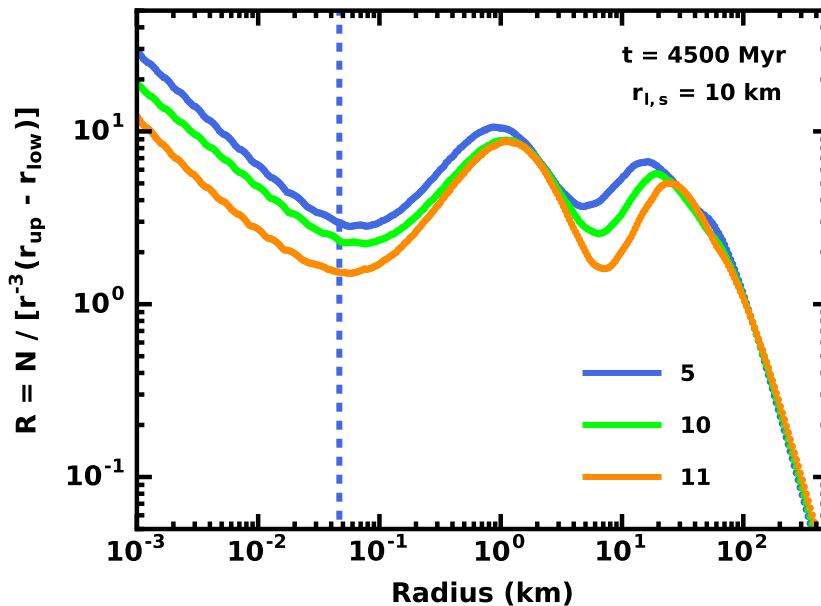


Fig. 23.— Comparison of $R(r)$ for $r_l = r_s = 10$ km at 4.5 Gyr for systems with normal ice and the Leinhardt & Stewart (2012) gravity component and collision velocities $v = 1$ km s $^{-1}$ (blue curve), 1.4 km s $^{-1}$ (green curve), and 2 km s $^{-1}$ (orange curve). Larger collision velocities eliminate the shoulder in the size distribution at 40–60 km. At smaller sizes, the amplitudes and wavelengths of peaks and valleys grow with larger v . However, the number of peaks/valleys and the overall shape of the size distribution is fairly independent of v .

(5), (10), and (11) display a clear peak near 1 km and a valley at 0.05 km (see Fig. 23) that agrees with the peak and valley in the *New Horizons* data. From the peak to the valley in $R(r)$, the amplitude listed in Table 3 grows from 3–6 ($v_c = 1$ km s $^{-1}$) to 4–7 ($v_c = 1.4$ km s $^{-1}$) to 5–7 ($v_c = 2$ km s $^{-1}$). While smaller than the amplitude in the *New Horizons* data, it seems plausible that a larger collision velocity might generate a larger amplitude. Systems with $r_l = 1$ –10 km have a deep valley at 5–10 km not observed in the *New Horizons* data. Calculations with $r_l = 30$ –100 km have a much shallower valley with a peak at 30–100 km that lies outside the range covered by *New Horizons*. With power-law slopes $q \approx 5$ at $r \gtrsim 30$ –100 km, the models provide a reasonable match to the ground-based data.

With a larger peak-to-valley amplitude, model (4) is also worth considering. For $v_c = 1$ km s $^{-1}$, the size distributions of the model (4) calculations are somewhat offset from those required for the *New Horizons* data, with peaks at 0.5 km and valleys at 0.025 km. While less well-placed than the peaks and valleys in models (5), (10), and (11), the amplitude of 7–9 is a better match to the *New Horizons* data. At larger sizes, however, the model (4) size distributions with $r_l = 30$ –100 km have a prominent valley at 3 km, a flat portion from 10–30 km, and a steep rise at 30–100 km (see Fig. 21). These do not match the *New Horizons* data very well.

To learn whether calculations with parameters intermediate between model (4) and model (5) provide a better match to the *New Horizons* data, we perform a limited set of calculations with the model (5) fragmentation parameters and substitute $Q_s = 10^6$ erg g $^{-1}$ cm $^{0.4}$. Starting with $r_l = r_s = 100$ km and q_s

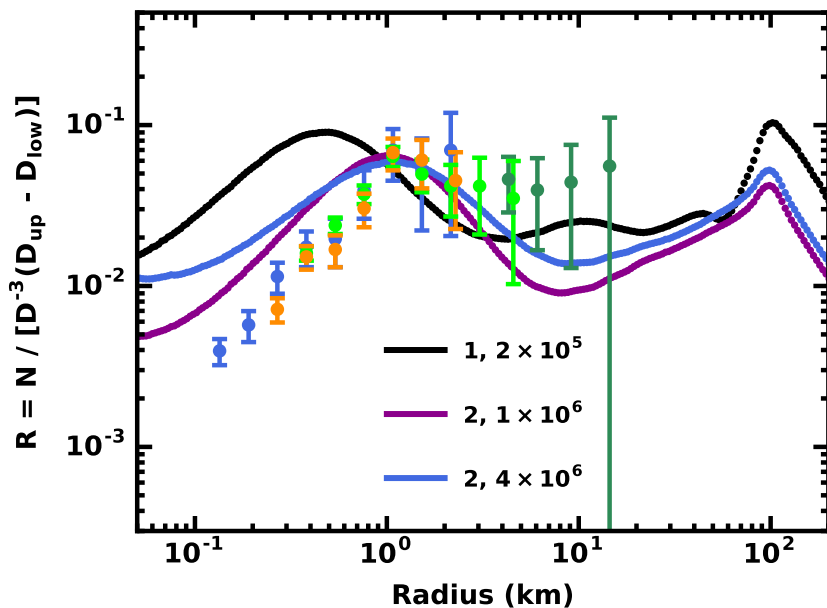


Fig. 24.— Comparison of *New Horizons* data with $R(r)$ for three collisional cascades. All calculations use $e_s = -0.4$ and the Leinhardt & Stewart (2012) parameters for the gravity component of Q_D^* . The legend indicates values for v_c (in km s^{-1}) and Q_s . Models with $v_c = 2 \text{ km s}^{-1}$ and $Q_s = 10^6 \text{ erg g}^{-1} \text{ cm}^{0.4}$ provide a reasonable match to the *New Horizons* data.

$= 0$, these calculations seek to establish whether a somewhat smaller bulk strength than in model (5) yields peaks and valleys close to those in model (5) but with a somewhat larger wave amplitude. Calculations with $v_c = 1 \text{ km s}^{-1}$, 2 km s^{-1} , and 3 km s^{-1} allow a measure of the wave amplitude as a function of v_c at this Q_s .

Fig. 24 compares several model size distributions with the *New Horizons* data. With the model (4) parameters (Fig. 24, black curve), the model matches the *New Horizons* data rather well at 1–20 km but fails at smaller sizes. Although the amplitude of the wave for model (4) is large, the location of the peak and valley are displaced to smaller sizes. Together with the normal ice fragmentation parameters, the larger collision velocity in model (11) matches the *New Horizons* data much better (Fig. 24, blue curve). Although this size distribution has a deep valley at 5–10 km, the agreement with the *New Horizons* data is reasonably good at 1–10 km. This model has a clear peak at 1 km, which agrees with the *New Horizons* data, and a valley at 0.05 km, which is consistent with the *New Horizons* data. However, the amplitude of the wave is a factor of 2–3 too small.

For $v_c = 2 \text{ km s}^{-1}$, models with $Q_s = 10^6 \text{ erg g}^{-1} \text{ cm}^{0.4}$ come close to matching the *New Horizons* data. At 1–100 km, this model has a peak at 1 km as in model (11), with a deeper valley at 5–10 km, and a gradual rise from 10 km to a sharp peak at 100 km. Solids with $r \gtrsim 100 \text{ km}$ have a steep size distribution with $q = 5$. Overall, this size distribution matches the *New Horizons* data well and has the steep slope at the largest sizes required by the ground-based observations. At smaller sizes, this model has a deep valley at 0.05 km. Unlike model (11), the depth of this valley almost matches the depth of the valley at 0.1 km in the *New Horizons* data.

In this model, with fragmentation parameters intermediate between those of the weak ice and normal ice parameters, changing the collision velocity does not improve the match to the observations. When $v_c = 1 \text{ km s}^{-1}$, the deep valley at 5–10 km is smaller; however, the valley at 0.05 km is also smaller. Thus, the lower collision velocity allows a better match to the data at 1–10 km at the expense of a poorer match at 0.1–1 km. Increasing the collision velocity to 3 km s^{-1} also fails to improve the match. At the higher collision velocities, the deep valley at 0.05 km remains fixed. Although the amplitude of the wave is somewhat larger, the peak is displaced to 2–3 km. In this size range, the match to the *New Horizons* data is somewhat better. The cost for this better match is a deeper valley at 5–10 km.

Compared to the analytical models, the χ^2 per degree of freedom for the numerical models is somewhat worse. The best analytical models have a χ^2 per degree of freedom of 3–4. In the numerical models, the χ^2 grows to 5–10. In both types of calculations, poor models have χ^2 per degree of freedom exceeding 100. While not excellent fits, the best analytical and numerical models are a significant improvement over other analytical and numerical models where the slope of the size distribution at 0.1–100 km is much larger than 3 (see the discussion in Greenstreet et al. 2015).

Overall, we prefer a model with $v_c = 2 \text{ km s}^{-1}$ and $Q_s = 10^6 \text{ erg g}^{-1} \text{ cm}^{0.4}$. Calculations with other initial values of q_s ($q_s = -3$ and 3 instead of $q_s = 0$) do not improve the match to the data. When $q_s = -3$, the valley at 5–10 km is deeper compared to the model with $q_s = 0$. At low collision velocities, $v_c = 1 \text{ km s}^{-1}$, models with $q_s = 3$ have much shallower valleys at 5–10 km than models with smaller q_s . Increasing v_c to $2\text{--}3 \text{ km s}^{-1}$ tends to eliminate this difference. Thus, systems with $v_c = 2\text{--}3 \text{ km s}^{-1}$ and $q_s = 2\text{--}3$ have size distributions similar to those with $q_s = 0$.

6. DISCUSSION

The analytic and numerical calculations described in §4 and §5 demonstrate that collisional cascades produce size distributions with features similar to those observed in the *New Horizons* data for Charon impactors with $r \approx 0.1\text{--}10 \text{ km}$. In the analytic models, reasonably good matches to the *New Horizons* data are possible when Q_s is small ($\sim 10^4 \text{ erg g}^{-1} \text{ cm}^{0.4}$) or moderate ($\sim 4 \times 10^6 \text{ erg g}^{-1} \text{ cm}^{0.4}$). Values for Q_s in between these limits produce size distributions that disagree with the *New Horizons* data. Much larger values for Q_s also fail. The analytic models favor smaller values for the exponent of the bulk strength component of Q_D^* ($e_s \approx -0.2$ to -0.4). When e_s is larger, the waves in the size distribution are too small. Our analysis supports the Leinhardt & Stewart (2012) parameters for the gravity component of Q_D^* over the Benz & Asphaug (1999) parameters.

The numerical models strongly favor the normal ice fragmentation parameters. When Q_s is small, the amplitudes of the waves in the size distribution are comparable to the factor of 10–20 wave observed in the *New Horizons* size distribution. However, the peaks and valleys in the numerical simulations are well off those in the data. When the calculations use parameters for normal ice ($Q_s \sim 1\text{--}4 \times 10^6 \text{ erg g}^{-1} \text{ cm}^{0.4}$ and $e_s = -0.4$), the locations of peaks and valleys match those in the *New Horizons* data. For collision velocities $v_c = 2 \text{ km s}^{-1}$, the amplitude of the wave falls about a factor of two short of the amplitude observed in the *New Horizons* data. Changing the collision velocity does not change the amplitude of the wave significantly; larger v_c moves the peak away from the peak in the *New Horizons* data. Although the match to the *New Horizons* data is not perfect, the derived size distributions match much better than other results in the literature.

Comparison of Fig. 6 and Fig. 24 suggest the analytical models match the *New Horizons* data better

than the numerical models. Due to the cpu time required, the numerical models sample a smaller set of fragmentation parameters than the analytical models. Because the numerical models do not match the analytical models precisely (see Figs. 18–19), it is not possible to anticipate the shape of the final size distribution in any numerical model. Choosing a fragmentation model slightly different than ‘normal ice’ might yield a better match to the *New Horizons* data. Within the numerical calculations, shot noise among large objects with infrequent collisions and the redistribution of mass from cratering and catastrophic collisions appear to reduce the waviness of the size distribution somewhat relative to the analytical model. With the fragmentation parameters required to match the *New Horizons* data fairly well-constrained, it is possible to examine how the degree of waviness depends on other algorithms in the numerical model. We plan to consider this issue in a future study.

Despite the sensitivity to the fragmentation parameters, the shapes of the wavy size distributions are remarkably insensitive to initial conditions. After 100–200 Myr of collisional evolution at 45 au, there is little variation in $R(r)$ at 0.1–10 km among calculations with different r_l and q_s . When Q_s is fairly large, all $R(r)$ have a valley near the transition radius and a peak at 10–30 r_t ; the position of the peak and the valley agree well with analytic models (O’Brien & Greenberg 2003). Systems with smaller Q_s have a valley at a size r_v somewhat larger than r_t and a peak $r_p \sim 10\text{--}30 r_v$; these peaks/valleys lie off analytic predictions due to interactions with waves generated by the small-size cutoff at 1 μm . At 10–100 km, $R(r)$ is sensitive to r_l and q_s . As the evolution proceeds past 100–200 Myr, these differences often disappear.

Tests indicate that $R(r)$ is also insensitive to the fragmentation algorithm. Calculations with different values for $m_{l,0}$, b_l , and b_d have similar size distributions at $t \gtrsim 100\text{--}200$ Myr. Although we did not test alternative approaches for catastrophic disruption or cratering (e.g., Fraser 2009; Benavidez & Campo Bagatin 2009; Campo Bagatin & Benavidez 2012, and references therein), previous experience with other fragmentation algorithms suggests that results will be similar to those described above (e.g., Kenyon & Bromley 2002, 2004a,b, 2008). While calculations with other approaches may infer somewhat different ‘best’ parameters for matches to the *New Horizons* data, the general conclusion that solids composed of ‘normal ice’ provide a better match to the positions of peaks and valleys in the *New Horizons* data than ‘strong’, ‘weak’, or ‘very weak’ ice should be independent of the fragmentation algorithm.

Another set of tests suggest that the evolution is independent of the algorithm for velocity evolution. In all models described above, particles have initial e and i that are fixed throughout the calculation. Allowing collisional damping, dynamical friction, and viscous stirring to modify particle velocities has little impact. The cascade is too efficient at transporting material from large particles to small particles. We did not investigate the possibility that large and small particles have different initial e and i ; however, we doubt that the results would be much different from those described above.

The calculations that most closely match the *New Horizons* data also provide a good match to other observations of TNOs. By design, the calculations begin with a steep size distribution, $q \approx 5.5$ for $r \gtrsim 100$ km. After 4.5 Gyr of evolution, the final slope is somewhat shallower, $q \approx 5$. Starting with a steeper slope, $q \approx 6$, instead of $q \approx 5.5$ would result in a final slope close to the observed $q \approx 5.5$ with little impact on the shape of the size distribution at smaller sizes. In simulations with $r_l \approx 30\text{--}100$ km, the size distribution has a clear break in slope at $r_b \approx 50\text{--}100$ km, close to the break inferred from ground-based and space-based imaging data. Some of the calculations also generate a divot in the size distribution for objects with $r \lesssim r_b$. The magnitude of the divot in the calculations is comparable to that required in some surveys of TNOs (e.g., Shankman et al. 2013, 2016; Alexandersen et al. 2016; Lawler et al. 2018).

Among the full suite of calculations, the power-law slope of the size distribution at 10–100 km, $q \approx 1.5\text{--}$

3.5, includes the range derived from ground-based observations of TNOs, $q \approx 2.0\text{--}3.5$ (see Fig. 1). Systems with $r_l = 1\text{--}3$ km generate the steepest slopes at $t \gtrsim 100\text{--}200$ Myr, $q \approx 3.0\text{--}3.5$, and have a break in the size distribution at smaller radii than observed, $r_b \approx 10\text{--}30$ km. As we increase r_l , the slope at 10–100 km decreases to $q \approx 2\text{--}2.5$; the position of the break grows to 50–100 km as observed. Some calculations with $r_l \gtrsim 10$ km generate two breaks in $n(r)$, one at 50–100 km and another at 10–30 km. In these systems, $q \approx 3.5$ (3.0) at $r \approx 10\text{--}30$ km ($r \lesssim 10\text{--}20$ km).

Although results from the analytic model suggest that the placement of waves at 0.1–10 km depends on r_{min} , we fixed $r_{min} = 1 \mu\text{m}$ in the suite of numerical calculations. For the normal and strong ice parameters, r_{min} should have little impact on the shape of $R(r)$. However, it is plausible that a factor of 2–3 smaller/larger r_{min} could impact the positions of waves in calculations with the weak ice fragmentation parameters. Shifting the positions of valleys and peaks in the size distributions of weak ice calculations to factor of 2–3 larger sizes would enable a better match to the *New Horizons* data. We plan to consider the impact of different choices for r_{min} and r_{max} in a separate publication.

In the calculations discussed here, expanding to a multi-annulus grid might produce a somewhat different outcome. In a multi-annulus calculation, the size distribution of solids in each annulus depends on the mix of collisions from material in other annuli. In a system where we divide the 30–60 au annulus considered here into 8–16 separate annuli with identical orbital e and i , annuli closer to the Sun experience higher velocity collisions than more distant annuli. With no excitation from nearby gas giants, we expect the average size distribution of the swarm to be similar to the results of single annulus calculations.

6.1. Dynamical Evolution of the Solar System

In current models for the Solar System, the gas giants grow within a circumsolar gaseous disk and reach their final masses before the disk dissipates $\sim 5\text{--}10$ Myr after the Sun formed (e.g., Bromley & Kenyon 2011; Mordasini et al. 2015; Johansen & Lambrechts 2017; Chambers 2018; Bitsch et al. 2019, and references therein). To account for the orbital architecture of the trans-Neptunian region and other features of the Solar System, dynamical calculations require Uranus and Neptune to migrate outward through a remnant disk of solid material to reach their current orbits (e.g., Malhotra 1993, 1995; Levison & Morbidelli 2003; Levison et al. 2008; Nesvorný 2015; Nesvorný & Vokrouhlický 2016). Viable migration models require proper timing of the migration and specific constraints on the size distribution of solids within the remnant disk. To avoid a collisional cascade removing significant material on short time scales, most of the mass in solids is in large objects with $r \gtrsim 100$ km (e.g., Kenyon et al. 2008; Kenyon & Bromley 2010). Achieving the observed mix of resonant and non-resonant objects requires migration through a swarm of Plutos on time scales of 10–100 Myr (e.g., Nesvorný 2015; Nesvorný & Vokrouhlický 2016); otherwise, it is not possible to generate the correct mix of resonant and non-resonant TNOs with the observed distribution of eccentricity and inclination.

To place the present calculations in the context of this evolution, we rely on previous results for the growth of solids at 15–150 au (e.g., Kenyon & Bromley 2008, 2010, 2012). Among any swarm of solids, the time scale for the size distribution to evolve scales with the local surface density Σ and orbital period P as $t \propto P/\Sigma$ (see also Lissauer 1987; Goldreich et al. 2004; Youdin & Kenyon 2013). Although the evolution of the collisional cascades described in this paper depends on r_l and the fragmentation parameters, most calculations establish the main features of the final size distribution at 100–300 Myr. For any other

combination of starting conditions, the time scale to achieve an approximate equilibrium size distribution is

$$t_{eq} \approx 200 \text{ Myr} \left(\frac{a}{45 \text{ au}} \right)^{3/2} \left(\frac{0.15 \text{ g cm}^{-2}}{\Sigma} \right). \quad (27)$$

Within the single annulus extending from 30 au to 60 au, $\Sigma = 0.15 \text{ g cm}^{-2}$ yields a total mass in solids of $45 M_{\oplus}$. For each calculation, the shape of the size distribution is nearly constant in time for $t \gtrsim t_{eq}$; the total mass in the swarm steadily declines with time.

For the initial conditions considered here, the time scale to generate the required features in the size distribution is a factor of 2–3 longer than the current estimate for the migration time of Neptune, $\lesssim 100 \text{ Myr}$ (Nesvorný & Vokrouhlický 2016). However, several modifications to the starting conditions yield similar size distributions on shorter time scales. At 45 au, increasing the initial surface density by a factor of five shortens the time required to reach equilibrium by a similar factor. To avoid increasing the initial mass to an unpalatable $225 M_{\oplus}$, it is necessary to reduce the size of the annulus from 30–60 au to 42–48 au. Shrinking the annulus further provides a way to maintain the same surface density (and collision time scale) while reducing the mass below $45 M_{\oplus}$.

Although confining solids to a narrow annulus is an unconventional choice for models of the Solar System, recent high resolution observations of many protostellar disks with ALMA reveal a variety of narrow rings at 25–100 au from the central star (e.g., Zhang et al. 2016; Fedele et al. 2018; Dullemond et al. 2018; Huang et al. 2018; Long et al. 2018; Cieza et al. 2019; Long et al. 2020). Among pre-main sequence stars with large disks, rings are common. Although young stars with compact disks are difficult to resolve with ALMA, Long et al. (2020) show evidence for structure on small scales, $a \sim 10\text{--}20 \text{ au}$ in GQ Lup A. The physical properties of the dusty rings in young stars are similar to those required to generate a suitably wavy size distribution of 0.1 km and larger TNOs in less than 100 Myr. Thus, this option is a plausible way to build a TNO size distribution that matches the *New Horizons* data on a time scale consistent with Neptune migration.

Placing the solids at smaller a is a viable alternative to a narrow ring at 45 au. Setting $a \approx 25 \text{ au}$ and keeping the surface density fixed at $\Sigma \approx 0.15 \text{ g cm}^{-2}$, the time scale to produce a wavy size distribution that closely matches the *New Horizons* data is $\sim 70 \text{ Myr}$. For the protosolar nebula model required to build the giant planets at 5–15 au, the surface density is $\Sigma \approx 0.5 \text{ g cm}^{-2}$ at 25 au (e.g., Bromley & Kenyon 2011; Kenyon & Bromley 2012). If this material extends from 20 au to 30 au, the total mass is roughly $30 M_{\oplus}$. The evolution time is $\sim 25 \text{ Myr}$. While the mass is somewhat larger than the $\sim 20 M_{\oplus}$ required in the Nesvorný & Vokrouhlický (2016) migration model, the time scale to generate a wavy size distribution is much smaller than the 50–100 Myr migration time. In this scenario, a migrating Neptune places many TNOs in resonant orbits. Our calculations suggest these TNOs would have a wavy size distribution similar to the size distribution of Charon impactors.

In either model for the size distribution of TNOs, dynamical interactions with Neptune need to remove most of the mass (Levison & Morbidelli 2003; Kenyon et al. 2008; Nesvorný & Vokrouhlický 2016). In our calculations, $R(r)$ achieves a characteristic shape with little total mass loss. Once the solids have this shape, destructive collisions slowly reduce the total mass. In the Solar System, where Neptune migrates outward from $\sim 15\text{--}20 \text{ au}$ to 30 au, dynamical interactions with the planet eject mass from the vicinity of Neptune; subsequent interactions with Neptune and the other gas giants eventually eject this mass from the Solar System. If collisional processes at 20–30 au have time to generate the characteristic shape for the size distribution, dynamical processes can remove mass without changing the shape of the size distribution. Our analysis suggests that collisions at 20–30 au can generate the required shape. Testing this conclusion in more detail requires a collisional cascade calculation coupled to a migration simulation.

Removing material in a narrow ring outside of Neptune’s orbit is more challenging. Once Neptune reaches its current orbit at $a \approx 30$ au, it rapidly removes solids material at 30–36 au and sculpts the orbits of solids at $a \gtrsim 36$ au. The time scale to remove tens of Earth masses outside of 36 au depends on the position of the ring relative to Neptune’s orbit and the eccentricities and inclinations of solids within the ring. It seems plausible that a collisional cascade can generate the necessary size distribution of TNOs as Neptune migrates to its current orbit. Quantifying the ability of Neptune to reduce the mass of solids to the level observed now requires coupling the collision calculation to a dynamical calculation involving Neptune and the other gas giants.

6.2. Long-term Evolution of Charon Impactors

As summarized in Singer et al. (2019), the craters on Charon represent the integrated history of impacts over the lifetime of the Pluto–Charon system. After Pluto–Charon forms (e.g., Canup 2005, 2011; Kenyon & Bromley 2014; Desch 2015; Kenyon & Bromley 2019), impacts from TNOs and any material leftover from the formation of the small satellites (e.g, Walsh & Levison 2015; Bromley & Kenyon 2020) generate craters on the surface of each planet. Reconstructing the cratering history requires time-dependent models for the size distribution(s), orbital architecture(s), and impact rates of possible impactors. Combining these with a relation between the sizes of the impactor and its associated crater yields a size-frequency distribution of craters on the surface of Charon.

If the size distributions and the orbital architectures of TNOs are constant in time, analytic and semi-analytical prescriptions for the collision rates are sufficient to derive the impact history (e.g., Dell’Oro et al. 2013; Greenstreet et al. 2015; Bierhaus & Dones 2015). In this approach, the size distribution of the craters reflects the adopted size distributions of TNOs. Greenstreet et al. (2015) consider a broad range of size distributions derived from (i) power-law fits to ground-based TNO data (see §2) and (ii) numerical simulations (e.g., Schlichting et al. 2013). Bierhaus & Dones (2015) consider power-law size distributions with $q = 2$ or 3 . In both studies, the predicted diameter of Charon’s largest crater (equivalently, the diameter of the largest impactor) is set by the total mass in TNOs and the fraction of TNO orbits that cross the orbit of Pluto–Charon. Below this size, the $R(r)$ for impactors is identical to the adopted size distribution.

To derive the expected crater distribution on Charon from a collisional cascade, we need to combine the calculations considered here with a dynamical model for the evolution of (i) TNO orbits with time and (ii) the removal rate due to interactions with Neptune. Here, we consider several simple estimates for TNOs with $a \gtrsim 30$ au to set the stage for a more detailed treatment in a future study. We assume that the TNOs generated at 20–30 au and placed onto larger a orbits by Neptune have the space density and orbital architecture required to match current observations. Because the collisional cascade calculations generate a wavy size distribution on short time scales, all of the different dynamical classes of TNOs have the same wavy size distribution. Of the calculations considered here, those with the normal ice or weak ice fragmentation parameters have the best chance of matching the size distribution of Charon impactors.

For the broad annulus at 30–60 au, only a fraction of the solids might collide with Pluto. Neptune removes all solids inside 36 au. TNOs with $q \gtrsim 50$ au never intersect Pluto’s orbit; At aphelion, Pluto has a large height above the ecliptic plane. TNOs with $a \approx 50$ au and lower e , lower inclination orbits also cannot collide with Pluto. Together, these constraints remove nearly 90% of the solids in the calculation from further consideration. To estimate the impact probability, we scale the number of TNOs with $H \leq 9$ ($r \gtrsim 40$ km) remaining in a calculation at 100–200 Myr to the results in Table 1 of Greenstreet et al. (2015)

and derive approximate rates for collisions with Pluto. Rates for Charon follow from the ratio of surface areas, with $r_C/r_P = 0.26$ (Stern et al. 2015; Nimmo et al. 2017).

Among the full suite of cascade calculations discussed here, the impact rates at 100–200 Myr range from a few to 100 times the rates quoted in Greenstreet et al. (2015). Models with the smallest rate of impacts have most of the initial mass in 1–3 km planetesimals. Within 100–200 Myr, collisions convert 90% to 95% of the initial mass into debris with $r \lesssim 0.1$ km. When most of the mass is initially in 30–100 km objects, collisions take much longer to remove a significant amount of material from the swarm. These models retain most of their mass until 300–500 Myr.

For solids in a narrow annulus, the impact rate depends mainly on the location of the annulus. Because collision rates within the annulus are large, the mass declines rapidly, on time scales of 20–100 Myr instead of 100–500 Myr for systems with $r_l = 1$ –100 km. These loss rates limit the number of impacts onto Pluto–Charon. In an annulus at 38–42 au, most of the solids can interact with Pluto; however, Neptune dynamically removes objects not lost to the collisional cascade. Although moving the annulus to 48–52 au limits removal by Neptune, the orbits of many fewer TNOs cross the orbit of Pluto–Charon. We suspect that it is possible to find a model where the size distribution at 20–30 Myr roughly matches the *New Horizons* observations and has the mass required to generate the observed cratering rate. Compared to other options, this approach requires more fine tuning of the initial conditions.

Overall, it seems that impactors generated in a collisional cascade could explain the *New Horizons* observations. Many calculations develop the required wavy size distributions in 20–30 Myr (for a narrow annulus at ~ 45 au or a disk at 20–30 au) to 100–200 Myr (for a broad annulus at 30–60 au). Although the total mass in solids continues to decline after these epochs, the shapes of these size distributions are relatively invariant over the rest of the age of the Solar System. Placing better constraints on the ability of models to match the density of craters on Charon requires calculations that track the dynamical interactions of TNOs with Neptune and the time-varying impact rate onto Pluto–Charon. Although straightforward within the *Orchestra* code, these calculations are time-consuming. Together with the relative insensitivity of the calculations to the initial q_s , the success of ruling out solids with strong ice or very weak ice allows the next set of calculations to be more focused.

Aside from matching the density and the size distribution of craters on Charon, it is important to match the current space density of the various dynamical classes of TNOs. Of the options considered here, it is easiest to imagine that an initial disk of solids at 20–30 au can maintain a cascade that achieves all of the goals of a complete TNO model. A well-placed narrow annulus outside the orbit of Neptune is the next most likely option. Developing a successful model with a thick annulus at 30–60 au is a challenge. More comprehensive numerical calculations can test these conclusions.

6.3. Impactors on (486958) Arrokoth

As we completed the calculations for this study, Spencer et al. (2020) reported an extensive analysis of the *New Horizons* data acquired during the 2019 January flyby of the TNO (486958) Arrokoth. Aside from revealing a lack of small rings and small satellites in the system, they describe statistics of the cratering record. For diameters 0.3–1 km, the frequency of craters follows a power-law with a slope, $q \approx -2$, that is indistinguishable from the frequency distribution of small craters with diameter 1–20 km on Charon (Singer et al. 2019). The density of 0.8–1 km craters on Arrokoth is roughly an order of magnitude larger than the density of 1–2 km craters on Charon, more than the factor of ~ 2 expected from detailed calculations of the

impact frequency prior to the flyby (Greenstreet et al. 2019).

To compare the collisional cascade calculations with these *New Horizons* data, we ignore the difference in absolute crater frequencies between Arrokoth and Charon and focus on the shape of the frequency distribution. We also gloss over the impact of the trajectories and velocities of impactors and the porosity and other physical characteristics of ices on the relation between impactor size and crater diameter (e.g., Bierhaus & Dones 2015; Singer et al. 2019). For simplicity, we adopt the same scaling relation between impactor size and crater diameter, $D = D_c/6.25$, used in §2. Other options yield similar results (e.g, Greenstreet et al. 2019).

For the adopted scaling relation, it is challenging to find a cascade model capable of matching the combined set of Arrokoth–Charon cratering data. Within the *New Horizons* data, the combined power-law slope extends over nearly two orders of magnitude in crater diameter. If both sets of craters have the same relation between crater diameter and impactor size, a cascade model needs to generate a power-law with slope $q \approx -2$ from 1 km to 0.04–0.05 km. For the normal ice parameters, $R(r)$ has a maximum at 1 km and a minimum at 0.05 km; however, the amplitude from peak to trough is much smaller than observed in the combined *New Horizons* data set (see Figs. 21, 22, and 24. With the weak ice parameters, the amplitude is larger but the maxima and minima are displaced to smaller sizes compared to the data. All calculations with very weak ice have wave amplitudes large enough to match the combined *New Horizons* data. However, these cascades produce minima at 1 km and maxima at 0.05 km.

Assuming the adopted scaling between crater and impactor sizes is correct, cascade calculations with very weak ice and a different r_{min} might match the combined *New Horizons* data. In the analytical models, shifting the minimum size in the calculation from $r_{min} = 0.3 \mu\text{m}$ to $r_{min} = 3 \mu\text{m}$ resulted in a significant shift in the positions of peaks and valleys in $R(r)$ at 0.1–1 km for the very weak ice fragmentation parameters (see Fig. 6). If the numerical calculations with different r_{min} generate similar shifts in the positions of peaks and valleys, then it should be possible to match the *New Horizons* observations with the very weak ice fragmentation parameters.

Matching the *New Horizons* data with the very weak ice parameters would have interesting implications for the long-term evolution of the TNO space density and cratering rate. When the cascade begins with a significant mass in small objects, $r \lesssim 1\text{--}10$ km, swarms of solids with the very weak ice fragmentation parameters lose mass more rapidly than those with the stronger ice parameters. Thus, it is easier for swarms with the very weak ice parameters to lose enough mass to match the current space density of TNOs at 40–50 au. More rapid mass loss also lowers the rate of TNO impacts on other TNOs, enabling the cascade models to provide a better match to the impact rates on Pluto, Charon, Arrokoth, and (eventually) other TNOs.

6.4. Other Issues

In §2, we noted the limited constraints on the frequency of ~ 1 km TNOs from space-based occultation data (e.g., Schlichting et al. 2009; Bianco et al. 2010; Schlichting et al. 2012; Zhang et al. 2013; Liu et al. 2015) and the need to convert small TNOs into Jupiter family comets (e.g., Levison & Duncan 1997; Emel’yanenko et al. 2004; Volk & Malhotra 2008; Brassier & Wang 2015, and references therein). In both examples, the apparent number of 1 km TNOs implies a very steep power-law size distribution at 1–100 km with $q \approx 3.5\text{--}3.75$. The *New Horizons* data for craters on Charon have $q \approx 3$ at 1–10 km and $q \approx 2$ at 0.1–1 km. There are few good options to reconcile these differences. Normalizing the *New Horizons* counts at 1 km to

level required for Jupiter family comets and the occultation data yields too many 10 km TNOs.

Our calculations do not address this issue. It seems plausible that the source of the impactors on Charon differs from the source of Jupiter family comets, especially if TNOs are formed in different locations from ~ 20 au to ~ 50 au. Developing this idea in more detail requires a multi-annulus coagulation–dynamical calculation to follow the evolution of the dynamics and the size distribution of TNOs at multiple points in the Solar System.

More complicated analyses of the space-based occultation data and ground-based TNO surveys might also address the offset in number density relative to the *New Horizons* data. For both data sets, analyses adopt power-law size distributions for TNOs with $r \lesssim 100$ km. Repeating these analyses with wavy size distributions might provide some insight. Given the good general agreement between the analytical and numerical calculations, it should be straightforward to incorporate our method for generating an equilibrium size distribution into these analyses. In principle, these data sets might place constraints on the fragmentation parameters needed to derive an equilibrium size distribution. Evaluating these constraints together with the limits from *New Horizons* data might yield additional information on the bulk properties of TNOs.

Finally, the size distribution of Charon impactors has features in common with the size distributions of Jupiter’s Trojan satellites and the main belt asteroids (e.g., Bottke et al. 2005; Yoshida & Nakamura 2005, 2008; Bottke et al. 2015; Yoshida & Terai 2017; Singer et al. 2019; Yoshida et al. 2019). In these other systems, $R(r)$ has a deep valley at $r_v \lesssim 0.1$ km and a peak at $r_p \approx 5$ km. Although we do not attempt to match $R(r)$ for asteroids or Jupiter’s Trojans, collisional cascades with $r_l \approx 5$ km and a range of fragmentation parameters can produce a peak in $R(r)$ at 5 km. Matching the deep valley probably requires solids composed of weak or normal ice rather than strong ice.

7. SUMMARY

The analytic and numerical calculations described here demonstrate that collisional cascades of 1–500 km icy solids generate wavy size distributions with features similar to those inferred from counts of craters on Charon. For models with a standard prescription for the binding energy Q_D^* (eq. 10) and an energy-scaling algorithm for collision outcomes, calculations that provide the best match to the *New Horizons* data have the properties of normal ice. In swarms of strong ice solids, features in the size distribution do not match the amplitudes or positions of peaks and valleys in the *New Horizons* data. Calculations of weak ice solids have the correct amplitudes for waves but not the correct positions of peaks and valleys.

Aside from matching the *New Horizons* data, cascades can also maintain a steep size distribution for solids with $r \gtrsim 100$ km and a break in the size distribution at $r_b \approx 50$ –100 km. Some calculations also produce a divot in the size distribution of solids with $r \lesssim r_b$. Additional work is needed to learn whether the size distributions that match the *New Horizons* data can account for the frequency of Jupiter family comets and recent detections of small TNOs with occultations.

Adding *New Horizons* data on the cratering record of (486958) Arrokoth complicates this analysis. For the combined set of Arrokoth and Charon impactors, the normal ice calculations have a wave maximum that matches the change in slope of $R(r)$ at 10–20 km and; the wave minimum is close to the smallest crater detected on Arrokoth. However, the wave amplitude from peak to trough is a factor of 3–4 smaller in the model than in the data. Although calculations with very weak ice produce waves with roughly the required amplitude at 0.05–1 km, the models have a wave maximum (minimum) at the trough (peak) of the data.

We speculate that calculations with a different minimum radius for solids might shift wave position without modifying the wave amplitude. We plan to test this possibility in a future study.

Although we perform calculations for one fixed annulus at 30–60 au from the Sun, scaling relations developed from previous studies allow us to consider whether the cascade models are consistent with the dynamical evolution of the gas giant planets and the cratering record on Pluto–Charon. In rings of solids at 20–30 au where Neptune migrates to its current orbit on time scales of 50–100 Myr (e.g., Nesvorný & Vokrouhlický 2016), collisional evolution can produce a wavy size distribution with features similar to the size distribution on Charon in 20–30 Myr. This model may also yield a reasonable cratering rate on Charon. Outside Neptune’s orbit, evolution of a swarm of solids at 30–60 au seems unlikely to produce a small enough cratering rate. However, cascades in a narrow annulus at 42–48 au are a viable alternative.

Making progress on a complete model for the size distribution of TNOs requires a calculation that combines a collision model with a dynamical model to derive the time evolution of the space density and orbital parameters of TNOs as functions of time. Aside from providing better comparisons with data for the wavy size distribution of craters on Charon and Arrokoth, this model can also derive cratering rates for comparisons with *New Horizons* data. With similarly wavy size distributions observed in main belt asteroids and Jupiter’s Trojan satellites (Bierhaus & Dones 2015; Bottke et al. 2015; Yoshida et al. 2019), it seems plausible that collisional cascades among solids left over from the formation of the terrestrial planets and the gas giants play an important role in establishing the current properties of small objects throughout the Solar System.

We acknowledge generous allotments of computer time on the NASA ‘discover’ cluster. Advice and comments from W. Fraser, M. Geller, and two reviewers greatly improved our presentation. Portions of this project were supported by the *NASA Outer Planets* and *Emerging Worlds* programs through grants NNX11AM37G and NNX17AE24G. This research has made use of data and/or services provided by the International Astronomical Union’s Minor Planet Center.

REFERENCES

- Adams, E. R., Gulbis, A. A. S., Elliot, J. L., et al. 2014, *AJ*, 148, 55
- Alexandersen, M., Gladman, B., Kavelaars, J. J., et al. 2016, *AJ*, 152, 111
- Artymowicz, P. 1988, *ApJ*, 335, L79
- Asphaug, E., & Benz, W. 1996, *Icarus*, 121, 225
- Bannister, M. T., Alexandersen, M., Benecchi, S. D., et al. 2016a, *AJ*, 152, 212
- Bannister, M. T., Kavelaars, J. J., Petit, J.-M., et al. 2016b, *AJ*, 152, 70
- Bannister, M. T., Gladman, B. J., Kavelaars, J. J., et al. 2018, *ApJS*, 236, 18
- Benavidez, P. G., & Campo Bagatin, A. 2009, *Planet. Space Sci.*, 57, 201
- Benz, W., & Asphaug, E. 1999, *Icarus*, 142, 5
- Bernardinelli, P. H., Bernstein, G. M., Sako, M., et al. 2020, *ApJS*, 247, 32

- Bernstein, G. M., Trilling, D. E., Allen, R. L., et al. 2004, *AJ*, 128, 1364
- Bianco, F. B., Zhang, Z.-W., Lehner, M. J., et al. 2010, *AJ*, 139, 1499
- Bierhaus, E. B., & Dones, L. 2015, *Icarus*, 246, 165
- Bitsch, B., Izidoro, A., Johansen, A., et al. 2019, *A&A*, 623, A88
- Bottke, W. F., Broz, M., O’Brien, D. P., et al. 2015, *The Collisional Evolution of the Main Asteroid Belt*, 701–724
- Bottke, W. F., Durda, D. D., Nesvorný, D., et al. 2005, *Icarus*, 175, 111
- Brasser, R., & Wang, J. H. 2015, *A&A*, 573, A102
- Bromley, B. C., & Kenyon, S. J. 2006, *AJ*, 131, 2737
- . 2011, *ApJ*, 731, 101
- . 2013, *ApJ*, 764, 192
- . 2020, arXiv e-prints, arXiv:2006.13901
- Brown, M. E., & Schaller, E. L. 2007, *Science*, 316, 1585
- Brown, M. E., Trujillo, C., & Rabinowitz, D. 2004, *ApJ*, 617, 645
- Burns, J. A., Lamy, P. L., & Soter, S. 1979, *Icarus*, 40, 1
- Campo Bagatin, A., & Benavidez, P. G. 2012, *MNRAS*, 423, 1254
- Campo Bagatin, A., Cellino, A., Davis, D. R., Farinella, P., & Paolicchi, P. 1994, *Planet. Space Sci.*, 42, 1079
- Canup, R. M. 2005, *Science*, 307, 546
- . 2011, *AJ*, 141, 35
- Chambers, J. 2018, *ApJ*, 865, 30
- Charnoz, S., & Morbidelli, A. 2007, *Icarus*, 188, 468
- Chiang, E. I., & Brown, M. E. 1999, *AJ*, 118, 1411
- Chiang, E. I., Lovering, J. R., Millis, R. L., et al. 2003a, *Earth Moon and Planets*, 92, 49
- Chiang, E. I., Jordan, A. B., Millis, R. L., et al. 2003b, *AJ*, 126, 430
- Cieza, L. A., Ruíz-Rodríguez, D., Hales, A., et al. 2019, *MNRAS*, 482, 698
- Davis, D. R., Chapman, C. R., Weidenschilling, S. J., & Greenberg, R. 1985, *Icarus*, 63, 30
- Davis, D. R., & Farinella, P. 1997, *Icarus*, 125, 50
- Dell’Oro, A., Campo Bagatin, A., Benavidez, P. G., & Alemañ, R. A. 2013, *A&A*, 558, A95

- Delsanti, A., & Jewitt, D. 2006, in *Solar System Update*, ed. P. Blondel & J. W. Mason (Berlin: Springer), 267
- Desch, S. J. 2015, *Icarus*, 246, 37
- Di Sisto, R. P., Fernández, J. A., & Brunini, A. 2009, *Icarus*, 203, 140
- Dohnanyi, J. S. 1969, *J. Geophys. Res.*, 74, 2531
- Dominik, C., & Decin, G. 2003, *ApJ*, 598, 626
- Dones, L., Weissman, P. R., Levison, H. F., & Duncan, M. J. 2004, in *Comets II*, ed. M. C. Festou, H. U. Keller, & H. A. Weaver (Tucson: University of Arizona Press), 153
- Duffard, R., Pinilla-Alonso, N., Santos-Sanz, P., et al. 2014, *A&A*, 564, A92
- Dullemond, C. P., Birnstiel, T., Huang, J., et al. 2018, *ApJ*, 869, L46
- Duncan, M. J., & Levison, H. F. 1997, *Science*, 276, 1670
- Durda, D. D., Greenberg, R., & Jedicke, R. 1998, *Icarus*, 135, 431
- Durda, D. D., & Stern, S. A. 2000, *Icarus*, 145, 220
- Elliot, J. L., Kern, S. D., Clancy, K. B., et al. 2005, *AJ*, 129, 1117
- Emel'yanenko, V. V., Asher, D. J., & Bailey, M. E. 2004, *MNRAS*, 350, 161
- . 2005, *MNRAS*, 361, 1345
- Farinella, P., Paolicchi, P., & Zappala, V. 1982, *Icarus*, 52, 409
- Fedele, D., Tazzari, M., Booth, R., et al. 2018, *A&A*, 610, A24
- Fraser, W. C. 2009, *ApJ*, 706, 119
- Fraser, W. C., Brown, M. E., Morbidelli, A. r., Parker, A., & Batygin, K. 2014, *ApJ*, 782, 100
- Fraser, W. C., & Kavelaars, J. J. 2009, *AJ*, 137, 72
- Fraser, W. C., Kavelaars, J. J., Holman, M. J., et al. 2008, *Icarus*, 195, 827
- Fuentes, C. I., George, M. R., & Holman, M. J. 2009, *ApJ*, 696, 91
- Fuentes, C. I., & Holman, M. J. 2008, *AJ*, 136, 83
- Gil-Hutton, R., Licandro, J., Pinilla-Alonso, N., & Brunetto, R. 2009, *A&A*, 500, 909
- Gladman, B., Holman, M., Grav, T., et al. 2002, *Icarus*, 157, 269
- Gladman, B., Kavelaars, J. J., Petit, J.-M., et al. 2001, *AJ*, 122, 1051
- Gladman, B., Marsden, B. G., & Vanlaerhoven, C. 2008, in *The Solar System Beyond Neptune*, ed. Barucci, M. A., Boehnhardt, H., Cruikshank, D. P., & Morbidelli, A. (University of Arizona Press, Tucson, AZ), 43–57
- Gladman, B., Lawler, S. M., Petit, J. M., et al. 2012, *AJ*, 144, 23

- Goldreich, P., Lithwick, Y., & Sari, R. 2004, *ARA&A*, 42, 549
- Greenberg, R., Hartmann, W. K., Chapman, C. R., & Wacker, J. F. 1978, *Icarus*, 35, 1
- Greenberg, R., Weidenschilling, S. J., Chapman, C. R., & Davis, D. R. 1984, *Icarus*, 59, 87
- Greenstreet, S., Gladman, B., & McKinnon, W. B. 2015, *Icarus*, 258, 267
- Greenstreet, S., Gladman, B., McKinnon, W. B., Kavelaars, J. J., & Singer, K. N. 2019, *ApJ*, 872, L5
- Harris, A. W., & Harris, A. W. 1997, *Icarus*, 126, 450
- Holman, M. J., Payne, M. J., Fraser, W., et al. 2018, *ApJ*, 855, L6
- Holsapple, K. A. 1993, *Annual Review of Earth and Planetary Sciences*, 21, 333
- . 1994, *Planet. Space Sci.*, 42, 1067
- Housen, K. R., & Holsapple, K. A. 1990, *Icarus*, 84, 226
- . 1999, *Icarus*, 142, 21
- . 2011, *Icarus*, 211, 856
- Huang, J., Andrews, S. M., Dullemond, C. P., et al. 2018, *ApJ*, 869, L42
- Irwin, M., Tremaine, S., & Zytkov, A. N. 1995, *AJ*, 110, 3082
- Jewitt, D., & Luu, J. 1993, *Nature*, 362, 730
- Jewitt, D., Luu, J., & Chen, J. 1996, *AJ*, 112, 1225
- Jewitt, D., Luu, J., & Trujillo, C. 1998, *AJ*, 115, 2125
- Jewitt, D. C., & Luu, J. X. 1995, *AJ*, 109, 1867
- Johansen, A., & Lambrechts, M. 2017, *Annual Review of Earth and Planetary Sciences*, 45, 359
- Kennedy, G. M., & Wyatt, M. C. 2011, *MNRAS*, 412, 2137
- Kenyon, S. J. 2002, *PASP*, 114, 265
- Kenyon, S. J., & Bromley, B. C. 2002, *ApJ*, 577, L35
- . 2004a, *AJ*, 127, 513
- . 2004b, *AJ*, 128, 1916
- . 2008, *ApJS*, 179, 451
- . 2010, *ApJS*, 188, 242
- . 2012, *AJ*, 143, 63
- . 2014, *AJ*, 147, 8
- . 2015, *ApJ*, 806, 42

- . 2016, *ApJ*, 817, 51
- . 2017, *ApJ*, 839, 38
- . 2019, *AJ*, 158, 142
- Kenyon, S. J., Bromley, B. C., O’Brien, D. P., & Davis, D. R. 2008, in *The Solar System Beyond Neptune*, ed. Barucci, M. A., Boehnhardt, H., Cruikshank, D. P., & Morbidelli, A. (University of Arizona Press, Tucson, AZ), 293–313
- Kenyon, S. J., & Luu, J. X. 1998, *AJ*, 115, 2136
- . 1999a, *AJ*, 118, 1101
- . 1999b, *ApJ*, 526, 465
- Kenyon, S. J., Najita, J. R., & Bromley, B. C. 2016, *ApJ*, 831, 8
- Khain, T., Becker, J. C., Lin, H. W., et al. 2020, *AJ*, 159, 133
- Kobayashi, H., & Tanaka, H. 2010, *Icarus*, 206, 735
- Kovalenko, I. D., Doressoundiram, A., Lellouch, E., et al. 2017, *A&A*, 608, A19
- Krivov, A. V., Sremcević, M., & Spahn, F. 2005, *Icarus*, 174, 105
- Lawler, S. M., Shankman, C., Kavelaars, J. J., et al. 2018, *AJ*, 155, 197
- Leinhardt, Z. M., & Stewart, S. T. 2012, *ApJ*, 745, 79
- Levison, H. F. 1996, in *Astronomical Society of the Pacific Conference Series*, Vol. 107, *Completing the Inventory of the Solar System*, ed. T. Rettig & J. M. Hahn, 173–191
- Levison, H. F., & Duncan, M. J. 1997, *Icarus*, 127, 13
- Levison, H. F., & Morbidelli, A. 2003, *Nature*, 426, 419
- Levison, H. F., Morbidelli, A., Vanlaerhoven, C., Gomes, R., & Tsiganis, K. 2008, *Icarus*, 196, 258
- Li, J., Lawler, S. M., Zhou, L.-Y., & Sun, Y.-S. 2020, *MNRAS*, 492, 3566
- Li, J., Zhou, L.-Y., & Sun, Y.-S. 2014a, *MNRAS*, 437, 215
- . 2014b, *MNRAS*, 443, 1346
- Lissauer, J. J. 1987, *Icarus*, 69, 249
- Liu, C.-Y., Doressoundiram, A., Roques, F., et al. 2015, *MNRAS*, 446, 932
- Löhne, T., Krivov, A. V., & Rodmann, J. 2008, *ApJ*, 673, 1123
- Long, D. E., Zhang, K., Teague, R., & Bergin, E. A. 2020, *ApJ*, 895, L46
- Long, F., Pinilla, P., Herczeg, G. J., et al. 2018, *ApJ*, 869, 17
- Love, S. G., & Ahrens, T. J. 1996, *Icarus*, 124, 141

- Luu, J., Marsden, B. G., Jewitt, D., et al. 1997, *Nature*, 387, 573
- Luu, J. X., & Jewitt, D. 1988, *AJ*, 95, 1256
- Luu, J. X., & Jewitt, D. C. 1998, *ApJ*, 502, L91
- . 2002, *ARA&A*, 40, 63
- Malhotra, R. 1993, *Nature*, 365, 819
- . 1995, *AJ*, 110, 420
- Malhotra, R., Lan, L., Volk, K., & Wang, X. 2018, *AJ*, 156, 55
- Morbidelli, A., & Levison, H. F. 2004, *AJ*, 128, 2564
- Mordasini, C., Mollière, P., Dittkrist, K.-M., Jin, S., & Alibert, Y. 2015, *International Journal of Astrobiology*, 14, 201
- Nesvorný, D. 2015, *AJ*, 150, 73
- Nesvorný, D., & Vokrouhlický, D. 2016, *ApJ*, 825, 94
- Nimmo, F., Umurhan, O., Lisse, C. M., et al. 2017, *Icarus*, 287, 12
- O’Brien, D. P., & Greenberg, R. 2003, *Icarus*, 164, 334
- Ohtsuki, K. 1992, *Icarus*, 98, 20
- Ohtsuki, K., Stewart, G. R., & Ida, S. 2002, *Icarus*, 155, 436
- Pan, M., & Sari, R. 2005, *Icarus*, 173, 342
- Pan, M., & Schlichting, H. E. 2012, *ApJ*, 747, 113
- Petit, J.-M., Holman, M. J., Gladman, B. J., et al. 2006, *MNRAS*, 365, 429
- Petit, J.-M., Kavelaars, J. J., Gladman, B. J., et al. 2011, *ArXiv e-prints*, arXiv:1108.4836
- Petit, J. M., Kavelaars, J. J., Gladman, B. J., et al. 2017, *AJ*, 153, 236
- Pitjeva, E. V., & Pitjev, N. P. 2018, *Celestial Mechanics and Dynamical Astronomy*, 130, 57
- Schlichting, H. E., Fuentes, C. I., & Trilling, D. E. 2013, *AJ*, 146, 36
- Schlichting, H. E., Ofek, E. O., Wenz, M., et al. 2009, *Nature*, 462, 895
- Schlichting, H. E., & Sari, R. 2011, *ApJ*, 728, 68
- Schlichting, H. E., Ofek, E. O., Sari, R., et al. 2012, *ApJ*, 761, 150
- Schwamb, M. E., Brown, M. E., & Fraser, W. C. 2014, *AJ*, 147, 2
- Shankman, C., Gladman, B. J., Kaib, N., Kavelaars, J. J., & Petit, J. M. 2013, *ApJ*, 764, L2
- Shankman, C., Kavelaars, J., Gladman, B. J., et al. 2016, *AJ*, 151, 31

- Sheppard, S. S., Jewitt, D. C., Trujillo, C. A., Brown, M. J. I., & Ashley, M. C. B. 2000, *AJ*, 120, 2687
- Sicardy, B., Ortiz, J. L., Assafin, M., et al. 2011, *Nature*, 478, 493
- Singer, K. N., McKinnon, W. B., & Nowicki, L. T. 2013, *Icarus*, 226, 865
- Singer, K. N., & Stern, S. A. 2015, *ApJ*, 808, L50
- Singer, K. N., McKinnon, W. B., Gladman, B., et al. 2019, *Science*, 363, 955
- Spencer, J. R., Stern, S. A., Moore, J. M., et al. 2020, *Science*, 367, aay3999
- Stern, S. A. 1995, *AJ*, 110, 856
- . 1996, *AJ*, 112, 1203
- Stern, S. A., & Colwell, J. E. 1997a, *AJ*, 114, 841
- . 1997b, *ApJ*, 490, 879
- Stern, S. A., Grundy, W. M., McKinnon, W. B., Weaver, H. A., & Young, L. A. 2018, *ARA&A*, 56, 357
- Stern, S. A., Bagenal, F., Ennico, K., et al. 2015, *Science*, 350, aad1815
- Trujillo, C. A., Jewitt, D. C., & Luu, J. X. 2000, *ApJ*, 529, L103
- . 2001a, *AJ*, 122, 457
- . 2001b, *AJ*, 122, 457
- Vilenius, E., Kiss, C., Mommert, M., et al. 2012, *A&A*, 541, A94
- Vilenius, E., Kiss, C., Müller, T., et al. 2014, *A&A*, 564, A35
- Vilenius, E., Stansberry, J., Müller, T., et al. 2018, *A&A*, 618, A136
- Volk, K., & Malhotra, R. 2008, *ApJ*, 687, 714
- Volk, K., Murray-Clay, R., Gladman, B., et al. 2016, *AJ*, 152, 23
- Volk, K., Murray-Clay, R. A., Gladman, B. J., et al. 2018, *AJ*, 155, 260
- Walsh, K. J., & Levison, H. F. 2015, *AJ*, 150, 11
- Weidenschilling, S. J. 1974, *Icarus*, 22, 426
- . 1989, *Icarus*, 80, 179
- . 1997, *Icarus*, 127, 290
- . 2010a, *ApJ*, 722, 1716
- . 2010b, *ApJ*, 722, 1716
- Wetherill, G. W. 1980, *ARA&A*, 18, 77
- Wetherill, G. W., & Stewart, G. R. 1989, *Icarus*, 77, 330

- . 1993, *Icarus*, 106, 190
- Williams, D. R., & Wetherill, G. W. 1994, *Icarus*, 107, 117
- Williams, I. P., O’Ceallaigh, D. P., Fitzsimmons, A., & Marsden, B. G. 1995, *Icarus*, 116, 180
- Wyatt, M. C. 2008, *ARA&A*, 46, 339
- Wyatt, M. C., Clarke, C. J., & Booth, M. 2011, *Celestial Mechanics and Dynamical Astronomy*, 111, 1
- Wyatt, M. C., & Dent, W. R. F. 2002, *MNRAS*, 334, 589
- Wyatt, M. C., Smith, R., Greaves, J. S., et al. 2007a, *ApJ*, 658, 569
- Wyatt, M. C., Smith, R., Su, K. Y. L., et al. 2007b, *ApJ*, 663, 365
- Yoshida, F., & Nakamura, T. 2005, *AJ*, 130, 2900
- . 2008, *PASJ*, 60, 297
- Yoshida, F., & Terai, T. 2017, *AJ*, 154, 71
- Yoshida, F., Terai, T., Ito, T., et al. 2019, *Planet. Space Sci.*, 169, 78
- Youdin, A. N., & Kenyon, S. J. 2013, *From Disks to Planets*, ed. T. D. Oswalt, L. M. French, & P. Kalas (Dordrecht: Springer Science & Business Media), 1
- Yu, T. Y. M., Murray-Clay, R., & Volk, K. 2018, *AJ*, 156, 33
- Zhang, K., Bergin, E. A., Blake, G. A., et al. 2016, *ApJ*, 818, L16
- Zhang, Z.-W., Lehner, M. J., Wang, J.-H., et al. 2013, *AJ*, 146, 14